

RADIOSENSITIZATION EFFECTS OF GOLD  
NANOPARTICLES IN PROTON THERAPY

BY

CHARNAY CUNNINGHAM

2017



UNIVERSITY *of the*  
WESTERN CAPE

# RADIOSENSITIZATION EFFECTS OF GOLD NANOPARTICLES IN PROTON THERAPY

by

**CHARNAY CUNNINGHAM**

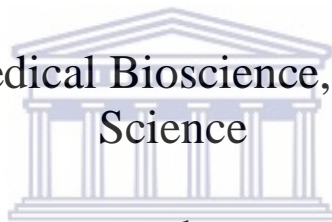
Submitted in partial fulfilment for the degree

*Magister Scientiae*

(Nanoscience)

in the

Department of Medical Bioscience, Faculty of Natural  
Science



at the

UNIVERSITY of the  
WESTERN CAPE

University of the Western Cape  
Bellville  
South Africa

**Supervisor:** Prof. M. de Kock

**Co-supervisor:** Dr. C. Vandevoorde

**Co-supervisor:** Prof. S. Slabbert

**Submitted:** November 2017

---

## DECLARATION

---

I, the undersigned, hereby declare that the work contained in this thesis titled **Radiosensitization effects of gold nanoparticles in proton therapy** is my own work and has not previously been submitted for any degree or assessment at any university. All the sources that I have used or quoted have been indicated and acknowledged by means of complete references.

---

C. Cunningham

---

Date



---

## DEDICATION

---

*For my grandparents; Margaret and Victor Cunningham, and Elinorah and Fredrich van Reenen who would be so proud.*



---

## ACKNOWLEDGEMENTS

---

Daarom vertrou almal wat u naam bely, op U, want U, Here, laat dié wat vra na u wil, nie in die steek nie. Psalm 9:11

I would firstly like to acknowledge God. I may not be able to describe my gratefulness to you as poetically as I wish, but I can give a huge thank you. I have been highly favoured and blessed. I know that I am always protected and strengthened by you. It is your will that has allowed for the completion of this thesis. More importantly, it is your will that has caused all the contributors to this project and my life, to guide me, strengthen me and enrich my life in ways I could never have imagined. Thank you, Lord. For thy Kingdom come, thy will be done.

To my parents David and Colleen Cunningham and my brother André Cunningham, I may not show it often, but I appreciate your presence in my life so much. Thank you for all the motivation, empathy, patience and love. You have supported me in more ways than I can mention in this small section, I am so deeply grateful.

My promoter, Professor Maryna De Kock. Being your student has been a true honour and privilege. Your huge depth of knowledge and humanity astounds me daily. What I did to deserve a supervisor as thoughtful, hard as nails and brilliant as you, I will never know. What I do know however, is that learning from you will always be one of the greatest accomplishments of my life. Thank you for truly going above and beyond the call of duty for me. I could not have asked for better. I have enjoyed every minute of science and life with you!

To my co-supervisor Dr. Charlot Vandevoorde. You epitomize everything a young woman and scientist ought to be. If I am but half as excellent as you are a few years from now, I'll consider myself successful. Thank you for the guidance, support, and utter dedication you have shown towards me and this project. I would have been lost without you.

Ms. Xanthene Miles, you are truly a special person. I would never have guessed that I would gain the presence of a human being whose silent strength would support me so much. Thank you for all the lessons, tips and advice. For a wonderful friendship filled with laughter. Your future shines as bright as that personality of yours.

Ms. Monique Engelbrecht, my drill sergeant, motivator, fellow mischievous spirit and friend. Thank you for the “extra set of hands” and extra brain at times. For putting up with my venting sessions and moments of euphoria at the smallest almost insignificant accomplishments. Your guidance and support do not go unnoticed. You will reach great heights.

A huge thank you to Mr. Phillip Beukes my sample “runner”. Thank you for keeping me calm when we were in the thick of it. I know you covered great distances for me (literally) with those samples. Thank you so much!!!

Prof Jacobus Slabbert, I truly believe that learning from you makes us all better. Thank you for all the invaluable lessons, your patience with my adjustment to the pace of radiobiology, the extent to which you threw yourself into this research and valuable input throughout this project. Your brilliance and dedication have been a constant source of amazement and inspiration for me and I consider your presence throughout this year a blessing.

Prof Martin Kidd for all your help with the statistical analysis of the micronucleus assay data that gave me splitting headaches. Thank you!

Ms. Tahira Boltman. For your aid with the stability testing and insights into nanotechnology, nanoparticles and research. You are awesome!

To all my nano-buddies with whom I spent the course of this masters, getting to know all of you has been an amazing experience. To Monushia Zimri and Nancy Sarpong in particular, thank you for providing me with a wonderful friendship and support system. I will cherish you always!

My besties, Shannen Keyser and Sandrine Mwisserwa, having each of you in my life adds a tremendous amount of value to it. Thank you for surpassing the point of friends and simply becoming family. I could not be more grateful for the huge supportive role you have in my life of science and play!

To my UWC peers and friends, I wish to express my gratitude to all of you for all the input, laughs, critique and support. I have been able to tap into a wealth of knowledge and wisdom these last few years that has always left me richer with each meeting.

The staff at iThemba LABS, I know that I cannot begin to fathom the huge amounts of manpower that was required for those “proton weekends”. Thank you for toughing out long nights, presentations, informative albeit entertaining lunches and everything in between.

To all aunts, uncles and cuzzies (you know who you are), thank you for the constant check-ups, chats, support and love. You would all make amazing cheerleaders.

Finally, to Mrs. Valencia Jamali and Mrs. Chyril Abrahams, thank you for always availing yourselves to me for inquiries, coordinating travels, fighting with suppliers and sometimes just allowing a small chat. Love, your nano-annoying child.



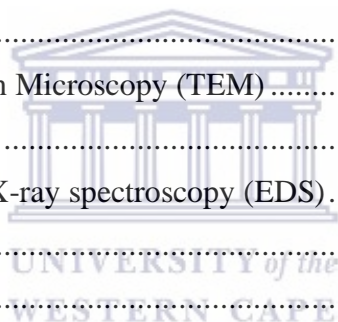
---

## TABLE OF CONTENTS

---

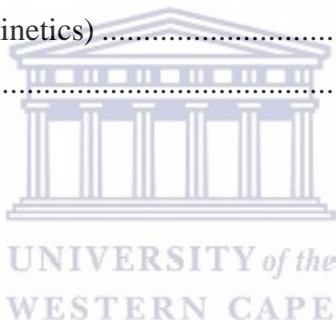
DECLARATION .....	iii
DEDICATION.....	iv
ACKNOWLEDGEMENTS.....	v
TABLE OF CONTENTS .....	viii
ABBREVIATIONS .....	xii
LIST OF FIGURES .....	xviii
LIST OF TABLES .....	xxi
ABSTRACT .....	xxii
PREFACE.....	1
CHAPTER 1: INTRODUCTION.....	2
1. Literature Review.....	2
1.1 Nanotechnology .....	2
1.1.2 The need for novel therapies in cancer treatment .....	3
1.2 Gold Nanoparticles (AuNPs) development .....	4
1.2.1 AuNPs and their application in medicine.....	5
1.3 AuNP synthesis .....	6
1.3.1 Green Chemistry and AuNPs.....	7
1.3.2 Cardamom.....	8
1.4 Radiation Therapy .....	10
1.4.1 Proton Therapy (PT).....	12
1.4.2 Relative Biological Effectiveness (RBE) and Proton Therapy .....	13
1.5 The use of gold nanoparticles as agents for radiosensitization .....	14
1.5.1 The underlying mechanism of radiosensitization.....	15
1.5.2 Proton radiation and gold nanoparticles .....	16
1.6 Overview of the Cell cycle and damage repair processes .....	18
1.6.1 Gap phase 1 .....	19
1.6.2 The S-phase.....	19
1.6.3 The G <sub>2</sub> M phase.....	20
1.6.4. Restriction Points.....	20
1.6.4.1. The G <sub>1</sub> /S checkpoint.....	20
1.6.4.2. G <sub>2</sub> M checkpoint.....	21
1.6.4.3. The Mitotic Spindle Checkpoint .....	22

1.7	The Cell cycle and radiation .....	22
1.8.	The cell cycle and gold nanoparticles.....	24
	EXPERIMENTAL AIMS .....	25
	CHAPTER 2: MATERIALS AND METHODS .....	26
2.1	AuNPs.....	26
2.1.1	AuNP synthesis (Green Chemistry).....	26
2.1.2	Spice preparation and processing.....	26
2.1.3	Temperature dependent synthesis .....	26
2.1.3.1	Temperatures between 55-85 ° C .....	26
2.1.3.2	Synthesis at room temperature (RT).....	27
2.1.4	Commercial gold nanoparticles (AuNPS). .....	27
2.1.5	AuNP treatment .....	27
2.2	AuNP Characterisation.....	28
2.2.1	UV-visible (vis) spectroscopy.....	29
2.2.2	Zeta Potential and Dynamic Light Scattering (DLS) determination.....	29
2.2.3	Stability Testing .....	29
2.2.4	Transmission Electron Microscopy (TEM) .....	30
2.2.4.1	Sample Preparation.....	30
2.2.4.2	Energy dispersive X-ray spectroscopy (EDS).....	31
2.3	AuNP uptake.....	31
2.4	Proton Radiation.....	31
2.5.	Cell line.....	33
2.5.1	Cell Culture Conditions .....	33
2.5.2	Cell Proliferation .....	33
2.5.3	MTT Assay .....	34
2.5.4	Mitotic Index.....	35
2.5.5	Clonogenic cell survival assay .....	36
2.5.6	Chromosomal damage .....	38
2.5.7	Interaction Indices .....	40
2.5.8	Cell Cycle Kinetics.....	41
2.6	Statistical Analysis .....	43
2.6.1	Cell Proliferation, MTT assay and Clonogenic cell survival assay .....	43
2.6.2	Mitotic Index.....	43
2.6.3	Radiation Damage.....	43
	CHAPTER 3: RESULTS .....	45



3.1	Gold Nanoparticle Characterisation .....	45
3.1.1	Ultraviolet Spectrophotometry.....	46
3.1.2.	Dynamic Light Scattering.....	48
3.1.3.	Zeta Potential .....	50
3.1.4.	Transmission Electron Microscopy.....	52
3.1.5.	Energy dispersive X-ray spectroscopy (EDS) .....	54
3.1.6.	Selected area diffraction (SAED).....	55
3.1.7.	Stability testing.....	56
3.1.8.	Gold Nanoparticle uptake (ICP-MS).....	60
3.2	<i>In vitro</i> analysis .....	61
3.2.1	Cell Proliferation .....	61
3.2.2	Cell Viability.....	64
3.2.3	Mitotic Index.....	65
3.3.	Proton experiments.....	65
3.3.1	Cell Survival.....	67
3.3.2	Chromosomal Damage .....	68
3.3.3.	Cell cycle kinetics .....	73
CHAPTER 4: DISCUSSION .....		77
4.1	Introduction.....	77
4.2	AuNP characterization.....	78
4.2.1	UV-vis Spectroscopy .....	78
4.2.1.1	Car-AuNPs .....	78
4.2.1.2	Citrate stabilized AuNPs .....	79
4.3	Dynamic Light Scattering (DLS) and Zeta Potential .....	80
4.3.1.	Car-AuNPs.....	80
4.3.2	Commercial (Citrate Stabilized) AuNPs .....	80
4.4	TEM, EDS and SAED.....	82
4.5	Stability testing.....	83
4.6	AuNP uptake .....	84
4.7	<i>In vitro</i> assessments .....	85
4.8	Radiation Damage.....	87
4.8.1	The Clonogenic cell survival assay .....	87
4.8.2	Chromosomal Damage .....	89
4.8.3	Cell cycle kinetics .....	94
4.8.3.1	Car-AuNPs .....	94

4.8.3.2	5 nm AuNPs .....	95
4.8.3.3	10 nm AuNPs.....	95
4.8.3.4	50 nm AuNPs .....	96
SUMMARY .....		98
CONCLUSION.....		100
REFERENCES .....		101
CHAPTER 5: ADDENDUM.....		118
5.1	AuNP images .....	118
5.2	UV-spectral curves .....	118
5.3	DLS and Zeta Potential.....	120
5.4	AuNP uptake .....	121
5.5	Statistical analysis of Mitotic index .....	122
5.6	Reference data of CSA .....	123
5.7	Data distribution curves for chromosomal damage analysis .....	124
5.8	Dose enhancement values (MNi) .....	125
5.9	RCGG values (cell cycle kinetics) .....	127
5.10	Cell cycle kinetics .....	129



---

## ABBREVIATIONS

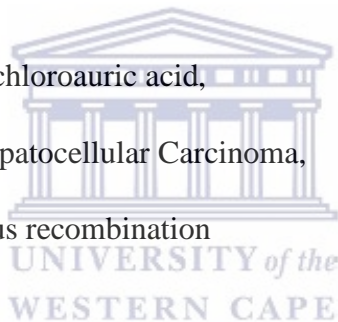
---

$\alpha$	alpha
$\beta$	beta
$\gamma$	gamma
$\lambda$	max maximum wavelength
%	percentage
°C	degree Celsius
>	greater than
<	smaller than
<b>A</b>	
AgNP	silver nanoparticle
ANOVA	Analysis of Variance
AO	Acridine Orange
APC	anaphase promoting complex or cyclosome
ATM	ataxia-telangiectasia mutated
ATR	ataxia-telangiectasia rad3-related
AuNP	gold nanoparticle
<b>B</b>	
BN	Binucleated cells
BRCA	Breast cancer 1/2
BSA	Bovine Serum Albumin
Bub	Budding uninhibited by benzimidazole
<b>C</b>	
C	Carbon

CAK	cyclin activating kinase
Car-AuNP	cardamom synthesized gold nanoparticle
CBMN	cytokinesis block micronucleus assay
Cdc	cell cycle division protein
CDK	cyclin dependent kinase
Chk	checkpoint kinases
CHO-AA8	Native Chinese Hamster Ovary
CHO-K1	Chinese Hamster Ovary
COX-2	cyclooxygenase-2
CSB	clustered strand breaks
CT	computed tomography,
Cu	Copper
<b>D</b>	
DEF	Dose enhancement factor
DLS	Dynamic light scattering
DMBA	7,12-Dimethylbenz[a]anthracene
DNA	Deoxyribonucleic acid
DSB	double-strand break
<b>E</b>	
E. coli	Escherichia coli
EDS	Energy dispersive x-ray spectroscopy
EPR	enhanced retention and permeability effect,
ETOH	ethanol
<b>F</b>	



FBS	Fetal Bovine Serum
FEG	Field Emmision Gun
<b>G</b>	
G1	Gap phase 1
G2	Gap phase 2
Glu-AuNPs	Glucose capped AuNP
GNP	Gold nanosphere
GNR	Goldnanorod
GNS	Gold nanospike
Gy	Gray
<b>H</b>	
HAuCL <sub>4</sub>	tetrahydrochlorauric acid,
Hep G2	Human Hepatocellular Carcinoma,
HR	homologous recombination
<b>I</b>	
FeNPs	Iron NPs
ICP-MS	inductively coupled mass spectrometry
IL-6	Interleukin-6
iNOS	inducible nitric oxide synthase
<b>K</b>	
KCL	potassium chloride
keV	kiloelectronvolts
kV	kilovolts
<b>L</b>	



L@AuNPs	ligand coated AuNPs
LET	linear energy transfer
<b>M</b>	
M	mass
Mad	mitotic arrest deficient protein
Mcm	minichromosome maintenance
MeV	Megaelectronvolts
MI	Mitotic Index
Mm	millimetre
MNi	micronuclei
MNP	Metallic Nanoparticles
M-phase	mitosis phase
Mps	Monopolar spindle
MRSA	Methicillin Resistant Staphylococcus Aureus
MTT	3- [4,5 – dimethylthiazol-2-yl] A 2,5 diphenyltetrazoliumbromide
mV	millivolts
<b>N</b>	
NB	nucleoplasmic bridge
NFK-B	Nuclear Factor Kappa Beta
NHEJ	Non-homologous end joining
nm	nanometer
NO	Nitric Oxide,
NP	Nanoparticle
NRF	National research foundation



## O

ORC                      origin recognition complex

## P

p53                      tumour suppressor protein 53

PBS                      Phosphate buffered saline

PDI                      Polydispersity index

PE                      Plating Efficiency

PI                      Propidium Iodide

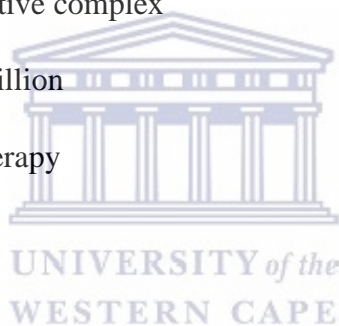
PIGE                    particle-induced gamma ray emission

PIXE                    particle-induced X-ray emission

pre-RC                pre-replicative complex

ppb                    parts per billion

PT                      Proton Therapy



## R

R                      Radius

RBE                    Relative Biological Effectiveness

ROS                    Reactive oxygen species

RT                      Radiation Therapy

## S

S. aureus              Staphylococcus aureus

SAED                   Selected area diffraction

SER                    Surface enhancement ratio

SOBP                   Spread Out Bragg Peak

S-phase	synthesis phases
SPR	Surface plasmon resonance
SSB	Single strand breaks
<b>T</b>	
TEM	Transmission electron microscopy
<b>U</b>	
UV	Ultraviolet
<b>V</b>	
V	Volume
Vis	visible
<b>Z</b>	
Z	Atomic number
ZP	Zeta Potential



---

## LIST OF FIGURES

---

<b>CHAPTER 1</b> .....	<b>2</b>
Figure 1.1: Example of the host of biomedical applications offered by NPs.....	2
Figure 1.2: Photographic evidence of the presence of AuNPs in human products for centuries.....	4
Figure 1.3: AuNPs are versatile and tuneable to various shapes and sizes.....	5
Figure 1.4: Schematic of therapeutic applications of AuNP.....	6
Figure 1.5: reactions involved in the green synthesis of gold nanoparticles and their applications.....	7
Figure 1.6: Elattaria cardamomum commonly known as “Green or true cardamom” represented photographically .....	9
Figure 1.7: Illustration of mechanisms of radiation damage.....	10
Figure 1.8: Schematic representation of the difference in radiation tracks.....	11
Figure 1.9: Energy deposition vs depth.....	13
Figure 1.10: Schematic depicting electron ejections upon X-ray interaction with high-Z materials.....	16
Figure 1.11: Diagram depicting the phases of the cell cycle.....	18
Figure 1.12: Interactions between the DNA damage response pathways and DNA repair networks.....	24
<b>CHAPTER 2</b> .....	<b>26</b>
Figure 2.1: Example of the colour change in the biological media seen after a 24 hour incubation period with AuNPs.....	30
Figure 2.2: Schematic depiction of irradiation conditions for proton experiments.....	32
Figure 2.3: Images of experimental setups for proton experiments.....	32
Figure 2.4: Image of the solubilized crystal violet dye upon addition of the detergent reagent (Triton-X).....	34
Figure 2.5: Graphic depiction of the steps involved in the clonogenic cell survival assay.....	36
Figure 2.6: Image depicting an example of the colonies upon completion of the CSA assay.....	37

Figure 2.7: MNi and nucleoplasmic bridge formation in cells undergoing nuclear division.....	40
Figure 2.8 Graphic depiction of forward and side scatter used to measure cell size and inner complexity within a flow cytometer.....	41
<b>CHAPTER 3.....</b>	<b>45</b>
Figure 3.1: Images depicting various AuNP colloidal solutions used for treatment.....	45
Figure 3.2: The effect of temperature of the synthesis reaction on AuNP product.....	46
Figure 3.3: UV absorption spectra of Car-AuNPs.....	47
Figure 3.4: UV absorption spectra of 5, 10 and 50 nm AuNPs.....	47
Figure 3.5: The hydrodynamic sizes of AuNPs. ....	49
Figure 3.6: Zeta Potential analysis of AuNPs. Barring the 5 nm AuNPs, all AuNPs were relatively stable and anionic.....	51
Figure 3.7: TEM images of Car-AuNPs.....	52
Figure 3.8: Elemental analysis results of AuNPs synthesized.....	54
Figure 3.9: Images depicting SAED results of Car-AuNPs synthesized at 85 °C.....	55
Figure 3.10: The Absorption spectra of each AuNP solution incubated for 0 hour (A-D).....	57
Figure 3.11: The Absorption spectra of AuNP solutions after a 24 hour incubation period with biological media.....	59
Figure 3.12: Quantities of AuNPs taken up by CHO cells after a 24 hour incubation with 10 nm and 50 nm AuNPs.....	60
Figure 3.13: Effect of AuNPs on cell proliferation after 4 h incubation period.....	61
Figure 3.14: Effect of 50 nm AuNPs on cell proliferation after 4 hour incubation period.....	62
Figure 3.15: Effect of larger AuNPs at low concentrations on cell proliferation after a 24-hour incubation period.....	62
Figure 3.16: The effect of 1.8 cineole on cell viability.....	64
Figure 3.17: The effect of 1.8 cineole and AuNPs on mitotic index.....	65
Figure 3.18: Surviving fractions of cells after the concurrent treatment of with 50 nm AuNPs (37 µM) and 6Gy dose of protons.....	67
Figure 3.19: Images of BN cells containing A) no MNi B) two MNi C) one MNi and D) BN	

containing no nuclei with a mononucleated cell in prometaphase of mitosis.....	68
Figure 3.20: MNi frequencies measured for protons with 5 and 10 nm AuNPs after a 4 hour incubation period.....	69
Figure 3.21: Frequency of MNi measured after exposure with protons and 37 $\mu$ M of 50 nm AuNPs.....	70
Figure 3.22: MNi frequency after exposure with 50 nm AuNPs at a concentration of 37 $\mu$ M for 24 hours and subsequent administration of protons.....	71
Figure 3.23: The effect of 10 nm (50 $\mu$ g/ml) and 50 nm (10 $\mu$ g/ml) AuNPs with a 6 Gy dose of protons on cell cycle progression.....	73
<b>CHAPTER 5: ADDENDUM.....</b>	<b>118</b>
Figure 5.1: Photographic images depicting the difference in colour of AuNPs synthesized with different temperatures.....	118
Figure 5.2: Temperature dependent synthesis of Car-AuNPs with extract prepared from whole cardamom seeds.....	118
Figure 5.3: The effect of HAuCl <sub>4</sub> quantity on AuNP quality.....	129
Figure 5.4: Size distribution curves prior to and after filtering the AuNPs.....	120
Figure 5.5: Statistical analysis of MI data.....	122
Figure 5.6: Distribution curves for MNi data of 5, 10 and Car-AuNPs. Despite a few outliers, the data was relatively normally distributed.....	124
Figure 5.7: Distribution curves for MNi data of 50 nm AuNPs.....	124
Figure 5.8: Distribution data of the MNi assay performed after a 24 hour incubation period with 50 nm AuNPs. The MNi data was normally distributed.....	125
Figure 5.9: Non-irradiated controls of CHO cells.....	129
Figure 5.10: The effect of Car-AUNPs on cell cycle kinetics.....	130
Figure 5.11: The effect of 5 nm AuNPs on cell cycle kinetics.....	131
Figure 5.12: The effect of 10 nm AuNPs on cell cycle kinetics.....	132
Figure 5.13: The effect of 50 nm AuNPs on cell cycle kinetics.....	133

---

## LIST OF TABLES

---

<b>CHAPTER 3</b> .....	<b>45</b>
Table 3.1: DLS and Zeta Potential results.....	51
Table 3.2: Estimated quantities of AuNP uptake after a 24 hour incubation period with increasing concentrations of each AuNP type.....	60
Table 3.3: The effect of Car-AuNPs and protons on cell cycle progression.....	74
Table 3.4: The effect of 5 nm AuNPs and protons on cell cycle progression.....	74
Table 3.5: The effect of 10 nm AuNPs and protons on cell cycle progression.....	75
Table 3.6: The effect of 50 nm AuNPs on cell cycle progression.....	76
<b>CHAPTER 5</b> .....	<b>118</b>
Table 5.1: The stability of Car-AuNPs over time. Car-AuNP stability in storage was measured by Zeta Potential and DLS over time.....	120
Table 5.2 AuNP uptake efficiency determined using mean side scatter obtained from flow cytometry.....	121
Table 5.3.: The cell survival clonogenic assay performed with two concentrations of 10 AuNPs after a 24 hour pre-incubation period.....	123
Table 5.4: The cell survival clonogenic assay performed with two concentrations of 10 nm AuNPs and 8 Gy of C <sup>60</sup> radiation.....	123
Table 5.5. Calculated DEFs for CHO cells treated with 5nm, 10nm and Car-AuNPs for 4 hours followed by proton radiation.....	125
Table 5.6 Dose enhancement values expressed after a 4 h incubation period of AuNPs and treatment with protons (2 Gy and 4 Gy).....	125
Table 5.7: Dose enhancement values expressed after a 24 hour incubation period of 50 nm AuNPs and treatment with protons.....	126
Table 5.8: RCGG values determined for Car-AuNP exposed cells.....	126
Table 5.9: RCGG values determined for cells exposed to 5 nm AuNPs, protons, and 5 nm AuNPs in combination with protons.....	127
Table 5.10: RCGG values determined for cells exposed to 10 nm AuNPs, protons and 10 nm AuNPs in combination with protons.....	127
Table 5.11: RCGG values calculated for cells exposed to 50 nm AuNPs, protons and 50 nm AuNPs in combination with protons.....	128

---

## ABSTRACT

---

Despite recent advances in radiotherapy, some tumours have shown to be resistant to treatment and patients still experience long term side effects. Gold nanoparticles (AuNPs) have been identified as effective radiosensitizers when employed concurrently with kilovoltage X-rays, which could selectively increase the dose delivered to a patient's tumour. The clinical application of proton radiation has gained renewed attention due to the lower integral body dose of protons compared to traditional X-ray based therapy. While extensive research has been formed on the behaviour of AuNPs in photon beams, limited information is available on the combination of AuNPs and proton radiation. Several questions remain regarding the interaction of protons with the AuNPs and possible dose enhancement effects at different depths along the Spread Out Bragg Peak (SOBP).

*In vitro* radiosensitization effects of AuNPs and protons at clinically relevant energies (200 MeV) were investigated in Chinese hamster Ovary (CHO-K1) cells by analysing its influence on cell growth, clonogenic survival, micronucleus induction and cell cycle progression. The effects of synthesis method and size of AuNPs were investigated using Car-AuNPs synthesized from *Elattaria Cardamom* (Car) extract (green synthesis) and commercial AuNPs (chemical synthesis) of different sizes in CHO cells irradiated at increasing depths along the proton beam.

Zeta Potential analysis, UV-vis spectroscopy and transmission electron microscopy was used to characterize the AuNPs. The synthesized Car-AuNPs were stable (ZP: -19.1mV) and monodispersed (PDI: 0.242). The study established that intricacies in Car-AuNP synthesis exist and can be attuned to control Car-AuNP size and product quality. Different temperatures and methods of extract preparation resulted in pronounced effects on the Car-AuNP size and dispersity level. Adjustment of these parameters yielded smaller (UV-spectral shifts from 590 nm to 525nm) uniformly shaped AuNPs (TEM: ~11 nm). Characterization of the 10 nm and 50 nm AuNPs obtained from Sigma, showed that these AuNPs were stable (-32.8 mV and -35.1 mV) and monodispersed (PDI: 0.225 and 0.102) over a 24-hour incubation period at both 25 °C and 37 °C.

Spectrophotometrical studies and haematoxylin and eosin staining indicated that the chemically synthesized AuNPs stimulated mitosis at lower concentrations (5  $\mu\text{g/ml}$ / 10  $\mu\text{g/ml}$ ) but exerted cytotoxic effects at high (50 $\mu\text{g/ml}$ ) concentrations.

Results from the clonogenic assay revealed that 50 nm AuNPs in combination with a 6 Gy dose of protons reduced surviving fractions of cells from 0.082 to 0.021 in the entrance plateau and from 0.059 to 0.013 in the middle of the SOBP. The cytokinesis block micronucleus (CBMN) assay indicated an increase in the number of micronuclei (MNI) by the 10 nm AuNPs. In contrast, the Car-AuNPs showed a decrease in the number of MNI. This decrease in radiation damage could be as a result of a radioprotective effect attributable to the phytochemical constituents within the cardamom extract.

Cell cycle progression showed a  $G_1$  peak (71 %) in the presence of the 10nm AuNPs in comparison to control  $G_1$  (33.94%) without radiation exposure. 6 Gy proton radiation caused an accumulation of cells in  $G_2M$ , possibly indicative of a  $G_2M$  block. The accumulation was incremental and increased with increasing depth along the proton beam, resulting in the largest  $G_2M$  peak observed in samples irradiated in the distal position of the SOBP.

This study verified that an interaction between AuNPs and proton radiation does exist and that the observed effects is dependent on the AuNP size and synthesis. Statistical analysis revealed that the interaction was independent of the irradiation depth along a modulated proton beam. However, the fact that chromosomal damage and changes in cell cycle kinetics were observed, warrants further investigation to clarify underlying mechanisms.

---

## PREFACE

---

Delivering a curative dose to the tumour while limiting the dose to surrounding healthy tissue is one of the biggest challenges in radiotherapy. The clinical application of proton radiation, previously maligned as a therapeutic option that is too costly, has gained renewed attention. This is due to the lower integral body dose of protons compared to traditional X-ray therapy which stems from the ability to confine the radiation dose to the malignant tissue and the lack of an exit dose. The reduced dose to surrounding normal tissue makes proton therapy particularly interesting to paediatric cancer patients, as children have a higher risk to develop secondary malignancies after radiation exposure. In addition, the incorporation of proton therapy (PT) with nanobiotechnology presents an even greater opportunity to improve the efficacy of radiotherapy.

Nanotechnology, an emerging and invasive discipline, yields particles that fall in a size range between 1-100 nm. Since its inception, the field has produced nanoparticles that can access the minutest parts of biological systems previously known to be inaccessible by other particles due to the microscopic size of these systems. Thus, nanotechnology presents a unique option to both target and treat carcinomas individually whilst preserving the integrity of the surrounding healthy tissue and potentially reducing the side effects associated with current cancer therapeutics.

Gold nanoparticles (AuNPs) have been extensively studied and like its bulk form, proven to exhibit a plethora of characteristics that can be exploited for medicinal use. AuNPs are selectively retained within malignant cells and have the potential to sensitize or improve the sensitivity of cancerous cells to radiation therapy. The combination of gold nanoparticles and proton radiation therefore presents an ideal mixture to enhance the effects of radiotherapy on radio-resistant carcinomas.

---

## CHAPTER 1: INTRODUCTION

---

### 1. Literature Review

#### 1.1 Nanotechnology

Nanotechnology is based on the manipulation of individual atoms and molecules to produce materials that fall into a scale ranging between 1-100 nm known as nanoparticles (NP) (Adams & Barbante, 2013). NPs exhibit unique physical and chemical properties that are exploited in optical, electronic, chemical and mechanical fields. Their versatility in nanobiotechnology stems from the ability to tailor their size, shape and composition (Arvizo, et al., 2010).

The small size and high surface-to-volume ratio of NPs, allow these particles easy access to biological systems and molecules (Blecher, et al., 2011) consequently gaining a foothold in the medical field (Miu & Sprando, 2010). A multitude of nanoparticles have been created with the main goal of enhancing the properties of a system previously stagnated by a lack of advancement in technology.

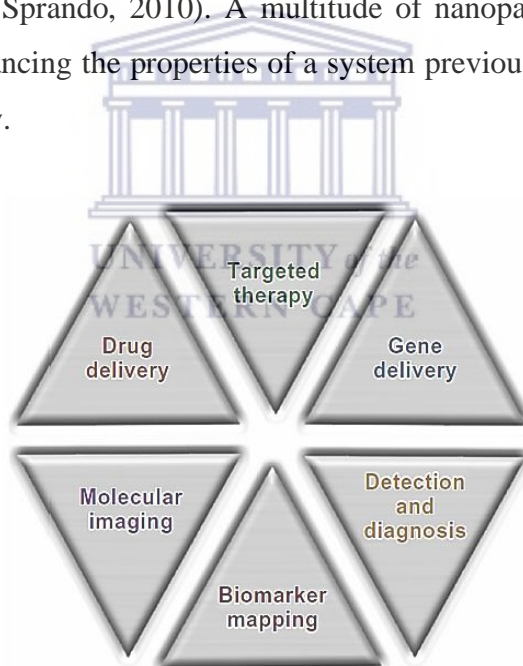


**Figure 1.1:** Example of the host of biomedical applications offered by NPs. Excerpted from Sanna et al., 2014

NPs can be deployed for the transport and delivery of a variety of biomedical entities for the treatment, prevention and diagnosis of many diseases (Figure 1.1) (Datta & Jaitawat, 2006; Sanna, et al., 2014; Pandey & Ahmad, 2011). The ability to effect diagnostic and therapeutic changes on a nanoscale could provide significant changes in medical care (Gannon, et al., 2008).

More recently, the breakthrough potential of cancer nanotechnology has been exhibited by various research papers employing NPs to improve cancer therapy (Bertrand, et al., 2014).

### **1.1.2 The need for novel therapies in cancer treatment**

Despite the development of targeted chemotherapeutic drugs over the past 20 years, cancer remains among the deadliest of human diseases (Linton, et al., 2016).

At present, intrusive processes such as chemotherapy, radiation and surgery to remove the tumour if possible, potentially followed by more chemotherapy and radiation, form the most successful cancer treatments (Yao, et al., 2016). However, anticancer agents do not differentiate between malignant and normal cells, leading to severe systemic toxicities (Sinha, et al., 2009). Therefore, the benefits of the treatments are often marred by the negative side effects and a high percentage of tumour recurrence (Foote, et al., 2012; Curren, et al., 2011).

NPs hold the potential to address and remedy some of the most significant limitations of chemotherapy, namely, its lack of specificity and narrow window of therapeutic efficacy (Steichen, et al., 2013). AuNPs are one of the most widely studied metallic NPs for their potential application in cancer diagnostics and treatment (Mirkin, et al., 2010). NPs are particularly relevant to tumours because tumours possess a leaky vasculature that is absent in normal/healthy tissue. Upon intravenous administration, NPs tend to circulate for longer times, if they are not small enough for renal excretion or large enough for rapid entrapment and recognition by the reticuloendothelial system (Yin, et al., 2014; Kobayashi, et al., 2014). AuNPs (without surface modification), will thus preferentially leak into tumour tissue via the leaky vasculature and are then retained in the tumour bed due to reduced lymphatic drainage. This process is known as the enhanced retention and permeability effect (EPR) (Kobayashi, et al., 2014). Auroshell is a gold nanoshell that uses passive targeting to reach tumour cells and is currently being applied in a clinical trial. Once inside, near- infrared laser light is applied, which heats the particles and thermally destroys the tumour and surrounding blood vessels without significant damage to healthy tissue (Grossman & Mc Neil, 2012). Thus AuNPs present the potential for a variety of applications and have been incorporated into various forms of therapy to improve its efficacy.

## 1.2 Gold Nanoparticles (AuNPs) development

Gold has been highly regarded as a medicinal compound for centuries (Jemal, et al., 2009). The first information on colloidal gold is recorded in treatises by Arabian, Chinese and Indian scientists who tried to attain colloidal gold as early as the fourth-fifth centuries (Daraee, et al., 2014). The discovery of AuNPs have been attributed to Michael Faraday's observation over 150 years ago, that colloidal gold solutions have properties that differ from its bulk counterpart (Hayat, 1989; Mirkin, et al., 2010). Years later, gold was incorporated into clinical trials initiated in 1925 to determine the efficacy of gold complexes in alleviating rheumatoid arthritis (Aaseth, et al., 1998). Recently, AuNPs have become a central component of medical discovery.

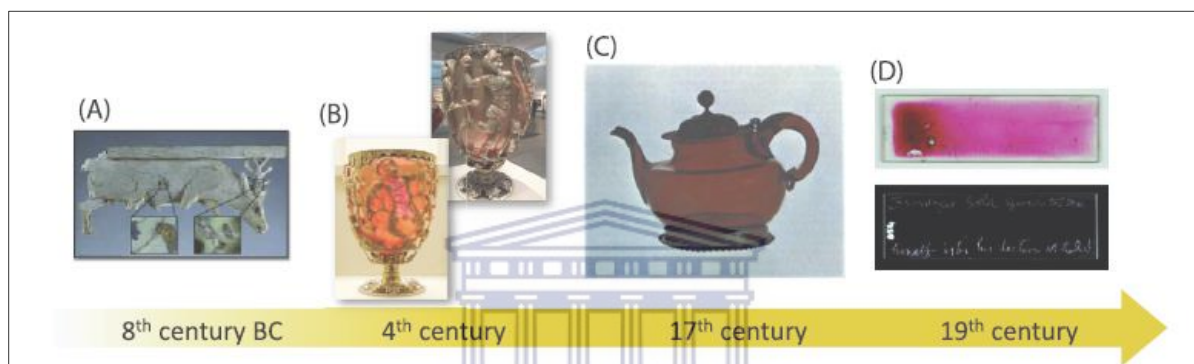


**Figure 1.2:** Photographic evidence of the presence of AuNPs in human products for centuries **A)** Egyptian gold plated archaeological ivory **B)** 4<sup>th</sup> century Roman Lycurgus cup which appears red upon illumination from the front and green upon illumination from the back **C)** Teapot (1680) obtained by Johannes Kunkel using the 'Purple Casius' technique **D)** Michael Faraday's original gold colloid samples. Image generated by and excerpted from (Vincenzo, et al., 2017).

### 1.2.1 AuNPs and their application in medicine

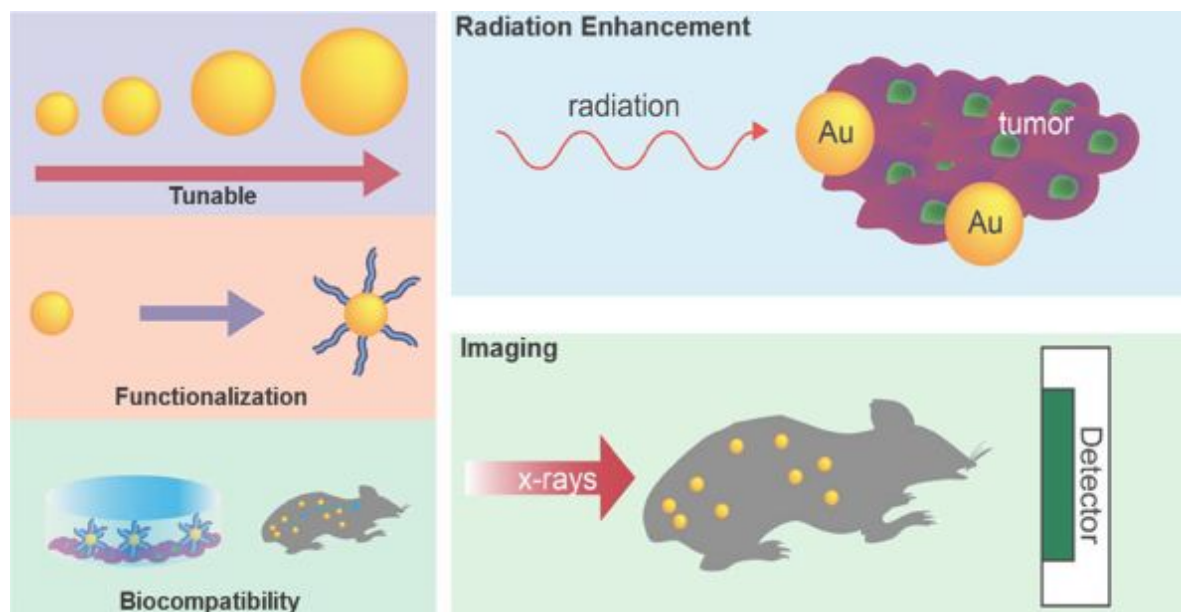


**Figure 1.3:** AuNPs are versatile and tuneable to various shapes and sizes, can be functionalized are generally safe and non-toxic and in vitro and in vivo. They have the ability to enhance radiation and serve as excellent contrast agents (Dorsey, et al., 2013).

Characteristic surface plasmon resonance (SPR) exhibited by AuNPs, results from photon confinement to a small particle size, enhancing all the radiative and non-radiative properties of the AuNPs offering multiple modalities (Huang & El-Sayed, 2010). AuNPs also have versatile surface chemistries which permits them to be coated with a wide range of molecules, allowing for diverse applications (Klebstov & Dykamn, 2010).

The unique optical properties of AuNPs, and the nearly 100 % conversion of absorbed light to heat, is sufficient to induce cellular damage such as hyperthermia, coagulation and evaporation (Svaarsand, et al., 1990; Dorsey, et al., 2013). Additionally, the high atomic number of gold allows elevated absorption and enhancement of ionizing radiation, such as superior X-ray attenuation for imaging applications (Dorsey, et al., 2013).

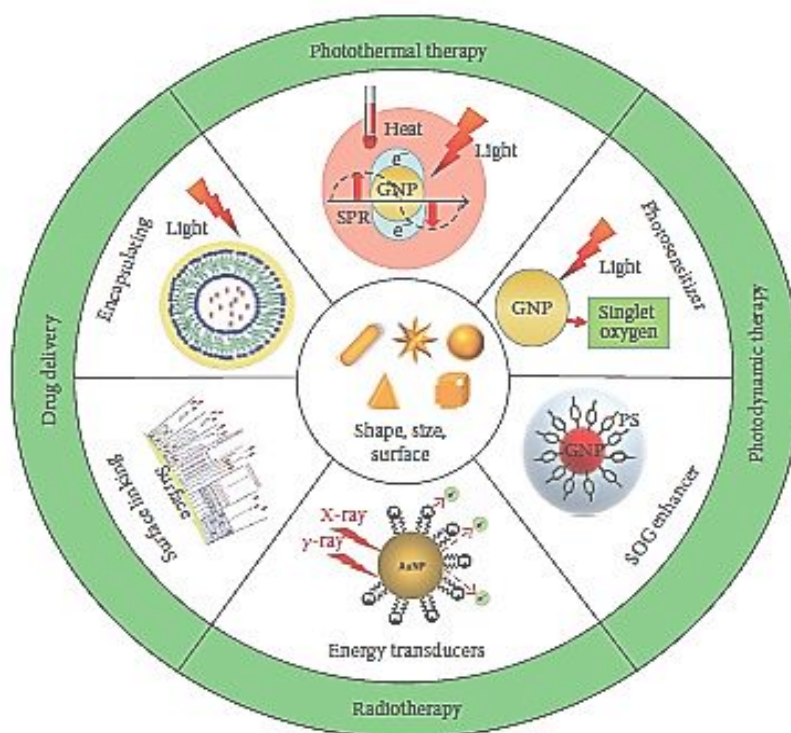


**Figure 1.4:** Schematic of therapeutic applications of AuNPs. Image excerpted from (Yao, et al., 2016)

### 1.3 AuNP synthesis

Several approaches exist for the fabrication of AuNPs; the crudest method, reduction of gold during which gold salts are reduced, was created by Turkevich in 1951 (Turkevich, et al., 1951) and modified by Frens (Frens, 1972). During this process, the nucleation of gold ions results in the formation of AuNPs (Arvizo, et al., 2010). The technique is based on the reaction that occurs for all bottom-up AuNP synthesis procedures in which an auric compound/metal salt (usually tetrahydrochloroauric acid ( $\text{HAuCl}_4 \cdot 3\text{H}_2\text{O}$ )) is reduced by a chemical (citrate) reducing agent to yield the non-oxidized state of gold (Au [I]) thus forming AuNPs. Changing various parameters within the synthesis process can yield AuNPs of different sizes, shapes and stability (Tran, et al., 2016).

AuNPs can also be produced via the Brust-Schiffrin method. Devised in 1994, the authors developed the method to create AuNPs in organic liquids that are usually immiscible in water (Brust, et al., 1994). Like the Turkevich method, the reaction involves the reduction of chloroauric acid ions to form AuNPs. In addition to the aforementioned methods, a multitude of AuNP synthesis methods exists that are exploited by privately owned scientific companies to create stable, monodisperse AuNPs available commercially for research purposes.

However, chemical methods for synthesizing metal NPs generally use expensive and toxic reagents as reducing and stabilizing agents, and it is likely that trace amounts of reagents remain unreacted in solution posing danger to the environment (Shankar, et al., 2004). To this effect, one of the most essential needs in nanotechnology is to develop environmentally friendly and ‘green’ approaches to nanoparticle synthesis and has resulted in the inception of green chemistry (Thakkar, et al., 2010).

### 1.3.1 Green Chemistry and AuNPs

Green synthesis of NPs (Green-NPs) can be realized without toxic and aggressive chemicals (Li et al., 2009) as it requires a biological compound as a reducing reagent. Green synthesis is cost effective and can be manipulated to give rise to a variety of shapes and sizes. Since biological molecules are used for the synthesis, the resulting AuNPs are capable of evading immune detection, have improved stability as well as tumour-targeting characteristics (Shukla, et al., 2005). The phytochemicals and bioactive substances such as flavonoids, phenols, terpenes and alkaloids in various plants, act as reducing agents and environmentally benign reservoirs for the production of NPs (Nune, et al., 2009).

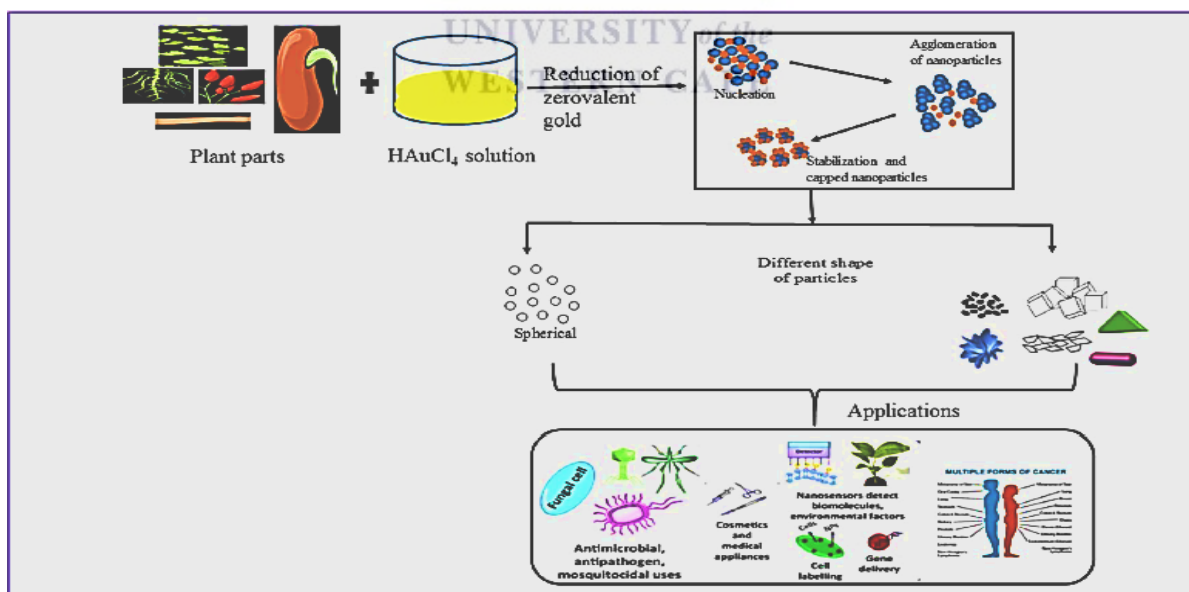


**Figure 1.5:** reactions involved in the green synthesis of gold nanoparticles and their applications (Santhoskumar, et al., 2011).

Plant-mediated NP synthesis has thus become a very promising area in nanotechnology because the plant itself acts as both a reducing and capping agent (Figure 1.4) it has been

shown that plants infer medicinal properties onto AuNPs during the synthesis procedures (Santhoskumar, et al., 2011; Lal & Nayak, 2012; Geetha, et al., 2013).

Abel-Raouf *et al*, successfully produced stable Green-AuNPs from *Galaxuara elongate* (*G. elongate*), an algal extract or powder. *G. elongata*, known to exhibit bactericidal activity, only proved effective against *Methicillin Resistant Staphylococcus Aureus* (MRSA), whereas its AuNP product inhibited the growth of *Escherichia coli* (E.coli), *Klebsiella pneumoniae* and MRSA respectively (Abdel-Raouf, et al., 2017).

Green-AuNPs have also been successfully synthesized from spices. The phytochemicals present in spices inhibit carcinogenesis through their bioactive components which block the activity of cytochrome P450, cyclooxygenase-2 (COX-2) and downregulate signal transducers (Bhagat & Charturvedi, 2016). Cinnamon phytochemical reservoirs have been used to coat AuNPs. These AuNPs showed no cytotoxicity, but displayed high uptake in cancerous cells *in vitro* and *in vivo* and facilitated detectable photoacoustic signals revealing the potential application of the phytochemical coated AuNPs as an excellent photoacoustic contrast agent (Chanda, et al., 2011).

### 1.3.2 Cardamom

Cardamom is a commonly used spice in Indian and Asian cuisines (Mueller, et al., 2010). Two major forms of cardamom generally exists. “Green or true cardamom” (*Elattaria cardamomum*) (Figure 1.6) and “Black or Brown” cardamom (*Amomum subulatum*). It has also been applied as a naturopathic agent against digestive disorders, the common cold, pulmonary tuberculosis as well as gum and throat infections (Sharma, et al., 2011). The large application of cardamom homoeopathically, has led to researchers investigating the *in vitro* and *in vivo* effects of cardamom on various disease pathologies.

The *in vitro* efficacy of cardamom was studied by researchers that encapsulated cardamom essential oil into chitosan NPs. As an antimicrobial agent, the cardamom loaded NPs exhibited excellent potential against extended  $\beta$  lactamase producing E.coli and MRSA. Cytotoxicity analysis indicated non-haemolytic and non-cytotoxic behaviour on human corneal epithelial cells and Human Hepatocellular Carcinoma (HepG2) cell lines (Jamil, et al., 2016). It has also been shown that cardamom ingested as a dietary phytoproduct, displays strong activity against 7,12-Dimethylbenz[a]anthracene (DMBA)-induced skin papillomatogenesis in Swiss Albino mice. The DMBA treated mice experienced blocked

Nuclear Factor Kappa Beta (NFK-B) activation and down regulated cyclo-oxygenase-2 (COX-2) expression resulting in reduction in both the size and number of skin papillomas (Das, et al., 2012). In addition, cardamom is a powerful anti-inflammatory and has been shown to downregulate cytokines such as COX-2, Interleukin-6 (IL-6), Tumour Necrosis Factor-alpha (TNF- $\alpha$ ) and inhibited inducible nitric oxide synthase (iNOS) mediated Nitric Oxide (NO) generation (Kandikattua, et al., 2017).

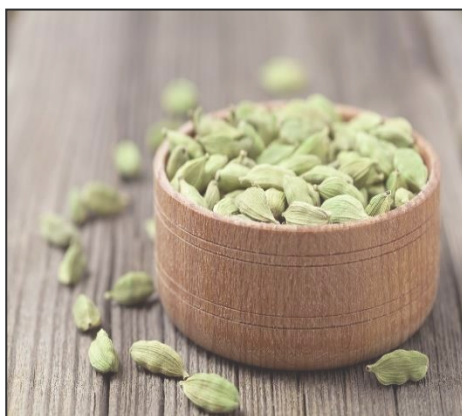


**Figure 1.6:** *Elattaria cardamomum* commonly known as “Green or true cardamom” represented photographically. Image retrieved from [ayurveda.alandiashram.com](http://ayurveda.alandiashram.com)

Research by Rajan *et al* revealed that cardamom synthesized AuNPs (Car-AuNPs) exhibit antibacterial activity against a broad spectrum of bacterial pathogens and that this activity was enhanced against *E.coli*, *Staphylococcus aureus* (*S.aureus*) and *Pseudomonas aeruginosa*. The Car-AuNPs also showed cytotoxicity towards Hela cancer cell lines (Rajan, et al., 2017).

Cardamom extract was also successfully used to synthesize silver nanoparticles (AgNPs). The authors showed that Car-AgNPs successfully inhibited the growth of *S. aureus* and *E.coli*. Car-AgNPs displayed potential as a cytotoxic agent against breast cancer, whilst both types of NPs were effective radical scavengers (Soshnikova, et al., 2017). A study by Singh and Srivastava that used black cardamom, proved that changes in salt concentration ratio as well pH influenced the characteristics of AuNPs. H<sub>2</sub>AuCl<sub>4</sub> quantity clearly affected AuNP size whereas the pH adjustments affected AuNP morphology. Additionally, the study established 1,8-cineole as the bioactive compound responsible for driving the synthesis of Au<sup>3+</sup> to Au<sup>0</sup> (Singh & Srivastava, 2015).

The volatile oil of cardamom is made up of a large number of monoterpenes (97.5%). The monoterpene make-up as characterized by Ali and Husain, consists of seven monoterpene hydrocarbons (9%), three monoterpene esters (1.3%), and seven monoterpene alcohols

(86.7%), of which the predominant monoterpene is 1.8 cineole ( 85.2%) followed by  $\alpha$ -terpinene (2.2%). During the research group's phytochemical investigation, it was discovered that many components of cardamom are highly bioactive and thus required investigations into the chemical and biological composition (Ali & Husain, 2014).

#### 1.4 Radiation Therapy

Over 50 % of patients with malignant tumours receive radiation therapy (RT) as part of their initial therapy, either alone or in combination with surgery and chemotherapy, which makes it an essential tool for curing cancer (Loeffler & Durante, 2013). RT is based on the deposition of energy along the path of incident radiation. In the initial (physical) radiation stage photons/ions interact with the cell, resulting in either direct damage to the deoxyribonucleic acid (DNA) or indirect damage through the generation of secondary low energy electrons, or radicals that can act as intermediaries and damage the DNA (Haume, et al., 2016).

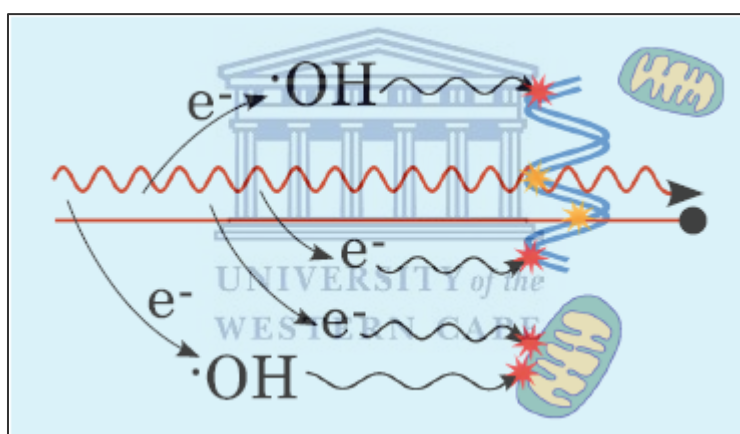


**Figure 1.7** Illustration of mechanisms of radiation damage. Photon radiation (red wave-like line and straight line) may directly damage the DNA (yellow stars) or indirectly damage DNA as well as other cellular components (mitochondria) (Haume, et al., 2016)

Radiation induced DNA strand breaks are integral role players to the fate of the cell leading to cell death or mutagenesis depending on the damage quality and the cell repair ability (Frances, et al., 2010; Taggart, et al., 2014). Radiation can induce a variety of lesions in the DNA: single strand breaks (SSB), double-strand breaks (DSB) formed by two SSB separated by less than ten base pairs distance limit and clustered strand breaks where more than two impairments are located within the mentioned distance limit respectively, on one and two strands (CSB and CSSB respectively) (Francis, et al., 2011).

X- or gamma-rays (photons) are sparsely ionizing and known as low linear energy transfer (LET) radiation. Most of the DNA damage caused by low LET radiation is repairable (Porcel, et al., 2010). LET measures the density of ionization events per unit length along radiation tracks. Densely ionizing (high LET) radiation deposits enough energy to inactivate a cell in one single track, whereas sparsely ionizing radiation (low LET) requires several tracks, each depositing a small amount of energy insufficient to kill a cell, to achieve the same effect (Scalliete & Gueulette, 2017). An adequate dose of ionizing radiation can kill a tumour cell, but the concerns of the amount of damage to healthy tissue residing in the environment surrounding the tumour, limit how much radiation a patient can receive (Porcel, et al., 2014).

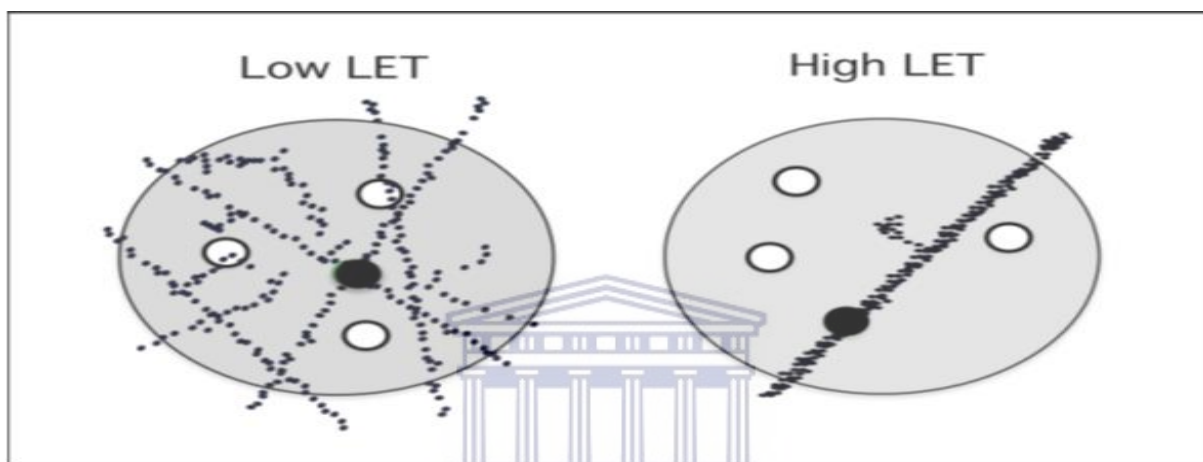


**Figure 1.8** Schematic representation of the difference in radiation tracks. For low-LET radiation, the inactivation of a radiosensitive target requires the conjunction of several tracks, whereas for high-LET radiation the impact of a single track is always fatal (Scalliete & Gueulette, 2017).

Cancer tissues can have, or develop, a resistance to photon radiation; and in addition, due to the physical position of the lesion, it can be difficult to effectively irradiate the tumour completely, leading to its regeneration (Kwatra, et al., 2013). Developments in RT such as particle therapy (proton and carbon ion therapy) are aimed at reducing the amount of normal tissue that is co-irradiated. However, particle therapy is more expensive than conventional therapy and therefore limited to the localized tumours in proximity to critical organs or tumours resistant to conventional treatments.

### 1.4.1 Proton Therapy (PT)

Protons (Hydrogen ions) are positively charged subatomic particles. They possess a unique depth-dose interaction with matter providing dosimetric advantages over X-ray therapy (Mohan, et al., 2013). The clinical rationale for PT is motivated primarily by their inverted depth-dose profile compared to photons. While the depth-dose curve of photons is characterized by a decrease in energy deposition with increasing depth after a short build-up, protons deposit a relatively low dose in the entrance channel (plateau) followed by a steep increase and sharp dose fall-off towards the end of their range in the so-called Bragg peak, beyond which no radiation dose is deposited (Fig 1.9). This allows the positioning of the region of maximal energy within the treatment target, while damage to surrounding healthy tissue organs and tissues is limited (Foote, et al., 2012; Newhauser & Zhang, 2015; Girdhani, et al., 2013; Kim, et al., 2010).

In theory, it also allows higher doses to be administered, potentially reducing the recurrence rate without increasing the complication rate and leading to better organ function and quality of life (Foote, et al., 2012). The effective targeting of PT, combined with the reduced dose in healthy tissue (Figure 1.9 b), is particularly important in the treatment of paediatric cancers in light of the fact that the risk of developing late morbidity or secondary cancers is so much greater in young patients (Mohan, et al., 2013).

Theoretically, the Bragg Peak allows the beam to be pointed directly to a critical structure, increasing the flexibility of PT treatment planning compared to normal photon therapy (Paganetti, 2012). Additionally, the Bragg Peak can be modulated to cover the entire tumour volume. Herein, several proton beams of different energies are combined to achieve the required depth-dose distribution necessary to cover the target volume. This produces a flat region along the Bragg Peak known as the Spread Out Bragg Peak (SOBP) (Figure 1.9) (Britten, et al., 2013; Tommasino & Durante, 2015). The rapid distal drop in dose at the end of the SOBP, is ideal in the treatment of tumours located in close proximity to organs at risk, further compounding the benefits of PT (Marshall, et al., 2016).

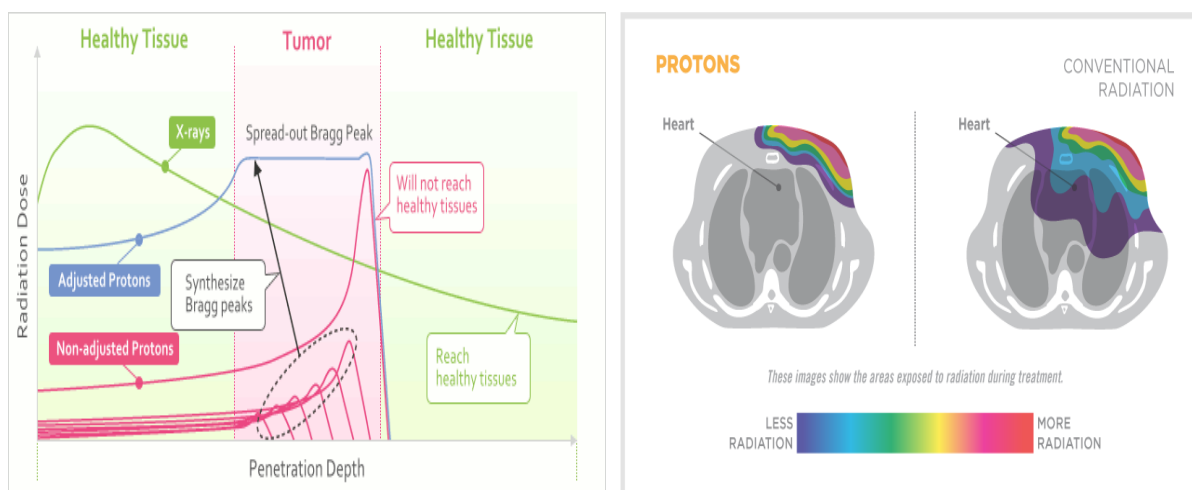


**Figure 1.9:** a) Energy deposition vs depth. The total energy delivered is proportional to the area under the red “protons” curve, The SOBP (Spread Out Bragg Peak) is formed by a suitable superposition of many different mono-energetic proton beams indicated by the blue line. A megavoltage photon beam depth-dosage profile indicated by the green line shows that at target dose depths (10-15cm) the energy is the same as the SOBP. Near the entry point however, photons deposit substantially more energy outside the target depth (Girdhani, et al., 2013). Image excerpted from (Mohan, et al., 2013) b) Colour shaded CT scan depicting the difference in irradiation dose deposition with proton compared to photon irradiation.

#### 1.4.2 Relative Biological Effectiveness (RBE) and Proton Therapy

Comparison between the biological effects of different types of radiation are usually expressed as Relative Biological Effectiveness (RBE). RBE is the ratio of the dose of photon radiation to the dose of a reference radiation that produces the same biological effect. However, the RBE can also be measured within the Bragg Peak region compared to the incident plateau region of an ion energy loss distribution. Protons are known to show a slightly increased RBE when compared to photon radiation and an RBE of 1.1 is currently accounted for in clinical practice compared to 1 for photons (Grün, et al., 2017). However, in the last part of the SOBP, the average proton energy decreases rapidly, leading to an increased linear energy transfer (LET). Paganetti *et al*, (2002) states that the particle type and the underlying dose averaged linear energy transfer ( $LET_d$ ), cell type, biological endpoint and dose level are the main variables to consider in RBE. Values as high as 1.6 in the distal region of the plateau of the SOBP and as high as 2.9 in the distal fall-off being reported by several authors, question the validity of a general RBE of 1.1 for protons in clinical practice (Britten, et al., 2013).

Generally, RBE is considered to increase with increasing LET, whereas it decreases with increasing dose (Villagrasa, et al., 2014). Although protons are generally viewed as low LET, the radiation quality of such proton beams have a high LET component towards the end of their range which could result in an increased complexity of DNA damage, with a possible corresponding decrease in repair efficiency and rise in the number of biologically important unrepaired breaks (Marshall, et al., 2016).

### **1.5 The use of gold nanoparticles as agents for radiosensitization**

The main goal of RT is the delivery of a lethal dose of radiation to a tumour whilst simultaneously sparing surrounding healthy tissue. Great effort has recently been concentrated on the attainment of this goal and has resulted in two distinct categories, the first, conforming the delivered dose to the tumour volume and second, enhancing the sensitivity of the tumour to therapeutic radiation (Polf, et al., 2011). Radiosensitizing adjuvants that enhance the dose specifically absorbed by tumour tissue can result in enhanced tumour killing for any given total radiation dose compared to radiation therapy alone (Dorsey, et al., 2013). Recently, a combination of radiotherapy and NPs have been proposed as a new alternative to improve current treatment protocols (Porcel, et al., 2010).

In a review by Retif *et al*, a clear trend amongst radio-enhancement based studies is defined. High atomic number ( $Z=79$ ) nanoparticles, in the context of radiosensitization, have been found to intensify the production of secondary electrons and reactive oxygen species (ROS) that in turn enhances radiation therapy effects (Retif, et al., 2015). It is thought that the overall treatment dose could be reduced, by increasing the local dose to the tumour through the use of NPs and as a consequence, decreasing side effects (Jeynes, et al., 2014). AuNPs in particular, signify a biologically compatible and safe class of materials that has attracted considerable attention in cancer therapy and imaging (Zhang, et al., 2008), and has been successfully implemented in studies striving to exhibit AuNPs' efficacy as a radiosensitizing agent.

Zhang et al, (2008) used thiol-glucose or sodium citrate capped AuNPs were used to explore the difference in uptake of AuNPs and the subsequent interaction of AuNPs with radiation in prostate carcinoma cells. The research team was able to successfully exhibit cell selectivity for AuNPs capped with thiol-glucose showing a three-fold increase in uptake of these when compared to their counterpart. Furthermore, using an X-ray machine at 220 kVp, a 2Gy dose

was delivered to the cells and a 45.97% inhibition of cell growth was seen in cells exposed to both X-rays and AuNPs. These findings, though valid, also exhibit the progression of the knowledge surrounding AuNP based radioenhancement studies since. Zhang *et al*, remarked that AuNPs less than 50 nm traverse the cell membrane more efficiently than larger AuNPs and that those below 20 nm effectively gain entry to the cell nucleus. However, the contrary has since been proven by Chitrani *et al*, 2010.

An *in vitro* study by Chitrani and collaborators in 2010, investigated radiosensitization by AuNPs as a function of AuNP size, using low energy X-rays. The research group exposed HeLa cells to AuNPs of varying sizes (14 nm, 74 nm and 50 nm) and showed that the greatest level of cellular uptake and radiosensitization was exhibited by the 50 nm AuNPs (Chitrani, et al., 2010).

### **1.5.1 The underlying mechanism of radiosensitization**

The Compton and Photoelectric effect are the main physical mechanisms underlying the interaction between keV X-ray beams and metallic NPs. An incident photon is either partially or fully absorbed by the nanoparticle resulting in the ejection of an electron from the NP surface (Mc Mahon, et al., 2016). Ionizing radiation has enough kinetic energy to detach at least one electron from an atom, NP or molecule, creating ions. Charged particles such as electrons, protons, heavy ions, alpha and beta particles are directly ionizing because they can interact directly with atomic electrons through Coulomb forces and transfer a major part of their kinetic energy directly.

In contrast, photons (X-rays or  $\gamma$ -rays) and neutrons are not charged and therefore more penetrating. They are indirectly ionizing, and have sufficient kinetic energy to free an orbital electron producing a 'fast' recoil or Compton electron that is, in turn directly ionizing. Strong photoelectric absorptions lead to dramatic increases in absorbed dose (Butterworth, et al., 2013). Auger electrons or fluorescent photons are produced by energy released from electrons that drop from higher orbits when replacing ejected electrons. Auger electrons have a much shorter range of coverage but can generate a much higher ionization density at a localized area. Consequently, Auger electrons deposit their energy within the vicinity of the AuNP, which leads to high inhomogenous dose distributions on the nanoscale. Thus it can be anticipated that the combination of radiation with the AuNPs would lead to an enhancement in radiosensitization (Saber, et al., 2017).

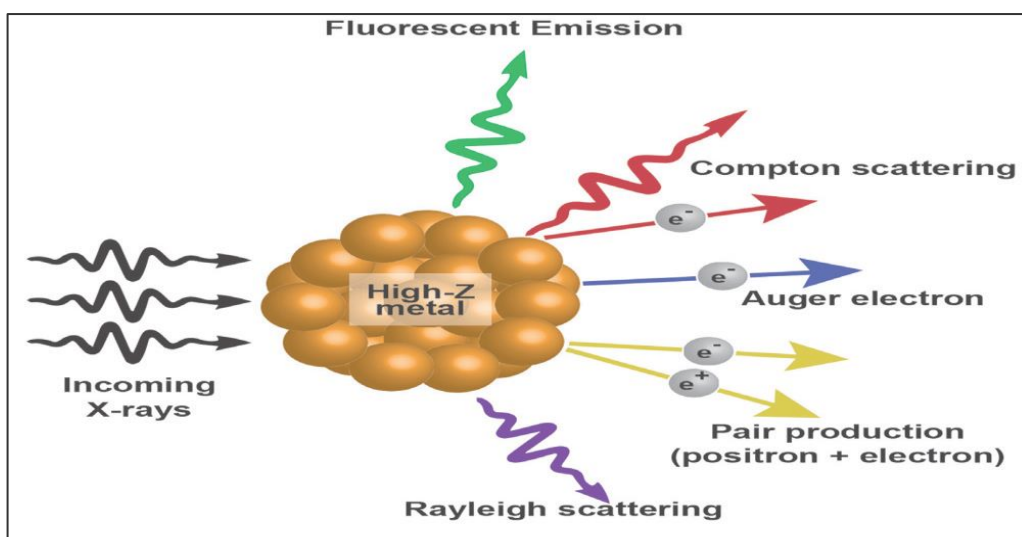


**Figure 1.10:** Schematic depicting electron ejections upon X-ray interaction with high-Z materials (Saber, et al., 2017).

### 1.5.2 Proton radiation and gold nanoparticles

Though AuNPs have been successfully implemented in studies as potential radiosensitizers, most of the current studies are limited to relatively low-energy kilovoltage X-rays. Only a few reports have been carried out with relatively high energy particles that have been used to irradiate cells or tumours containing nanoparticles showing radiosensitization similar to those found in X-rays (Kim, et al., 2010; Jeynes, et al., 2014). Most of the studies show or predict a less pronounced dose enhancement effect with clinical protons compared to low-energy X-rays (Jeynes, et al., 2014). However, kV X-rays have a limited use clinically due to their shallow penetration depth in the patient. From that perspective, protons are a promising candidate for radiosensitization with AuNPs, since the cross-section of high-Z materials to protons is large at clinically relevant energies (>60 MeV). Furthermore, the slightest dose enhancement effect could already impact therapeutic efficacy.

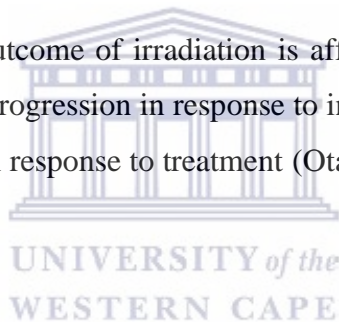
Theoretical work by Verkhovtsev *et al* showed that metal NPs (MNPs) with ion therapy significantly increased the secondary electron yield when compared to that of pure water, due to the excitation of plasmons in the nanoparticle. More specifically, noble metal nanoparticles were shown to be superior to other (e.g gadolinium) NPs (Verkhovtsev, et al., 2015a; Verkhovtsev, et al., 2015b).

A lack of experimental studies investigating proton and AuNP interaction in cells has caused very little validation of previous theoretical simulation findings. However, Kim and co-authors have explored the interaction of various metal nanoparticles and proton radiation and their biological effect. Their research has mainly been centred on particle-induced X-ray

emission (PIXE) or particle-induced gamma ray emission (PIGE) in which it is described that MNPs are activated by high energy particles such as protons and upon activation, release X-rays or gamma-rays (Kim, et al., 2010).

In 2009, Kim *et al* demonstrated that the tumour cytotoxicity of a 45 MeV proton beam was enhanced up to 20-28% by PIXE effects in a proton dose-dependent manner when coupled with administered superparamagnetic NPs. Furthermore, the research group investigated the PIXE effects caused by the interaction between a 2.4 MeV beam and AuNPs, ligand coated AuNPs (L@AuNPs) or Iron NPs (FeNPs) and the bearing this has on tumour cytotoxicity. Both the *in vivo* and *in vitro* study showed increased PIXE effects as NP concentrations were increased *in vitro*. Furthermore, when coupled with a 45 MeV SOBP proton beam, higher concentrations of NP treatment displayed decreased cell survival fractions. Using a tumour regression assay, the obtained *in vivo* results demonstrated significant dose enhancement thought to be due to PIXE effects when compared to conventional proton therapy without NPs (Kim, et al., 2010).

According to Otani, *et al*, the outcome of irradiation is affected by the cell cycle. Thus the biological changes in cell cycle progression in response to insult also requires investigation in order to illuminate effects seen in response to treatment (Otani, et al., 2016).



## 1.6 Overview of the Cell cycle and DNA damage repair processes

The cell cycle comprises four phases in which G<sub>0</sub> is seen as a resting period just prior to the first phase, Gap phase-1 (G<sub>1</sub>). The internal cell cycle signalling system takes over from growth factor (GF) signalling and controls the events of the S-phase, Gap phase 2 (G<sub>2</sub>) and mitosis (M-phase) (Barnum & O'Connell, 2014). Cell cycle progression is subject to control mechanisms.

Key regulators of the cell cycle are proteins called cyclins that bind to cyclin dependent kinases before the kinases can become enzymatically active. (Malumbres & Barbacid, 2009).

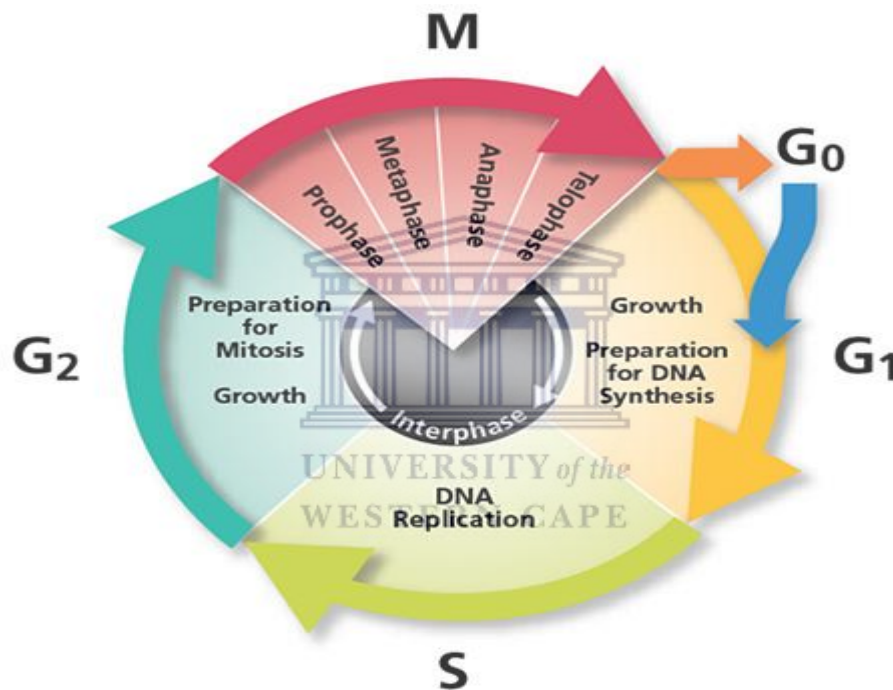


**Figure 1.11:** Diagram depicting the phases of the cell cycle. Image obtained from (Biosciences, 2014)

D-type cyclins (D1, D2, and D3) are key regulators of G<sub>1</sub> progression and formation of active complexes between D-type cyclins and CDK4/CDK6 is subject to regulation by extracellular signals. Cyclin E, in association with CDK2, is required for the G<sub>1</sub>/S transition and cyclin A in a complex with CDK2, is essential for progression through S phase. Lastly, both cyclin A and the B-type cyclins associate with CDK1 to promote entry into mitosis. The mechanisms of CDK regulation consist of positive regulation by cyclin abundance, phosphorylation by CAK (cyclinH/CDK7) and dephosphorylation by phosphatases (members of the Cdc25 family) as well as negative regulation by inhibitory tyrosine phosphorylation through Wee1 and Mik1 (Barnum & O'Connell, 2014). Other controls, termed checkpoint controls, originate

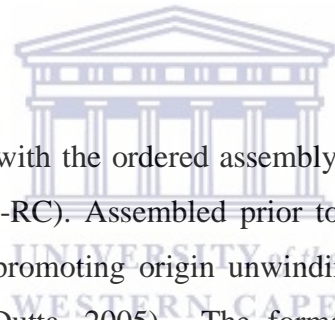
from within the cell and arise from the need to coordinate different cell cycle events, and to halt cell cycle progression in response to irregularities such as DNA damage or faulty spindle assembly (Guo & Hay, 1999).

### **1.6.1 Gap phase 1**

The G<sub>1</sub> phase ensures that the cell is ready to enter the S-phase based on nutrient and growth factor availability (Budirahardja & Gönczy, 2009). Central to its functionality is the activation and inactivation of nuclear phosphoprotein Retinoblastoma (RB). Phosphorylation of RB by CDK 4/6 and cyclin D complex results in the release of the E2F transcription factor (Morgan, et al., 1998) inducing the transcription of genes necessary for the G<sub>1</sub>/S transition and S-Phase (Deckbar et al., 2011; Dubrovnik & Scott., 2000).

### **1.6.2 The S-phase**

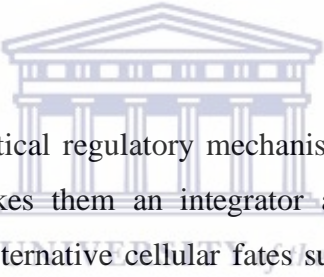
The replication of DNA begins with the ordered assembly of a multiprotein complex called the pre-replicative complex (pre-RC). Assembled prior to the S-phase at origins on DNA, pre-RCs initiate replication by promoting origin unwinding and facilitating recruitment of DNA polymerase (Takeda & Dutta, 2005). The formation of pre-RCs occurs when a multiprotein complex known as the origin recognition complex (ORC), binds the origins on DNA and serve as landing pads for several additional regulatory proteins (O'Connor & Adams, 2010). There are 6 ORCs which are located among six chromosomes. ORC recruits the initiation factors (regulatory proteins) Cdc6 and Cdt1 to origins, which are both in turn responsible for loading the minichromosome maintenance (Mcm2-7) complex. Replication is initiated upon Mcm loading. Pre-RC formation occurs during both early G<sub>1</sub> and late M phases licensing the DNA for replication during the S-phase (Takeda & Dutta, 2005).



### 1.6.3 The G<sub>2</sub>M phase

The second gap phase is another growth phase in which cells prepare to enter mitosis. Mitotic entrance is dependent on the cyclinB/CDK1 complex, activated by phosphorylation by CAK on threonine 161. Hyperphosphorylation of CDK1 on tyrosine 15 and threonine 14 through Wee1 and Myt1 kinases results in a temporary block during which the replicated DNA is checked. Central to this phase of the cell cycle is the (cell cycle division 25) Cdc25 phosphatase family. The inhibitory kinases are removed by Cdc25B and Cdc25C, activating the cyclinB/CDK1 complex (Cappelletti, et al., 2000). Cdc25A generally plays a role in cell cycle transition particularly at the G<sub>1</sub>/S transition and the exit of mitosis (Donzelli & Draetta, 2003). When cyclin B-CDK1 is activated it phosphorylates substrates required for chromosome condensation, nuclear envelope breakdown and formation of the mitotic spindle. On completion of mitosis, cyclin B is degraded via the ubiquitin-proteasome pathway, leading to the dissociation and inactivation of the complex and mitotic exit.

### 1.6.4. Restriction Points



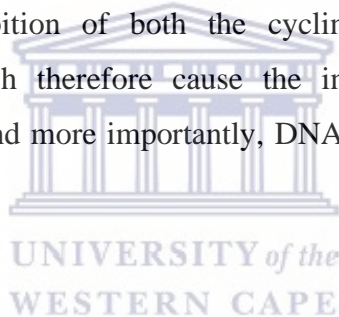
Restriction points are seen as critical regulatory mechanisms allowing a cell to monitor its environment and size. This makes them an integrator and fundamental decision maker controlling the switch between alternative cellular fates such as cell division, temporal cell cycle arrest, quiescence and differentiation (Bartek, et al., 1996). According to the cell cycle stages, DNA damage checkpoints are classified into at least 3 checkpoints: The G<sub>1</sub>/S (G<sub>1</sub>) checkpoint, the intra-S phase checkpoint, and the G<sub>2</sub>/M checkpoint (Murray, 1994). There are more checkpoints such as the spindle checkpoint and morphogenesis checkpoint. The spindle checkpoint arrests the cell cycle at the M phase until all chromosomes are aligned on the spindle (Murray, 1994). This checkpoint is very important for equal distribution of chromosomes. The morphogenesis checkpoint detects abnormality in the cytoskeleton and arrests the cell cycle at G<sub>2</sub>/M transition (Blagosklonny & Pardee, 2002).

#### 1.6.4.1. The G<sub>1</sub>/S checkpoint

The G<sub>1</sub>/S arrest due to DNA damage causes a delay in cell cycle progression to facilitate DNA repair, thus preventing mutations. Entrance into S-phase is regulated by either a p53

dependent or p53 independent pathway (Clémenson & Marsolier-Kergoat, 2009). The p53 independent pathway is known as Cdc25A pathway. These pathways share the same key upstream regulators, ataxia-telangiectasia mutated/ATM and Rad3-related (ATM/ATR) and checkpoint kinases 1 and 2 (Chk1/Chk2) and target Cdc25A, a dual specificity phosphatase and p53 simultaneously within minutes after DNA damage. ATM is mainly activated in response to DSBs, whilst ATR is primarily activated following replicative errors that result in single-stranded DNA (Clémenson & Marsolier-Kergoat, 2009).

Chk2 phosphorylates the Cdc25A phosphatase in several serine residues, which stimulates ubiquitination and proteasome mediated degradation of Cdc25A leading to cell cycle arrest (Zhou & Elledge, 2000). Degradation of Cdc25A inhibits CDK2 activity thus preventing recruitment of DNA polymerase  $\alpha$  and initiation of DNA synthesis (Stracker, et al., 2009). ATM is also responsible for the activation of tumour suppressor protein p53 ( $G_1/S$  arrest maintenance). The activation of p21 by p53 regulates the transition between  $G_1$  and S-phase by interacting with CDK2, repressing the kinase activity of cyclinD-CDK4, cyclinE-CDK2, and cyclinA-CDK2. The inhibition of both the cyclin-CDK complexes leads to the dephosphorylation of RB which therefore cause the inhibition of the E2F dependent transcription of S phase genes and more importantly, DNA damage repair (Zhou & Elledge, 2000).



#### **1.6.4.2. $G_2M$ checkpoint**

The biochemical pathways involved in the DNA damage induced  $G_2$  checkpoints are signalling cascades that unite to inhibit the activation of CDK1. This checkpoint is very similar to the  $G_1/S$  checkpoint. DNA double-strand breaks activate the ATM-Chk2-Cdc25 pathway and DNA lesions such as UV light activate the ATR-Chk1-Cdc25 pathway. Down regulation of Cdc25A, Chk1, Chk2 and Wee1 regulates CDK1 activity and consequently  $G_2$  arrest together with p53/p21, which is distinct from the  $G_1/M$  checkpoint activities. After ATM dependent activation, Chk1 and Chk2 furthermore phosphorylate Cdc25C on Serine 216 creating a binding site for 14-3-3 proteins. Binding of 14-3-3 proteins to Cdc25C, results in the nuclear export of Cdc25C to the cytoplasm thus inhibiting CDK1 activity (Bartek, et al., 1996). p53 is also activated to exert an inhibitory effect on CDK1 via p21 resulting in  $G_2M$  arrest (Graves, et al., 2001; Blagosklonny & Pardee, 2002).

### **1.6.4.3. The Mitotic Spindle Checkpoint**

In both mitosis and meiosis, the spindle checkpoint blocks progression from metaphase to anaphase when more time is required to allow chromosomes to achieve proper bipolar spindle attachment. Spindle microtubule disruption or a compromise in their connection to the kinetochores of chromosomes can delay the onset of anaphase when chromosomes fail to align completely at the metaphase plate. The primary target of the spindle checkpoint is the anaphase-promoting complex or cyclosome (APC/C) (Gorbsky, 2014). An E3 ubiquitin ligase, APC/C catalyses ubiquitination on several target proteins, thus enabling their recognition and degradation by the proteasome. During cell division its most important activator protein is cell division cycle (Cdc20), dually playing a key role within the checkpoint (Pesin & Orr-Weaver, 2008). Seven spindle assembly checkpoint genes (Mad1, Mad2, Mad3, Bub1, Bub2, Bub3 and Mps 1) are known to function at kinetochores to inhibit anaphase onset, or to mediate mitotic exit in the presence of spindle abnormalities (Encalada, et al., 2005). These act as APC/C inhibitors and form complexes in which the main endpoint is Cdc20 inhibition and APC/C inactivation as a consequence of this inhibition, causing a block at metaphase (Sudakin, et al., 2001). When most kinetochores are attached and chromosomes are aligned on the metaphase plate, Mad2 inhibition of APC-Cdc20 activity is ended. The active complex then ubiquitinates securin and allows the activation of separase, which cleaves cohesion. Loss of cohesion triggers chromosome segregation and the onset of anaphase.

The destruction of securin allows the chromatids to separate, while proteolysis of cyclin B allows the cell to exit the mitotic state. The ubiquitin proteolysis of cyclin B is associated with the inactivation of CDK1, initiation of telophase, chromosome decondensation, nuclear envelope reformation, and cytokinesis.

## **1.7 The Cell cycle and radiation**

Rapidly dividing cells, such as cancer cells, are more susceptible to radiation. The inherent cellular kinetics can result in different proportions of cells to be in different stages of the cell cycle at the time of radiation. This can influence the response to radiation treatment. In response to radiation, ATM activation plays an important role. It controls the initial

phosphorylation of several key proteins such as p53, Mdm2, BRCA1, Chk2 and Nbs1 in response to DNA damage (Zhou & Elledge, 2000). These activated proteins all exist as role players in genome integrity preservation and are paramount to the cells fate in the face of DNA damage. DSBs, one of the main causes of ionizing IR damage, is repaired by BRCA1. DNA repair takes place by non-homologous end joining (NHEJ) or homologous recombination (HR) (Sancar, et al., 2004). HR may play a more prominent role during the late S and G<sub>2</sub> stages whereas early S and G<sub>1</sub> DNA repair mechanisms are thought to be dictated by NHEJ (Pawlik & Keyomarsi, 2004).

NHEJ, can occur throughout the cell cycle, predominantly in G<sub>0</sub> and G<sub>1</sub>, and simply ligates the broken DNA. HR effects its repair mechanism by replicating an intact homologous DNA duplex, its requirement of an intact sister chromatid causes most of its operational activity to be within the S/G<sub>2</sub> phase and is the most accurate form of DNA repair. NHEJ is a bit more complex and largely error prone. This is caused by limited processing of the DNA ends resulting in quick but often-times indelicate repair. Ironically, NHEJ largely exerts its effects with the aid of proteins that function as caretakers of the mammalian genome. NHEJ requires the DNA end-binding Ku complex (responsible for initial break recognition), a protein kinase which signals the break in DNA and activates repair proteins at the break, potential DNA end processing enzymes (for example Artemis) and a ligase complex which re-ligates the DNA (XRCC4-Ligase VI complex) (Burma, et al., 2006; Sonoda, et al., 2006).

Throughout the cell cycle a variation in radiosensitivity can be observed. The late S-phase is the most radioresistant, G<sub>2</sub>M is most radiosensitive whilst G<sub>1</sub> takes a more intermediate position. The greatest level of resistance shown by the S-phase may be due to a greater proportion of repair by HR than by NHEJ. Whereas the open structure of DNA might contribute to the radioresistance in G<sub>1</sub>. The high radiosensitivity seen in G<sub>2</sub>M is possibly caused by the poor repair competence (reduced enzyme access) and chromatin compaction (Bohm, et al., 2010). This is also further explained by cells switching off DNA repair during mitosis leading to telomere fusion inhibition (Otani, et al., 2016).

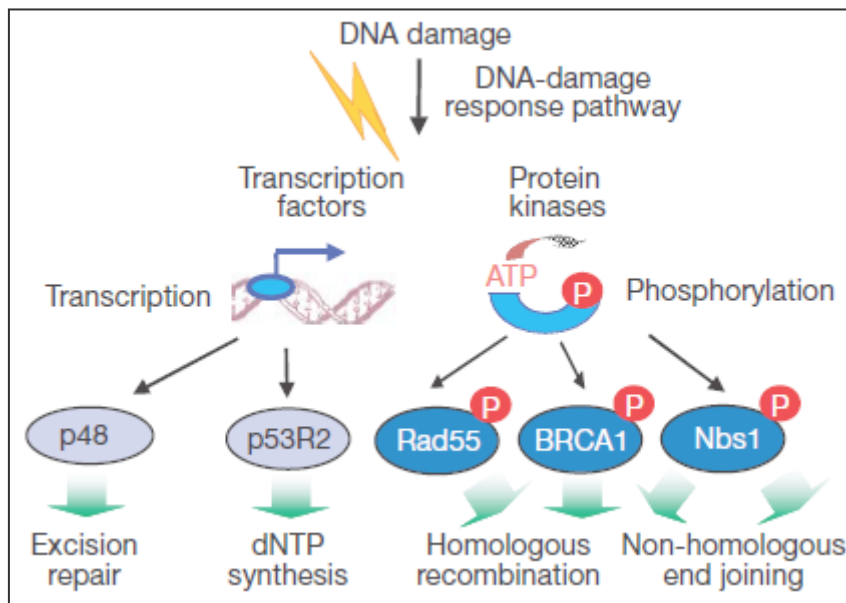


**Figure 1.12:** Interactions between the DNA damage response pathways and DNA repair networks (Sancar, et al., 2004)

## 1.8. The cell cycle and gold nanoparticles

The amount of studies exploring the effect of a particular agent's ability to act in conjunction with radiation and affect the cell cycle has increased greatly. AuNPs are no exception in this regard. A study by Roa, *et al.*, employing glucose-capped AuNPs (Glu-AuNPs) with megavoltage X-rays in prostate cancer revealed a 24% enhancement in radiation sensitivity due to AuNPs. An increase in cells stalled in G<sub>2</sub>/M and to a lesser extent in S-phase could be seen when compared to controls (Roa, et al., 2009). Another study by Geng, *et al* also showed an increase in radiosensitivity in ovarian carcinoma cells caused by Glu-AuNPs. Similarly, a significant increase in the cell fractions in G<sub>2</sub>/M was seen with an increase from 18.4% in Glu-AuNP treated cells in G<sub>2</sub>/M to 40.5% of cells in cells treated with Glu-AuNPs and X-ray irradiation (Geng, et al., 2011).

---

## EXPERIMENTAL AIMS

---

AuNPs have been identified as effective radiosensitizers following bombardment with low energy (e.g. 200 – 500 keV) X-rays, leading to the release of Auger electrons that can induce localised ionising damage to cells.

Since limited studies are currently available on the dose enhancement effect of AuNPs in clinical proton therapy, this project focused on the response of Chinese Hamster Ovary (CHO-K1) cells treated with AuNPs followed by exposure to 200 MeV protons at NRF iThemba LABS, Faure. Two types of AuNPs, synthesized using cardamom (green synthesis) and commercially obtained AuNPs (5, 10 and 50 nm) were used in this study and uptake and cytotoxicity was evaluated for CHO-K1 cells.

The aim of this study was to investigate and compare the interaction between clinical proton treatment and AuNPs by:

- a) Performing time- and dose dependent exposure studies in order to determine the effect of the synthesized and commercial AuNPs on cell survival.
- b) Studying morphological changes induced by the different AuNPs with haematoxylin and eosin staining
- c) Determining the interaction between AuNPs and protons of clinical energy, at various positions in the SOBP, by using the micronucleus assay and clonogenic cell survival assay
- d) Investigating the effects of AuNPs on their own and in combination with proton radiation on cell cycle progression

---

## Chapter 2: MATERIALS AND METHODS

---

### 2.1 AuNPs

#### 2.1.1 AuNP synthesis (Green Chemistry)

Gold nanoparticles were fabricated by means of a bottom up method using *Elattaria Cardamomum* extract as a reducing and stabilizing agent of Tetrahydrochloroauric acid ( $\text{HAuCl}_4 \cdot 3\text{H}_2\text{O}$ ) as described by (Singh & Srivastava, 2015). Parameters such as temperature,  $\text{HAuCl}_4 \cdot 3\text{H}_2\text{O}$  quantity and seed processing as part of extract preparation were varied in order to observe its effect on AuNP synthesis. The solvent volume was kept consistent at 100 ml  $\text{dH}_2\text{O}$  and the general format of AuNP synthesis involving solvent, reducing agent and gold salts ( $\text{HAuCl}_4 \cdot 3\text{H}_2\text{O}$ ) was followed.

#### 2.1.2 Spice preparation and processing

Cardamom seeds sourced locally were removed from the pods. 0.5 g whole seeds or 0.5 g crushed seeds were used in the synthesis. This specific weight was used as preliminary results in our laboratory proved it to yield AuNPs with the narrowest size distribution. 100 ml of  $\text{dH}_2\text{O}$  and the seed pods were added to a glass beaker and the synthesis procedure followed according to the parameter to be varied.

#### 2.1.3 Temperature dependent synthesis

##### 2.1.3.1 Temperatures between 55-85 ° C

The solvent containing the prepared seed pods was placed upon a heat stir plate and allowed to heat up to 55°C, 65°C, 75°C and 85°C respectively. After 5 minutes exposure to a specific temperature, a magnetic stirring bar was added to the heated solution at medium speed and allowed to spin for a further 4-5 minutes. 300  $\mu\text{l}$  of  $\text{HAuCl}_4$  was then added to the solution resulting in an instant observable colour change from golden yellow to wine red or deep purple indicating the reduction reaction of  $\text{HAuCl}_4 \cdot 3\text{H}_2\text{O}$  to  $\text{Au}^{2+}$  and thus AuNP production. For all NP solutions, wine red coloured solutions were considered relatively stable and monodisperse whereas grey and purple solutions were considered to contain a high level of

aggregation as described by (Huang & El-Sayed, 2010). AuNPs employed in stability over time studies were stored at 4°C however, for all other experiments Car-AuNPs were synthesized when required.

### 2.1.3.2 Synthesis at room temperature (RT)

Heatless synthesis required the NP solution to be made up as stated above with the immediate addition of 300 µl of HAuCl<sub>4</sub>. The solution was then left at RT (standard temperature (25°C) and pressure) overnight and the resultant colour change from clear or amber to varying shades of purple or grey was considered an indicator of successful NP production within solution at RT. Thereafter the nanoparticles were filtered using Munktell filter paper (Lasec) to remove any debris and bulk toxins produced as by-products of the synthesis procedure. This filtration method was followed for all Car-AuNP synthesis procedures.

### 2.1.4 Commercial gold nanoparticles (AuNPs).

Citrate stabilized AuNPs (5 nm, 10 nm and 50 nm) were purchased from Sigma Aldrich (Johannesburg, South Africa). AuNPs were stored at 4°C to ensure stability over time and filtered through 0.2µm filters (Whatman, Lasec) just prior to treatment ensuring AuNP sterility prior to treatment exposure.

### 2.1.5 AuNP treatment

The following mathematical scheme was used to determine the volume of commercial AuNP solution that was needed to treat the cells with the required concentration of AuNPs.

The radius was used as a starting point to determine diameter and subsequently derive particle per ml (parts/ml) that is later converted to a given concentration.

$$r = \frac{10 \times 10^{-7}}{2}$$
$$= 5 \times 10^{-7} \text{ (radius of particle in cm)}$$

The radius of each AuNP was adjusted based on the size specifications of the manufacturer.

Next, the volume of one particle in cm<sup>3</sup> is calculated where  $\pi = 3.142$

$$V = \frac{4}{3} \times \pi \times r^3$$

$$= \frac{4}{3} \times \pi \times (5 \times 10^{-7})^3$$

$$= 5.23 \times 10^{-19} \text{ cm}^3$$

The previously calculated volume is then used to determine the mass of the particles where  $\rho$  is the density of Au in g/ml ( $\rho = 19.3 \text{ g/ml}$ );

$$M = V \times \rho$$

$$= 1.012 \times 10^{-17}$$

$$\text{Thus, the number of particles needed:} = \frac{10 \times 10^{-6}}{M} \text{ (for } 10 \text{ } \mu\text{g/ml)}$$

$$= 9.885 \times 10^{11}$$

According to the indicated quantities of AuNPs by suppliers Sigma Aldrich, the number of particles per ml in 25 ml of an AuNP colloidal solution is  $5.98 \times 10^{12}$ .

$$\text{Volume of AuNPs removed to yield } 10 \text{ } \mu\text{g/ml} = \frac{\text{Number of particles Needed}}{\text{Particles per ml of AuNP solution}}$$

$$= 0.165 \text{ (Volume to taken out of bottle to yield } 10 \text{ } \mu\text{g/ml concentration of } 10 \text{ nm AuNP.)}$$

Consequently, the volumes were adjusted to ensure higher concentrations and or different sizes of AuNPs.

## 2.2 AuNP Characterisation

Physicochemical properties of nanomaterials contribute towards their behaviour in biological systems (Treuel, et al., 2014). Characterization of AuNPs is paramount in attaining reliable data with high translational output. Characterization procedures are needed to explain the NPs as chemical species which are highly reactive, with surface charge and particle size most often being identified as the cause for NPs reactivity to constituents in biological environments resulting in effects such as cellular uptake, toxicity and dissolution (Battacharjee, 2016).

### 2.2.1 UV-visible (vis) spectroscopy

By exploiting the principle of SPR, the UV spectrum can be used to draw conclusions about the size and stability of the AuNPs in suspension (Balog, et al., 2015). UV-vis spectra of AuNPs were recorded as function of wavelength using a POLARstar® Omega (BMG Labtech) UV-vis spectrophotometer from 400- 800 nm at a path correlation of 2.94 and resolution of 1 nm.

### 2.2.2 Zeta Potential and Dynamic Light Scattering (DLS) determination

Zeta potential (ZP) analysis is a technique used to determine the charge of nanoparticles within colloidal solutions whilst DLS is a spectroscopic technique used to determine the average hydrodynamic size of nanoparticles (Zimbone, et al., 2011). In order to execute the given characterization methods, 1 ml of AuNPs were placed into cuvettes or capillary tubes for DLS and ZP measurements. AuNP solutions were subsequently analysed using a Zetasizer Nano ZS (Malvern Instruments). Information was retrieved in the phase analysis light scattering mode at 25°C.

### 2.2.3 Stability Testing

Prior to AuNPs interacting with living cells or organisms, their surfaces are confronted with biological fluids such as cell culture medium, lung fluid or blood, whose components will inevitably interact with the NP surface. It is important to precisely understand the behaviour of these AuNPs in biologically relevant surroundings at a basic level which is crucial in developing any kind of nanomaterial of subsequent medical application.

Following a representative model system developed by Balog *et al*, AuNPs were incubated in commonly used buffers and cell culture media for 24 hours reflecting the longest incubation period of the AuNPs within cultures during experimental exposure scenarios (Balog, et al., 2015). Each particle type was incubated in four different increasingly biologically complex media namely (Figure 2.1) i) Phosphate Buffer (PBS) ii) Bovine Serum Albumin (a high molecular weight protein and major component of serum (5 mg/ml) iii) RPMI 1640 medium and iv) RPMI 1640 medium supplemented with 10 % FBS at 25°C and 37°C. Additionally, the naked NPs (green) were tested over time to ascertain their stability in

storage (4°C). Commercial AuNPs were excluded from the time-based stability tests due to its prior stabilization within a citrate buffer thus conferring an established stability over time in storage. Upon the completion of the respective incubation periods, AuNPs were characterized via UV-vis spectroscopy as previously described.

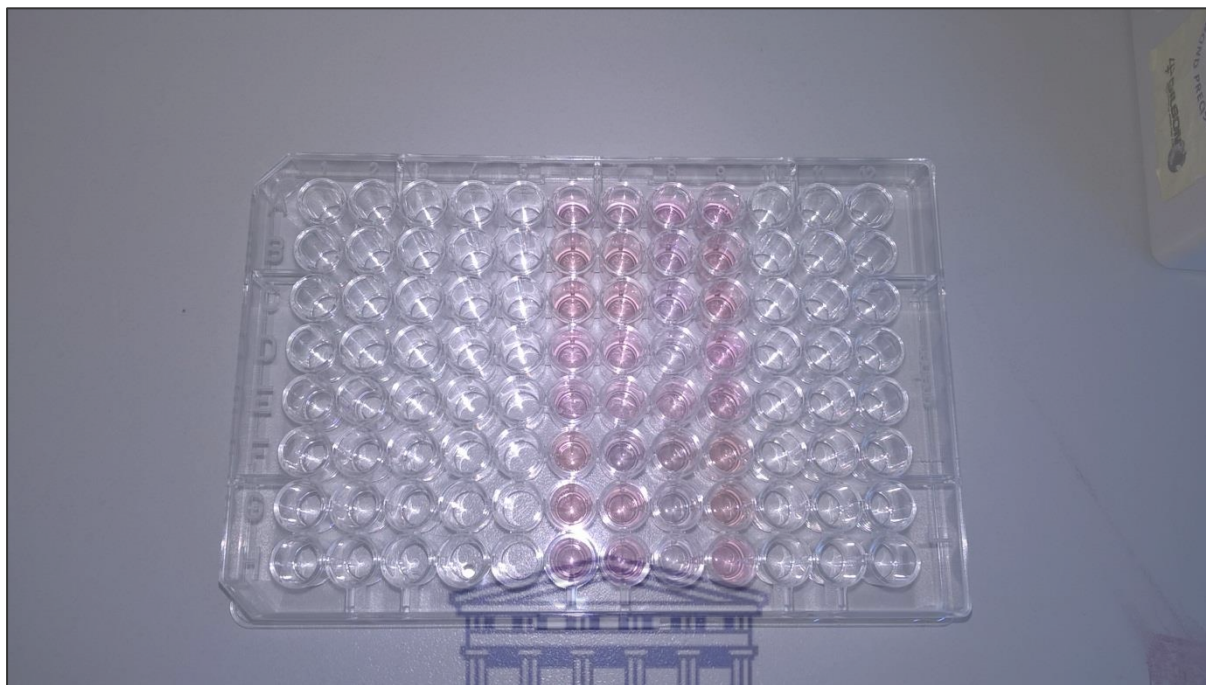


**Figure 2.1:** Example of the colour change in the biological media seen after a 24 hour incubation period at 37°C and 25°C with AuNPs.

#### 2.2.4 Transmission Electron Microscopy (TEM) of the WESTERN CAPE

In order to visually confirm the presence of AuNPs within solution, AuNP samples were prepared as described above at 85 °C with crushed and whole seeds in order to ascertain whether or not seed preparation influenced nanoparticle size and shape. TEM is the most common and accurate technique for obtaining data about AuNP size and size distribution (Amendola & Meneghetti, 2009). TEM was performed at the University of the Western Cape Physics department using a FEI Tecnai G2. TEM images taken of commercial nanoparticles by AuNP suppliers (Sigma Aldrich, Johannesburg South Africa) were used as visual confirmation of AuNP size.

##### 2.2.4.1 Sample Preparation

Samples were prepared by drop-coating 20 µl of AuNP solution onto a carbon coated copper grid and allowed to dry for approximately 10 minutes under a Xenon lamp. Once dried, the samples were analysed under the microscope.

Transmission electron micrographs were collected using an FEI Tecnai G2 20 field-emission gun (FEG) TEM, operated in bright field mode at an accelerating voltage of 200 kV.

#### **2.2.4.2 Energy dispersive X-ray spectroscopy (EDS)**

In addition to image production by TEM via transmitted electrons through the sample, more information can be gained from electrons interacting with the sample. Atoms within the sample produce X-rays as a by-product of their interaction with the transmitted electrons. These X-rays carry information as to the type of atoms present and can be retrieved by changing the detector of the TEM. This information is displayed as a spectrum identifying the elements present as elemental maps (DSimaging, 2013). This technique was used to confirm that the nanoparticles imaged were in fact composed of gold. EDS spectra were collected using an EDAX liquid nitrogen cooled Lithium doped Silicon detector.

### **2.3 AuNP uptake**

In order to determine whether or not AuNPs were endocytosed into the cells, inductively coupled mass spectrometry (ICP-MS) was used. ICP-MS was performed at Stellenbosch University using Aqua Reagia (1:1 HNO<sub>3</sub>, HCL) to dissolve the AuNPs and allow the detection of the quantity of gold atoms in solution and subsequent conversion of this quantity to parts per million (ppm). Quantities yielded were then correlated to the concentrations with which we exposed exponentially growing cells to 2.5, 5 and 10 µg/ml of 10 nm and 50 nm AuNPs. This quantity was then converted to represent the amount of AuNPs endocytosed in parts per billion per cell (ppb/cell).

### **2.4 Proton Radiation**

For the experiments involving high concentrations of smaller AuNPs, cell suspensions were irradiated in sterile 2 ml cryogenic vials (NEST Biotechnology Co., Cat. No. 607101) at 3 different depths in the primary 200 MeV proton beam (collimator aperture: 30 mm diameter, R50 beam range: 100 mm, SOBP: 31 mm). An absolute calibration water tank with Perspex walls was used for this experimental set-up.

The chromosomal damage tests with the larger AuNPs (50 nm), was executed by irradiating the adhered cell monolayer attached to the side wall of the culture flask making it possible to irradiate them in a thin monolayer (<1 mm) perpendicular to the beam direction at 3 positions

along the SOBP, including a position in the distal fall-off which required high precision positioning (Figure 2.2). Culture flasks were irradiated in a phantom consisting of several thin Perspex blocks. Water equivalent depths were simulated by interposing the Perspex blocks of varied thickness in front of the flasks (Figure 2.3). All irradiation exposures were performed at the NRF-iThemba LABS.

All experiments involved some of, or all of the irradiated positions depicted in Figure 2.2. The entrance plateau was included in the bulk of the experiments in which it served as an internal reference/ standard position in order to merge the data from different experiments.

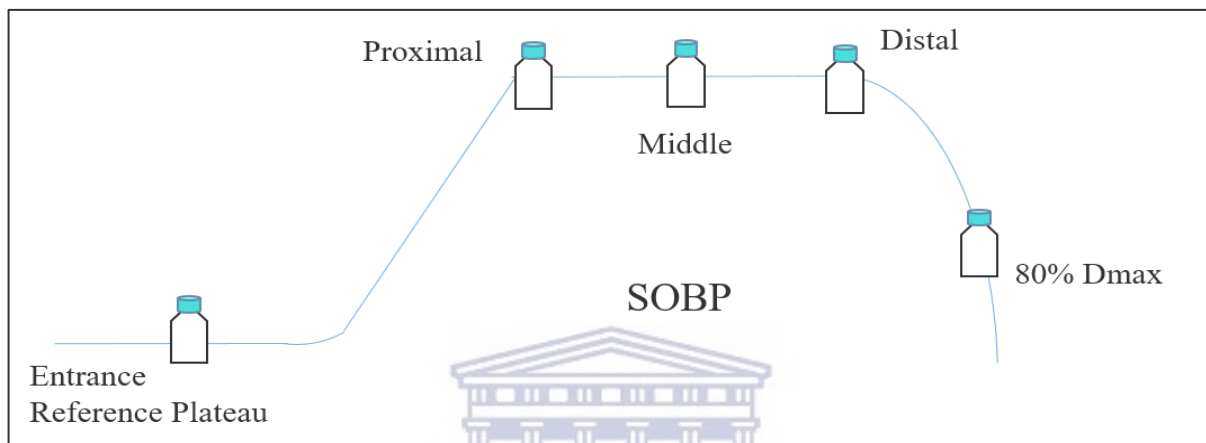


**Figure 2.2:** Schematic depiction of irradiation conditions for proton experiments. Flasks containing the treated and non-treated cell monolayers were irradiated at different depths along the SOBP. The entrance plateau position served as a reference dose to which other irradiated depth conditions were compared.

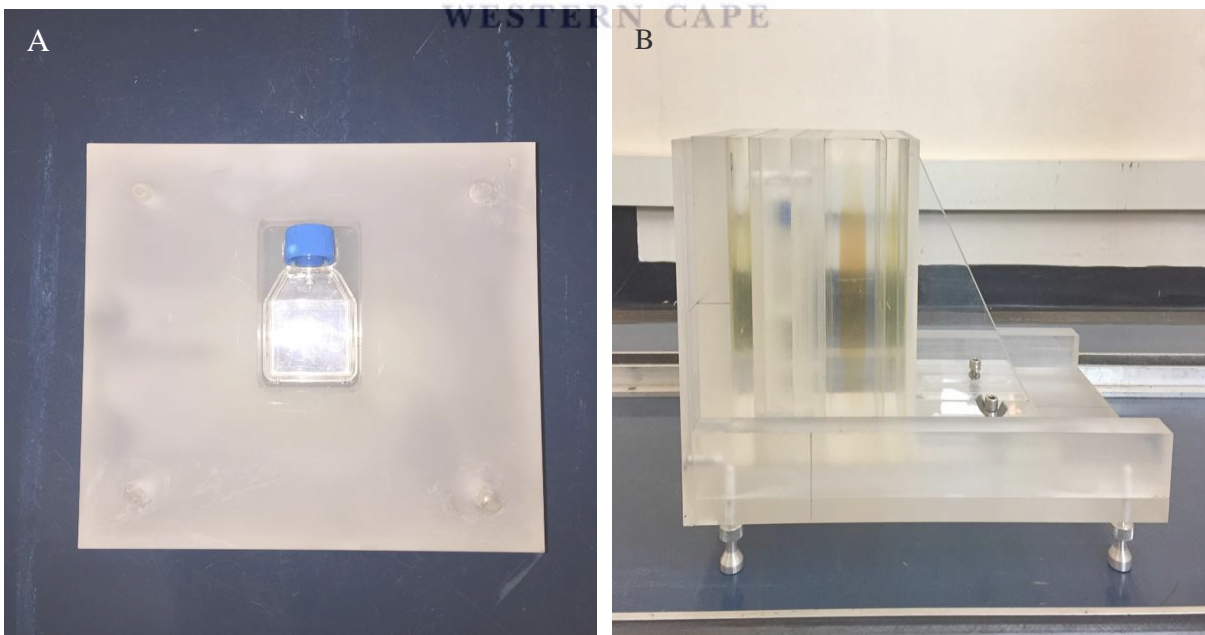


**Figure 2.3:** Images of experimental setups for proton experiments A) shows the Perspex containing the T 12.5 flasks B) shows the perspex walls surround the flasks in it's correct orientation prior to proton radiation

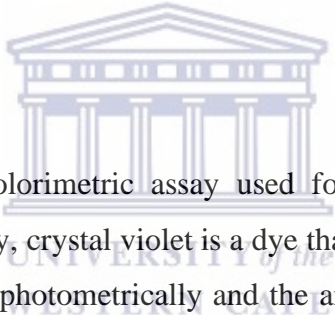
## 2.5. Cell line

Chinese hamster ovary (CHO-K1) cells, an epithelial cells line are derived from ovaries of the Chinese hamsters it is a well-studied cell line in radiation, genetics, toxicity screening, nutrition and gene expression (Wurm, 2004). The CHO-K1 cells were gifted by Prof. J Slabbert (NRF-iThemba LABS, Somerset West, Cape Town).

### 2.5.1 Cell Culture Conditions

CHO-K1 cells were maintained in RPMI 1640 medium, supplemented with 10% Fetal Bovine Serum (FBS) supplied by GIBCO, 1 % Pencillin (100 $\mu$ g/ml) and Streptomycin (100 $\mu$ g/ml), respectively. Cells were allowed to grow under standard conditions of 37°C, 5% Carbon dioxide and 95% humidity prior to harvesting for experimental purposes.

### 2.5.2 Cell Proliferation



The crystal violet assay is a colorimetric assay used for the quantification of DNA in response to treatments. Principally, crystal violet is a dye that accumulates in the cell nucleus. The solubilized dye is measured photometrically and the amount of dye absorbed correlates with the nuclear DNA content and thus with cell number (Vega-Avila & Pugsley, 2011). The optical density observed is converted and expressed as a function of percentage depicting the effect of AuNPs on the proliferative capacity of the cells when compared to controls (expressed as 100 %). Due to the plasmonic nature of AuNPs, the wavelength of AuNPs overlaps with various colorimetric substances resulting in the production false positive or negative results. Due to the absorbance of crystal violet (570 nm) this spectral overlap is prevented as the difference in absorbance is about 10-60 nm in wavelength between the AuNPs and crystal violet.

Due to the doubling time of CHO-K1 cells, 2500 cells/well were seeded into 96-well tissue test plates (TPP) (Sigma Alrich) and allowed to attach and duplicate overnight. Cells were treated with 50  $\mu$ g/ml of the 5 nm, 10 nm and the Car-AuNPs for 4 hours. Quantities of 50 nm AuNPs at a 50  $\mu$ g/ml concentration were determined to yield high volumes of the 50 nm stock solution (refer to mathematical scheme in section 2.1.5). This would result in a high

ratio of AuNPs to media. Distortions in treatment conditions were determined. Following this, 5 and 10 $\mu$ g/ml exposures for 4 and 24 hours respectively, were selected for the 50 nm AuNPs. Cells without AuNP treatment served as controls. Following the respective incubation periods, treatment-containing media was aspirated, and the cells fixed in 100  $\mu$ l of 2.5% glutaraldehyde (Applichem) for 15 minutes. Cells were then stained with crystal violet for 30 minutes and subsequently rinsed with water. The plates were allowed to air dry. Once dry, 200  $\mu$ l of 0.1 % Triton-X (Sigma Aldrich) was added for 30 min in order to lyse the cells and consequently free the bound crystal violet from nuclear constituents. 100  $\mu$ l of the solution was then transferred to a 96-well flat bottom plate (greiner bio-one) and 0.1 % Triton-X added to an additional lane to serve as a blank. The plates were read at 570 nm using a UV-vis spectrophotometer and the optical densities recorded were converted to a percentage to assess changes in cell proliferation.

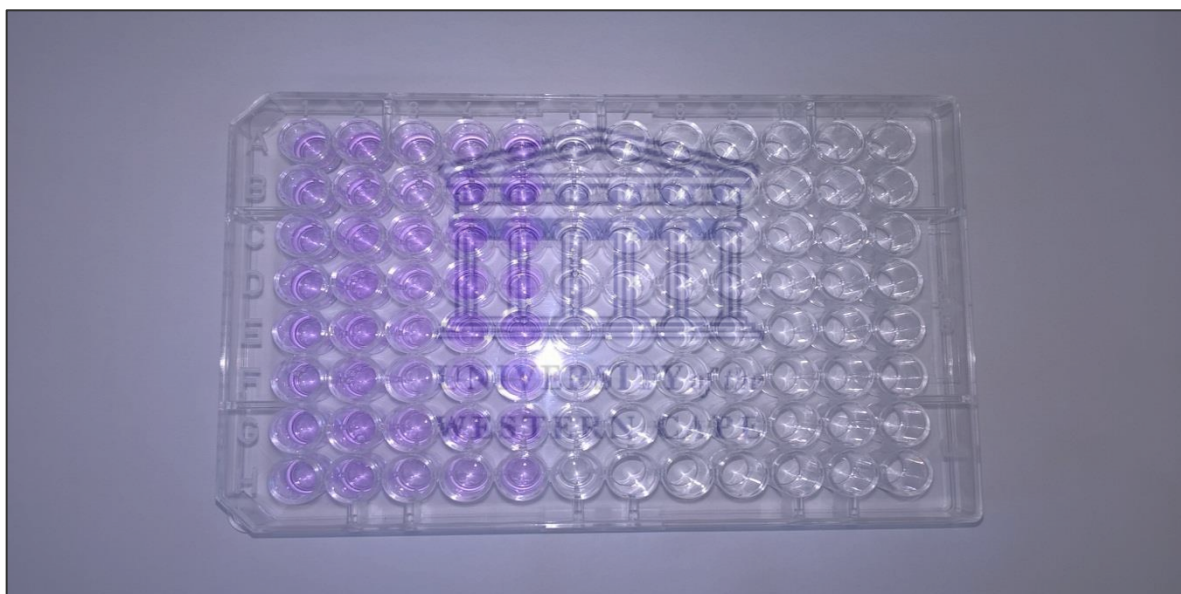


**Figure 2.4: Image of the solubilized crystal violet dye upon addition of the detergent reagent (0.1 % Triton-X).** Purple colour of the dye demonstrates that the wavelength at which optimal absorption will occur will be longer than that of the AuNPs due to where the purple colour lies on the colour spectrum in comparison to the red wine colour of successfully synthesized AuNPs.

### 2.5.3 MTT Assay

The MTT cell viability assay is used to determine cytotoxicity of treatments (Tully, et al., 2000). A water soluble tetrazolium salt, MTT (3-[4,5 – dimethylthiazol-2-yl] - 2,5 diphenyltetrazoliumbromide) (Sigma-Aldrich, Johannesburg, South Africa) is converted to an insoluble formazan (causing a purple colour change) by cleavage of the tetrazolium ring by succinate dehydrogenase within the mitochondria. Due to the permeability of the formazan

product, it only accumulates in healthy tissue and the level of formazan can be directly correlated to viable cells able to convert MTT (Fortakis & Timbrell, 2006). The assay was thus used to assess the effect of 1.8 cineole (active compound in cardamom phytochemical complex), on the cells and determine the optimal treatment concentrations with which to apply 1.8 cineole in order to correlate the effect of the active compound to that of the Car-AuNPs.

According to Murata, *et al*, the 1.8 cineole (Sigma-Aldrich, Johannesburg, South Africa) exhibited inhibitory effects in colon cancer cells (Murata, et al., 2013). Thus concentrations increasing at 5 µl/ml increments from 5-20 µl/ml were explored according to the exposure conditions described by (Murata, et al., 2013). Exponentially growing cells were seeded into 96-well plates, allowed to attach overnight and treated under the aforementioned conditions with the addition of a negative control (cells without AuNP exposure). The experimental protocol outlined by the ATCC® for the MTT assay was used to execute the experiment.

#### **2.5.4 Mitotic Index**

Mitotic index was used to examine the influence that AuNPs and 1.8 cineole had on the morphology and mitosis of the cells. The haemotoxylin and eosin staining method was used to differentially stain dividing cells (for mitotic phase identification) to allow for the quantification of the effects that the change in environment had on cell division.

10 000 cells/ coverslip (flame sterilized) were seeded into six well plates and allowed to adhere to the coverslips within the culture vessel overnight. Coverslips (Lasec) were flame sterilized using 100% ETOH under aseptic conditions. Cells were then exposed to 20µl/ml of 1.8 cineole and 5 µg/ml or 10 µg/ml of AuNPs for 24 hours. Cells without 1.8 cineole and AuNPs were considered controls. Upon completion of the incubation period, cells were fixed in Bouins fixative (Sigma Aldrich) for 20 minutes, washed in 70 % ETOH (Sigma Aldrich) and rinsed in water. This was followed by staining the cells in haemotoxylin (Sigma Aldrich) for 12 minutes followed by a 1-minute rinse step. The cells were then stained in eosin (Sigma Aldrich) followed by another rinse with water for 1 min. Finally, the cells were dehydrated by sequentially placing them in 70%, 90% and 100% ETOH for 2 minutes respectively followed by a final 2-minute exposure to Xylene (Sigma Aldrich). The stained cell containing coverslips were then mounted with xylol (Sigma Aldrich) onto slides (Lasec). 3 Replicates of each exposure scenario were scored using a compound light microscope (Zeiss) at 40× magnification,

The mitotic index was expressed graphically by plotting the percentage of dividing cells using the following equation:  $\frac{(\text{Prophase}+\text{Metaphase}+\text{Anaphase}+\text{Telophase})}{N \text{ (cumulative number of dividing cells)}} \times 100\%$ .

### 2.5.5 Clonogenic cell survival assay

The clonogenic cell survival assay determines the ability of a cell to proliferate and to form a large colony or clone. This is particularly relevant to radiation biology as cells are generally regarded as been “killed” by radiation if they have lost their proliferative integrity, not by whether they physically survive in population (Bohm, et al., 2010). Hence, a cell survival curve can be defined as the relationship between the dose of an agent used to produce an insult and the fraction of cells retaining their ability to replicate (Munshi, et al., 2005).

The clonogenic cell survival assay was used to assess the radiation dose enhancement capabilities of AuNPs and the effect of AuNPs on cell survival. Preliminary experiments provided the plating efficiencies (PE) of the CHO-K1 cells and the effects of AuNPs on the proliferative integrity of the cells upon insult by irradiation. PE refers to the percentage of cells seeded into a dish that finally grow into a colony.

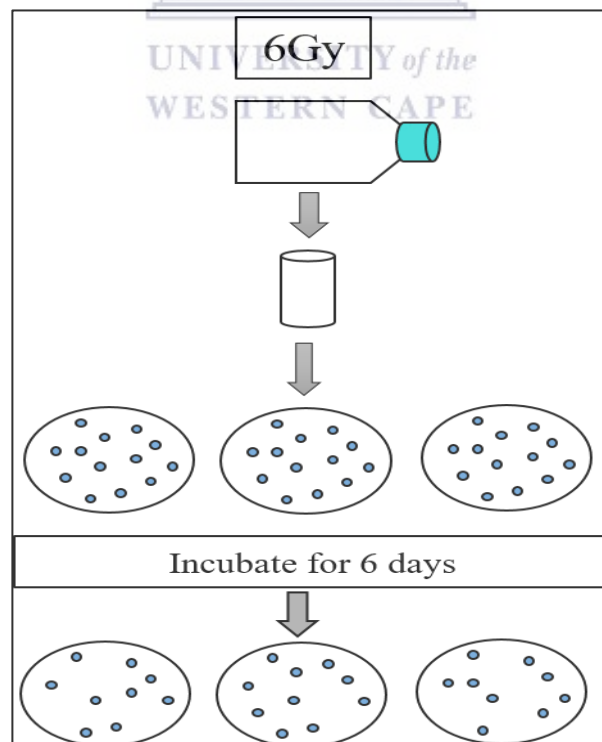


**Figure 2.5:** Graphic depiction of the steps involved in the clonogenic cell survival assay

Preliminary experiments prior to proton irradiation experiments aided in determining the quantities of cells required to compensate for the loss of cells due to irradiation in order to obtain an equal initial quantity of 200 colonies per plate for all samples.

Exponentially growing cells were seeded (750 000/ flask) and allowed to attach. The cells were then treated with a 37  $\mu$ M concentration of 50 nm AuNPs and incubated for 24 hours prior to irradiation. The conditions of the experiment also included a non-irradiated AuNP control along with a negative control containing no AuNPs and no irradiation to determine the PE. Additionally, irradiated controls without AuNPs for all dose points were included. The cells were then irradiated (6 Gy protons) in the entrance plateau, proximal and middle positions of the SOBP. Immediately after irradiation, the cells were trypsinized and counted using a haemocytometer. Cells were then seeded in triplicate (Figure 2.5). Plates containing cells were placed back into the incubator to allow proliferation into colonies ( $\geq 50$  cells per colony) over a period of 6 days. Upon completion of the 6-day period cells were fixed in 1:8:1 acetic acid, water and methanol for five minutes, stained with 0.01% amido black for 30 minutes, washed with fixative and allowed to air dry. The blue stained colonies were then scored by counting all the individual colonies (that met the abovementioned cell number requirements) and the change in surviving fractions in relation to dose, plotted for further analysis.

This high dose of 6 Gy was selected due to the minimal effect on the surviving fractions commonly seen when applying a 4 Gy dose and moreover a 2 Gy dose which is often comparable to the negative control in cell number. Dilution routes calculated using pre-determined plating efficiencies via  $\gamma$ -ray irradiations (Cobalt-60 source) as reference data, were followed and the required quantities seeded accordingly into 3 petri dishes (60 $\times$ 20mm, Greiner).



**Figure 2.6:** Image depicting an example of the colonies upon completion of the CSA assay.

### 2.5.6 Chromosomal damage

The micronucleus assay is one of the preferred methods for assessing chromosome damage because the assay enables the reliable measurement of chromosome loss and chromosome breakage (Fenech, 2000). Micronuclei (MNi) (Figure 2.7) are small extranuclear bodies that stem from chromosome fragments or whole chromosomes that lag behind at anaphase during nuclear division (Vral, et al., 2011). The cytokinesis block micronucleus (CBMN) assay is often used to measure MNi, because scoring is restricted to once divided binucleated cells (BN), which specifically express MNi. This restriction prevents confounding effects caused by suboptimal or altered cell division kinetics (Fenech, 2007). Furthermore, the CMBN method allows for the accumulation of virtually all cells in the BN stage regardless of their division kinetics making the test highly sensitive (Luzhna, et al., 2013).

Exponentially growing cells were seeded into 25 cm<sup>3</sup> (NEST) flasks at 750 000 cells/flask and allowed to attach overnight. Cells were subsequently treated with 50 µg/ml of the 10nm, 5 nm or Car-AuNPs for 4 hours. Immediately prior to irradiation the cells were trypsinized and placed into cryovials (NEST). Cells were irradiated with a 2 Gy dose in suspension within a water phantom. Immediately post-IR, cytochalasin B (Cyt-B) (an inhibitor of microfilament assembly requirement for cytokinesis completion), was added directly to the suspension at a concentration of 1 mg/ml. The Cyt-B containing cell suspensions were consequently seeded into petri dishes (Greiner) containing coverslips. The cells were allowed to grow overnight and were fixed in 3:1 methanol, acetic acid exactly 24 hours after Cyt-B addition and allowed to air dry. Immediately prior to scoring, cells on coverslips were stained with 0.1% aqueous solution of acridine orange (AO) for 1 minute and rinse with Gürr buffer for 1 minute. The stained coverslips were then mounted onto slides (Lasec) using Gürr buffer as a mounting solution. The slides were then scored using a fluorescent microscope (Zeiss), with a FITC filter for optimal visualization of the BN containing MNi.

For the 50 nm AuNPs, the entrance plateau, proximal, middle and distal positions of the SOBP along with the 80% Dmax position in the distal fall-off were used for the irradiation with 2 and 4 Gy proton doses. Exponentially growing cells were seeded at 750 000 cells/flask into 12.5 cm<sup>3</sup> (Flacon) flasks and allowed to attach. The cells were then treated with 10µg/ml (37µM) of AuNPs for 4 and 24 hours respectively. The change in concentration was selected due to the large amount of 50nm AuNPs that would be required within in media to obtain a

50µg/ml concentration. The low media: AuNP solution ratio could possibly result in a high level of cytotoxicity prior to irradiation due to a lack in nutrient supply to the cells. Additionally, a greater level of dose enhancement was expected to be exhibited by the 50 nm AuNPs in comparison to the smaller AuNPs which would effectively saturate the cells with damage and create difficulty visualizing MNi when scoring. Finally, according to findings by Jain, *et al*, AuNPs were shown to have radiosensitization effects at optimal concentrations of 12 µM (Jain, et al., 2011). Thus, the concentration applied in this study was reduced accordingly so that a suitable concentration (in µM) was applied to the CHO cells.

The cells were irradiated as an attached monolayer in a T12.5 culture flask at different positions. Immediately after irradiation cyt-B was added at a concentration of 1mg/ml. The cells were then incubated overnight and 24 hours post-IR trypsinized, centrifuged at 1000 rpm for 8 minutes and permeabilized with 0.045 M cold potassium chloride (KCL). The cells were then centrifuged again and fixed in 1:10:11 acetic acid, methanol and ringers solution overnight. The following day, the cells were pelleted by centrifugation and the fixative aspirated followed by the addition of 10:1 methanol acetic acid fixative resuspension of the cells within the fixative. From this cell suspension, 40 µl was used to drop coat slides and allowed to dry. The slides were then stained with AO by suspending cells in AO, followed by suspension in Gürr Buffer, covered with a coverslip (using Gürr Buffer as a mounting solution) and scored manually using a fluorescent microscope (Zeiss).

Scoring criteria as set out by (Fenech, 2000; Fenech, 2007) were used for the evaluation. Briefly, cells that may be scored for MNi frequency must exhibit the following characteristics; (i) cells should be binucleated (ii) two nuclei should exhibit defined membranes within the same cytoplasmic boundary (iii) the two nuclei should exhibit the same morphological characteristics (iv) a nucleoplasmic bridge connection is allowable to a size range of a ¼ of the nuclear diameter (v) nuclear boundaries should be distinguishable especially in the case of overlapping nuclei and finally (vi) cytoplasmic boundaries of adjacent cells should be individually distinguishable. For each condition the total number of MNi per 500 BN cells per slide, was analysed. All conditions were scored in triplicate and the average per triplicate used to express the change in MNi quantity per condition.

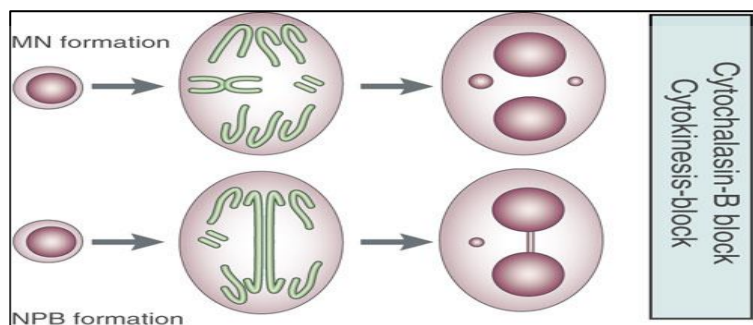


**Figure 2.7:** MNi and nucleoplasmic bridge formation in cells undergoing nuclear division. This is only observable in cells undergoing nuclear division and can be recognized by their BN appearance after cytokinesis blocking with Cytochalasin-B (Cyt-B). Image excerpted from (Fenech, 2007).

### 2.5.7 Interaction Indices

Interaction between AuNPs and protons were suggested by calculating a factor representative of the interaction between the combined treatments. The following equation was applied to data yielded from the CBMN and CSA assays. A sensitization interaction between protons and AuNPs is considered to exist when Unity ( $U$ )  $> 1$ . Conversely when  $U < 1$  no interaction occurred. Unity is the preferred indices as for interaction investigation as outline by Prof. J Slabbert.

$$\text{Unity} = \frac{\text{Combination of Treatment (AuNPs+IR)}}{\text{Separate treatments (AuNPs)+(IR)}}$$

### 2.5.8 Cell Cycle Kinetics

The outcome of irradiation is affected by the cell cycle (Otani, et al., 2016). In this study, flow cytometry was used to determine the combined effect of AuNPs and protons on the cell cycle. Flow cytometry enables the identification of cell distribution during various phases of the cell cycle. Discrimination between the phases of the cell cycle is based on their respective DNA contents made distinguishable by a fluorescent dye, propidium iodide (PI) which binds stoichiometrically to DNA. Principally, the stained material has incorporated an amount of dye that is directly proportional to the amount of DNA within the cell population (Nunez, 2001). Different quantities of DNA are expressed during the different phases of the cell cycle making the aforementioned distinction possible. The flow cytometer operates by introducing cells into an artificial flow and hydrodynamically focusing them into a single file. Laser induced fluorescence and/ or scattered light reflected off cells can be detected by photodetectors (Figure 2.8) (Tanev, 2009). Slight deflection of some of the photons that hit the edge of the cell (forward scatter) corresponds to the size of the cell, whereas photons scattered at right angles to the cell indicate the inner complexity and granularity of the cells (Dhawan & Sharma, 2010). A resultant dot graph representing the respective amounts of scatter is then plotted by the flow cytometer and replotted into a histogram depicting the different phases of the cell cycle and the extent to which a treatment induces accumulation of cells in a specific phase.

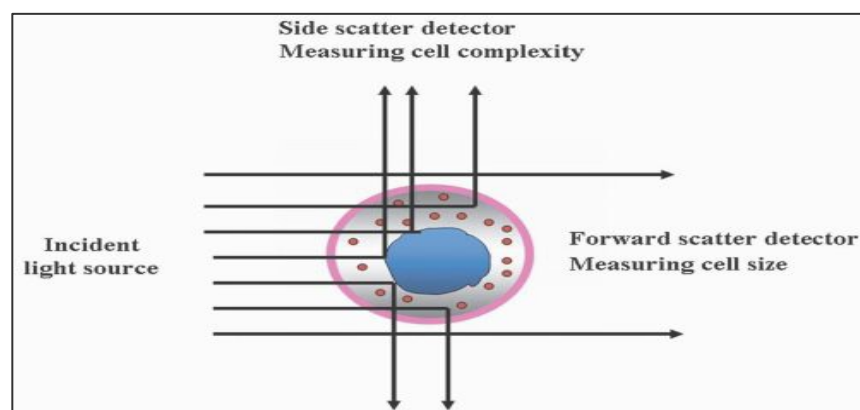


**Figure 2.8:** Graphic depiction of forward and side scatter used to measure cell size and inner complexity within a flow cytometer. [www.oncohemakey.com](http://www.oncohemakey.com)

1×10<sup>6</sup> cells were seeded into 25 cm<sup>3</sup> flasks and allowed to attach overnight. The cells were then exposed to 50 µg/ml of 5, 10 or 50 nm AuNPs for 4 hours prior to irradiation or 10 µg/ml of AuNPs, 24 hours prior to irradiation. Upon exposure to the AuNPs for the allotted time frames, media containing the AuNP suspensions were removed and the cells replenished with fresh media. Cells were then irradiated with a 6 Gy dose of protons at the reference position, entrance of the SOBP, middle of the SOBP, the proximal end of the SOBP and the 40% Dmax position (distal fall-off). Cells were then returned to the incubator immediately after irradiation and allowed to incubate for 8 hours. Upon completion of the 8 hour time frame, cells were harvested, concentrated by centrifugation for 6 minutes at 900 rpm. This was followed by membrane permeabilization using 5 ml of ice-cold 95 % ethanol (EtOH) which also served as a fixative in which the cells were stored at -20° C overnight. Subsequently the EtOH was removed by centrifugation at 1400 rpm for 5 min (25° C). The cells were then washed with PBS (pH7.4) twice and the cells concentrated followed by the removal of supernatant from the pellet to which 1 ml of propidium iodide (PI) was then added and the cell pellet resuspended within the PI. The cell suspensions containing the PI, was left for 10 min at RT prior to analysis with the flow cytometer.

A BD ACCURI-6 flow cytometer was used to analyse the cells employing a 488 nm laser and recording 10 000 events per sample. The BD ACURRI 6 software was used to apply a gate to the resultant plots that were consistent for all cell populations. Data collected was subsequently analysed according to scatter as described by Dhawan & Sharma in which it is explained that the changes in side scatter detected can be directly correlated to AuNP uptake (Dhawan & Sharma, 2010). Furthermore, according to Roa, *et al.*, RCGG is a parameter that depicts the cell status at the time of radiotherapy and is derived based on the measured cell changes due to AuNP treatment. RCGG can thus be used to deduce cellular radiosensitivity. Hence, the most sensitive and radioresistant phases of the cell cycle is taken into account. With a modification on the calculation provided by (Roa, *et al.*, 2009), with the S-phase in lieu of the G0/G1 phase being selected as the most radioresistant phase, RCGG was calculated by:

$$\text{RCGG} = \frac{\text{Value of G2M phase (\%)}}{\text{Value of S-phase (\%)}}$$

RCGG allows several derivations, the first, that a greater G2M leads to a larger RCGG, a smaller S-phase leads to a larger RCGG and a larger RCGG indicates a greater level of

radiosensitivity when compared to controls. RCGG was thus calculated in order to determine whether the AuNPs were able to effectively sensitize the cells when compared to cells that received protons without AuNPs.

## 2.6 Statistical Analysis

### 2.6.1 Cell Proliferation, MTT assay and Clonogenic cell survival assay

GraphPad Prism 5 statistical analyses software was used to perform statistical analysis on data yielded from the crystal violet assay (GraphPad Prism version 5 for Windows, GraphPad software San Diego, California, USA). Predetermined standard deviations (Excel 2013) were used to plot error bars within the data and two-way analysis of variance (ANOVA) along with Bonferonni post-tests (post hoc) were used to obtain whether statistically significant differences existed among the exposure scenarios when compared to their controls and one another. Herein, variation between groups were considered statistically significant when p values were less than 0.05 ( $p < 0.05$ ), highly significant when  $p < 0.01$  and extremely significant when  $p < 0.001$ .

### 2.6.2 Mitotic Index

The statistical analysis of mitotic index was completed via Medcalc (Schoonjans et al., 1995) (version 14.8.1). One way analysis of variance (ANOVA) was used to determine the significant differences between the control means and experimental groups. Error bars of  $\pm 2$  standard deviations (SD) were used to show the influence of AuNP types on each sample in an experiment group. Student Newman Keuls tests were performed for all independent and pair-wise comparisons and results were considered statistically significant if  $p < 0.05$ .

### 2.6.3 Radiation Damage

The radiation damage data from the CBMN assay was analysed at Stellenbosch University by Professor M. Kidd using Statistica. The data was assessed for normal distribution and subsequently analysis using the Kruskal-Wallis test to compare the means. Vertical bars on the data points were used to denote 0.95 confidence intervals whilst alphabetical letters were used to indicate statistically significant differences between means. For example; samples that were both labelled **a** do not statistically differ from one another. Samples labelled **a** and **ab** or **bcd** and **abc** were significantly different statistically indicated by the difference in

alphabetic letters and letter arrangements. Samples were considered statistically significant when the determined p-value was lower than 0.05 ( $p < 0.05$ )



---

## CHAPTER 3: RESULTS

---

### 3.1 Gold Nanoparticle Characterisation

Car-AuNPs were synthesized by adjusting the parameters (temperature and degree of mechanical crushing of cardamom seeds) of the synthesis procedure in order to ascertain whether the shape and size of AuNPs are dependent on these parameters. The colours of the Car-AuNPs showed the same red hue when compared to the commercial AuNPs (Sigma Aldrich). Due to the unique optical properties of AuNPs, their UV-spectrum results in a particular ruby red colour when AuNP suspensions are stable (Huang & El-Sayed, 2010).

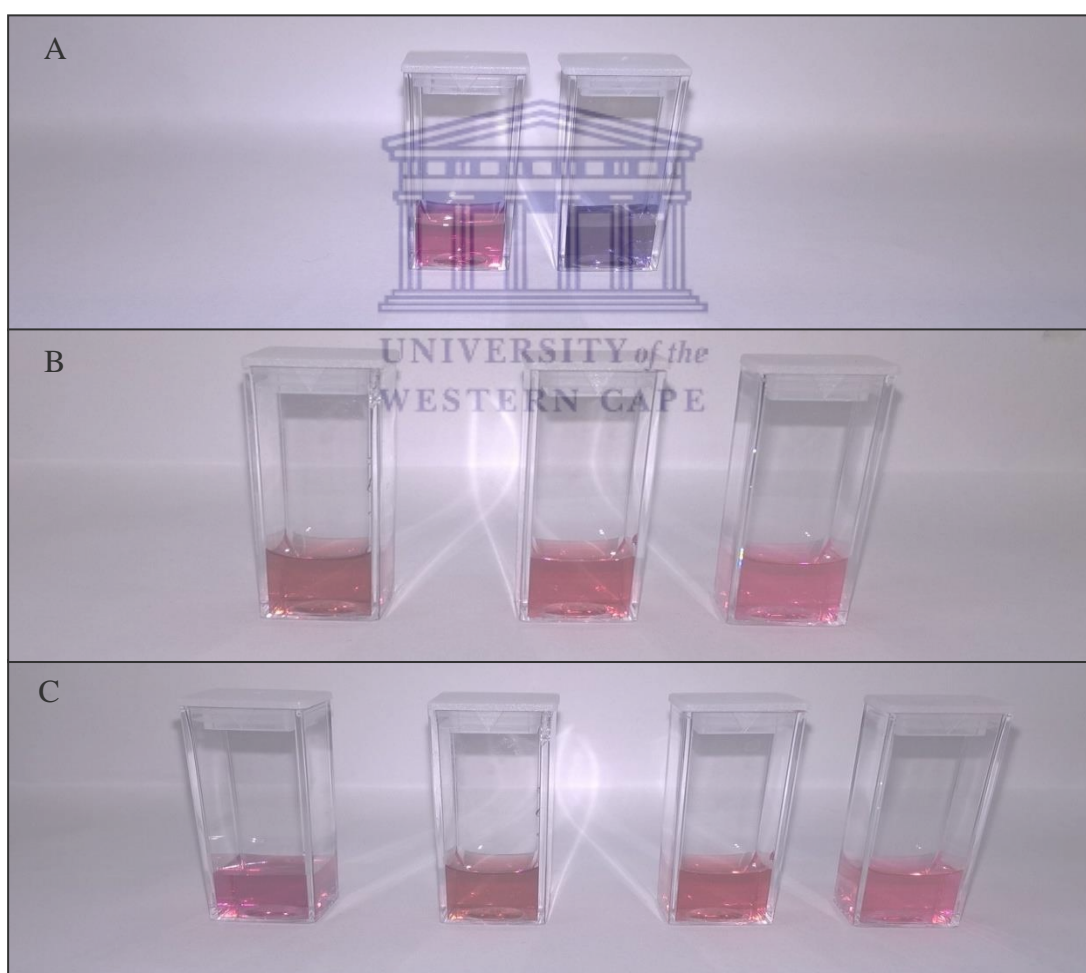


**Figure 3.1: Images depicting various AuNP colloidal solutions used for treatment** A) the difference between AuNPs synthesized by crushed (left) and whole (right) cardamom seed pods at 85°C B) Commercial AuNPs (from left) 5nm, 10 nm and 50 nm C) difference in colour of colloidal solution (from left) Car-AuNP, 5 nm AuNP, 10 nm AuNP and 50 nm AuNP

### 3.1.1 Ultraviolet Spectrophotometry

The absorption of each AuNP solution was measured via UV-vis spectrophotometry for the analysis of surface plasmon resonance (SPR) to determine AuNP presence, as well as approximate size and quantity (Huang & El-Sayed, 2010). SPR properties of AuNPs allows the determination of agglomeration levels based on the maximum wavelength at which AuNPs absorb light. The influence of AuNP size on SPR is affected by the absorption maximum ( $\lambda$  max) which increases from 520 nm to 570 nm for 20 nm AuNPs and 100 nm AuNPs respectively (Huang, et al., 2006). Therefore this increase in AuNP size red shifts the SPR wavelength and also increases the intensity (absorbance). The expected SPR peak for AuNPs that are uniform in size and shape is thus narrow and normally appears in the visible region starting at 520 nm (Huang & El-Sayed, 2010; Salata, 2004).

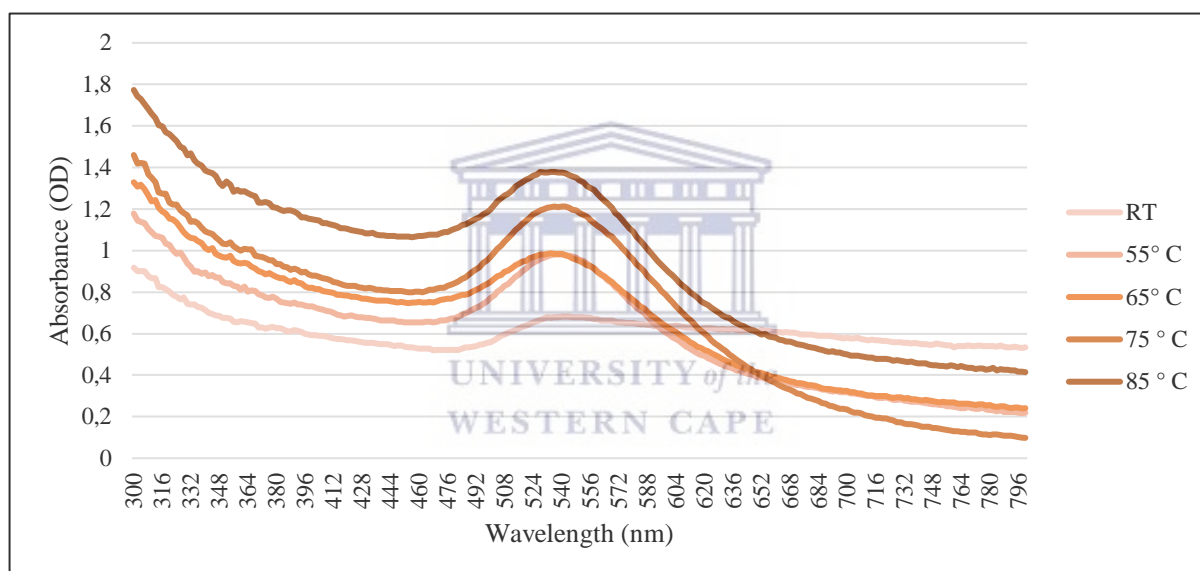


**Figure 3.2: The effect of temperature of the synthesis reaction on AuNP product.**

Figure 3.2 shows that AuNP synthesis using crushed cardamom seeds provided the product with the greatest level of stability, absorbance and narrowest SPR band width at 85°C. The result showed that the optimum synthesis temperature for Car-AuNPs was **85°C**.

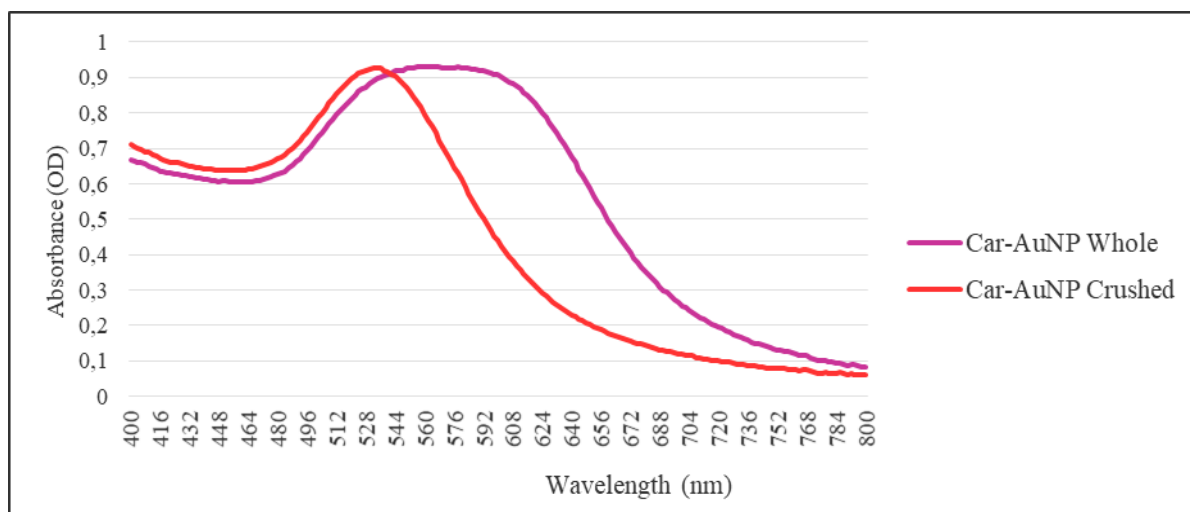


**Figure 3.3: UV absorption spectra of Car-AuNPs.** Car-AuNPs synthesized from crushed and whole cardamom seeds at 85°C, showed a clear difference in AuNP quality as depicted visually and via a difference in absorbance. The absorbance of Car-AuNPs (crushed)  $\lambda$  max at a wavelength of 525 nm whilst the Car-AuNPs prepared by extract with whole cardamom seeds had a  $\lambda$  max of 590.

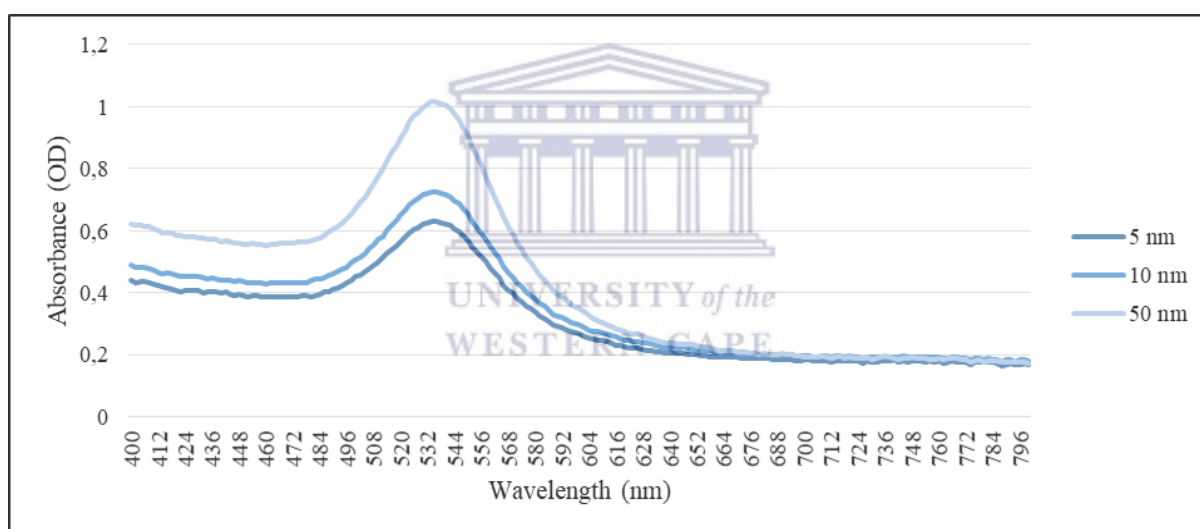
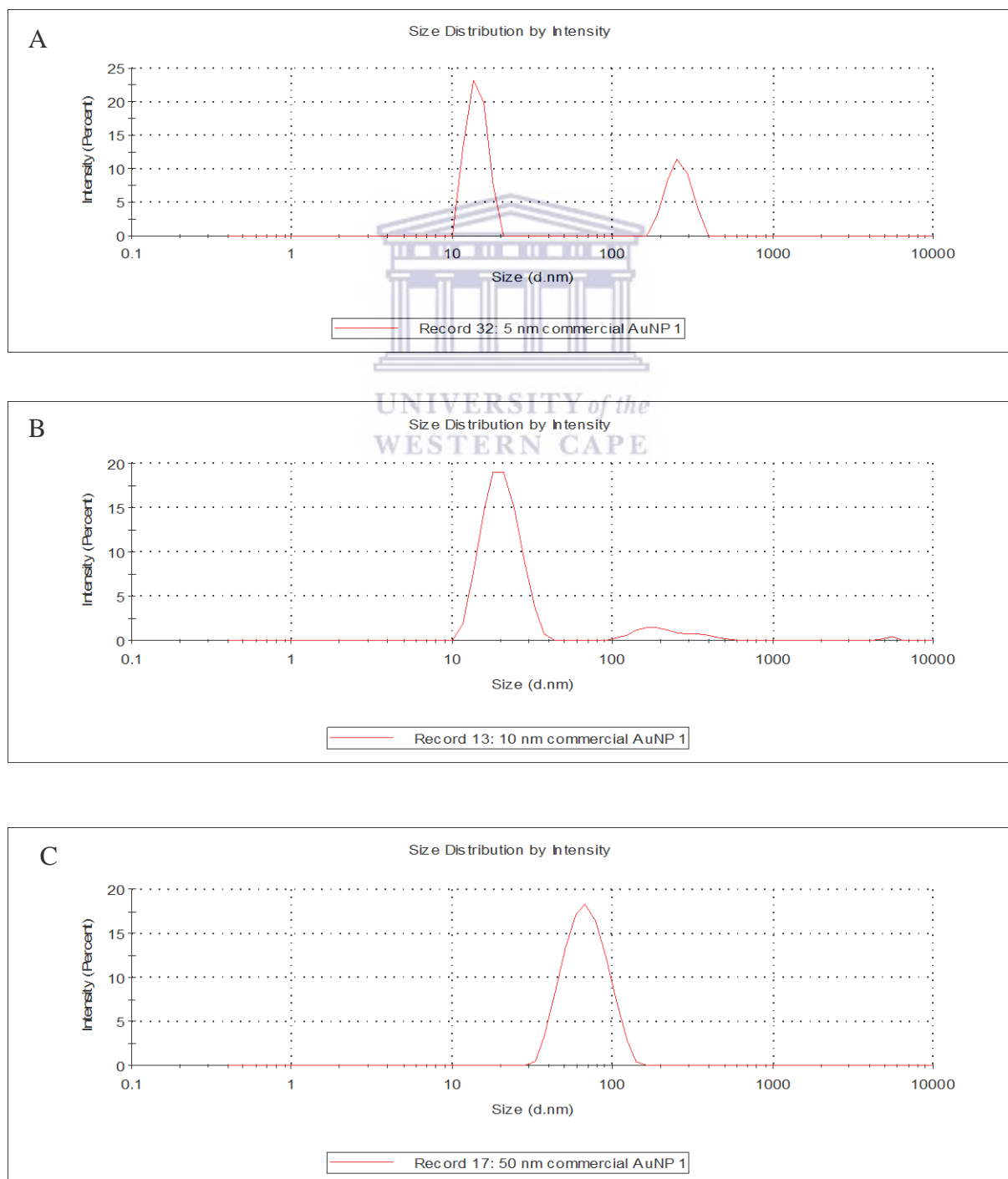


**Figure 3.4: UV absorption spectra of 5, 10 and 50 nm AuNPs.**

The  $\lambda$  max of 50 nm AuNPs was recorded at 536 nm, whilst the 5 and 10 nm AuNPs measured 542 and 544 nm respectively (Figure 3.4). The larger  $\lambda$  max values of the 5 and 10 nm AuNPs indicates that agglomeration was present within the AuNP solutions whilst the  $\lambda$  max value of the 50 nm AuNPs shows that the 50 nm AuNPs were stable.

### 3.1.2. Dynamic Light Scattering

DLS was used to determine the hydrodynamic sizes of AuNPs within suspension and obtain the level of dispersity in the size of the AuNPs expressed as an index known as the polydispersity index (PDI). “Monodisperse” AuNPs usually have narrow PDI ranges within values of 0.0-0.1. “Polydisperse” NPs measure within a range of 0.1-0.4 and are considered moderately disperse within this range whilst a broad level of dispersity is usually denoted by PDI values that are greater than 0.4 (Nobbmann, 2014). The size distribution curves obtained are shown in Figure 3.5.



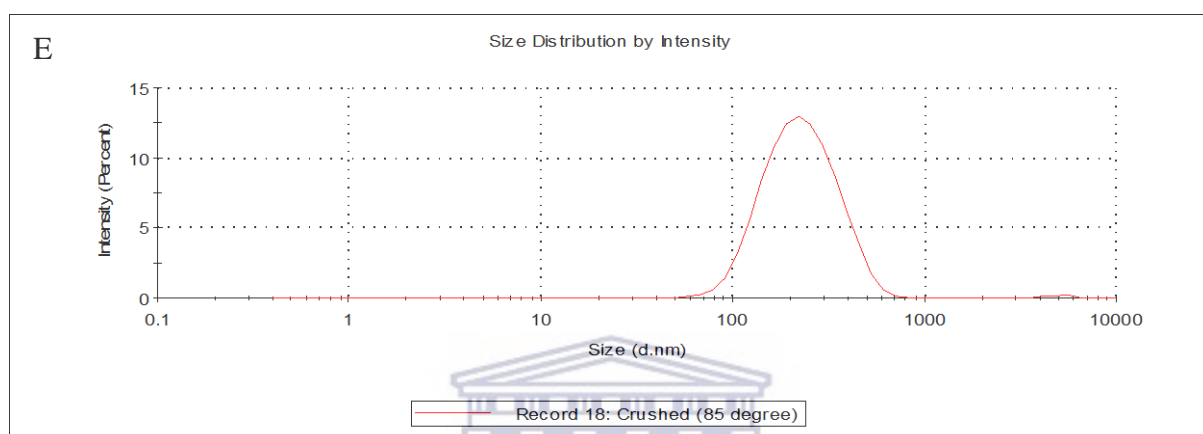
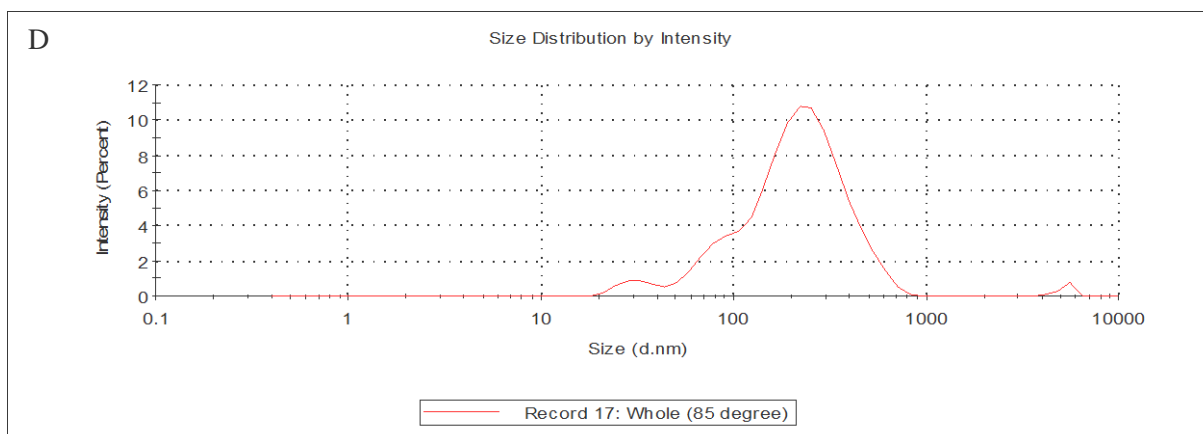


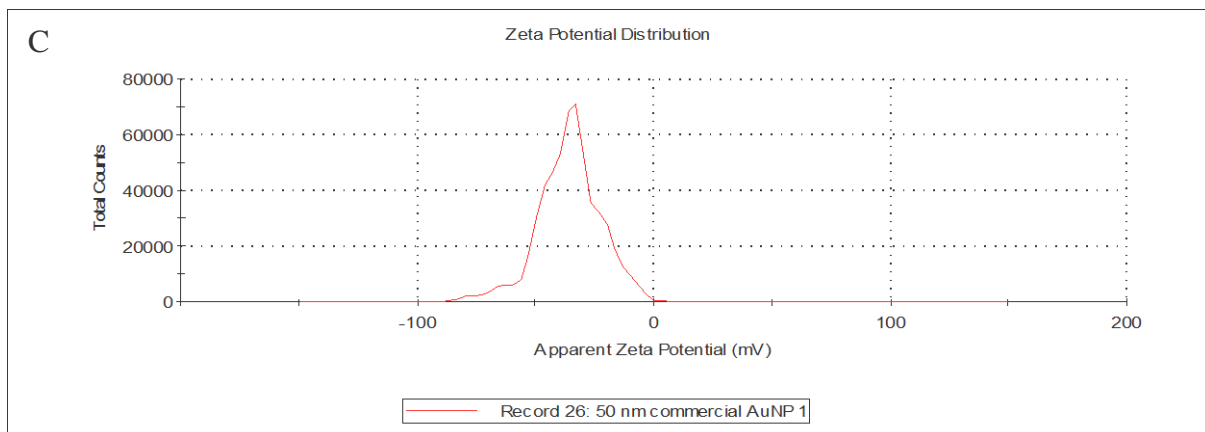
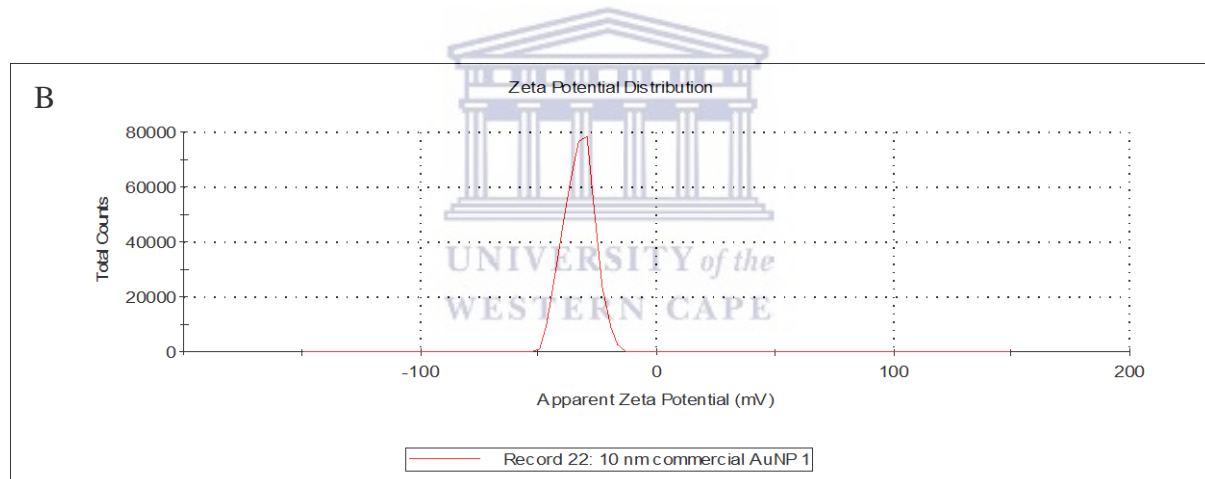
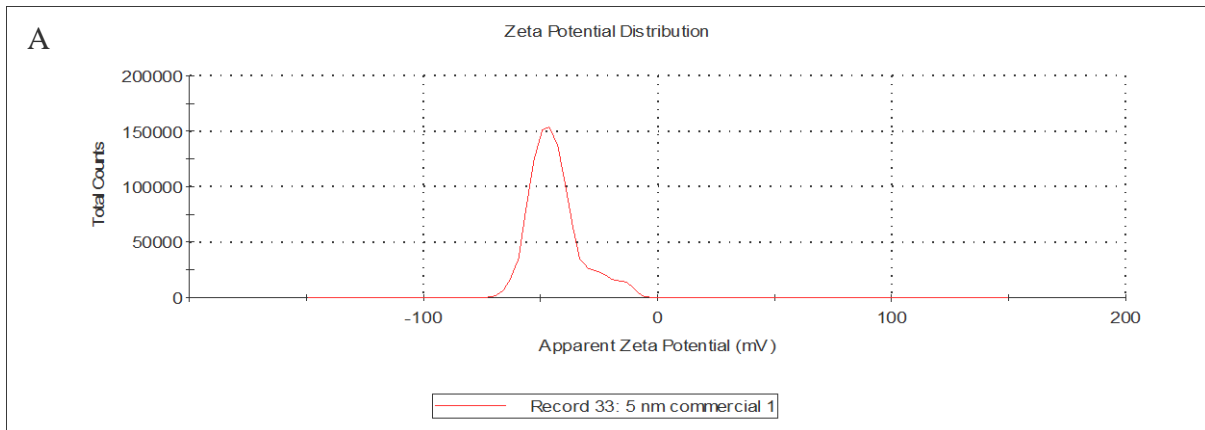
**Figure 3.5: The hydrodynamic sizes of AuNPs.** A) 5 nm AuNPs B) 10 nm AuNPs C) 50 nm AuNPs D) Car-AuNPs (whole seed extract) E) Car-AuNPs (crushed seed extract)

UNIVERSITY of the  
WESTERN CAPE

Results depicted in Figure 3.5 A represent the DLS measurements obtained for the 5 nm AuNPs. 5 nm DLS results show AuNPs that are polydisperse. However the analysis of the two peaks indicate that the majority of the AuNPs in solution are within the 10 nm range (Figure 3.5 B) (smaller sizes are usually more difficult to detect with DLS) indicating that the true size of the AuNPs are indeed 5 nm. The 10 nm and 50 nm AuNPs single DLS curves indicate moderate and narrow levels of size dispersity within the samples. The size distribution curves of the Car-AuNPs confirm the previously reported difference in quality of the AuNPs yielded via synthesis with extract of different seed preparations. The distribution curve for the crushed Car-AuNP (Figure 3.5 E) showed that the difference in extract preparation resulted in better AuNP size dispersions when Car-AuNPs were prepared with extract from crushed seeds rather than whole seeds (Figure 3.5 D).

### 3.1.3. Zeta Potential

The determination of surface forces on the surface of the AuNPs provides crucial information on the stability of the particles in dispersion. The magnitude of the ZP is predictive of the colloidal stability and NPs with a ZP greater than + 25mV and less than – 25mV, typically have high degrees of stability (nanoComposix, 2012).



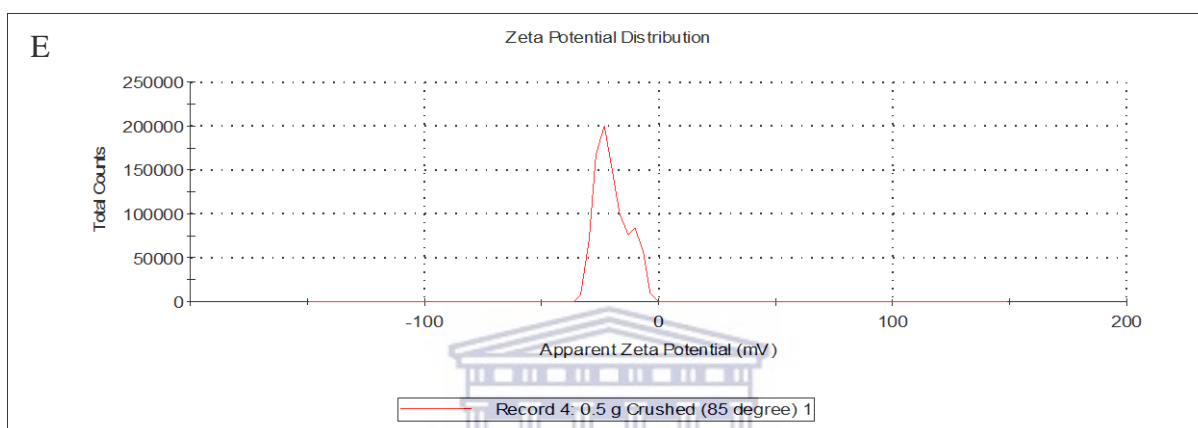
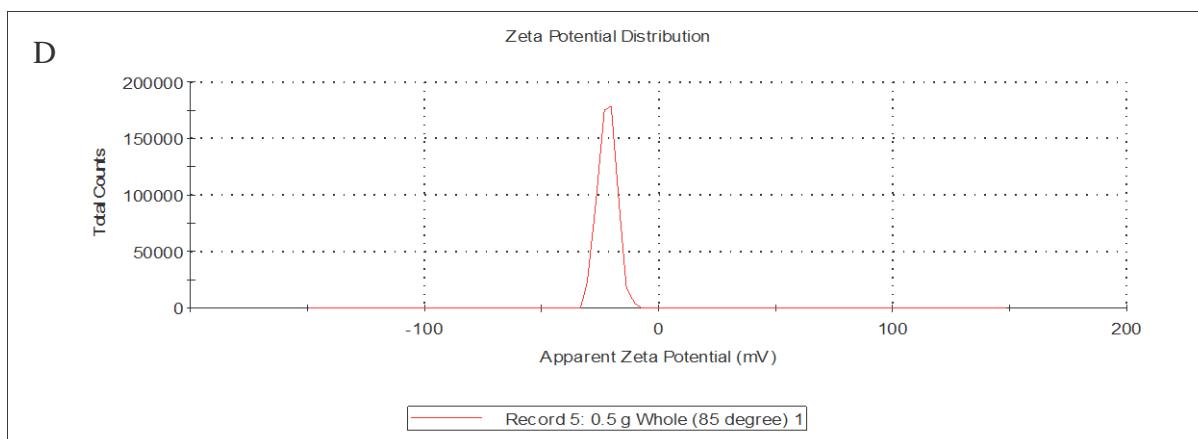
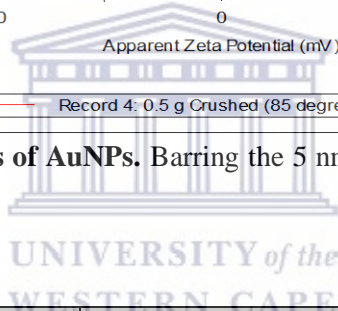


**Figure 3.6: Zeta Potential analysis of AuNPs.** Barring the 5 nm AuNPs, all AuNPs were relatively stable and anionic.



Sample name	DLS	Zeta Potential	Polydispersity Index (PDI)
5 nm AuNP	176.4 d.nm	-44.1 mV	0.402
10 nm AuNP	33.47 d.nm	-32.8 mV	0.225
50 nm AuNP	65.64 d.nm	-35.1 mV	0.102
Car-AuNP whole	176.1 d.nm	-23.3 mV	0.440
Car-AuNP crushed	191.4 d.nm	-19.9 mV	0.242

**Table 3.1: DLS and Zeta Potential results.** These results correspond to the size distribution curves (averaged) and zeta potential graphs depicted above.

A clear discrepancy in size of the 5 nm can be seen with a high PDI of 0.402 (Table 3.1). The size distribution of the 10 and 50 nm are moderately disperse and yielded good result qualities. The charge of all AuNPs barring the 5 nm indicated stable nano-dispersions. The same discrepancy seen for the 5 nm AuNPs regarding size is noticeable for the Car-AuNPs which measured an average of 11 nm with TEM.

### 3.1.4. Transmission Electron Microscopy

TEM was performed in order to visually confirm the presence of AuNPs, to visualize the morphological characteristics of the Car-AuNPs and to determine the core size and elemental composition of the AuNPs.

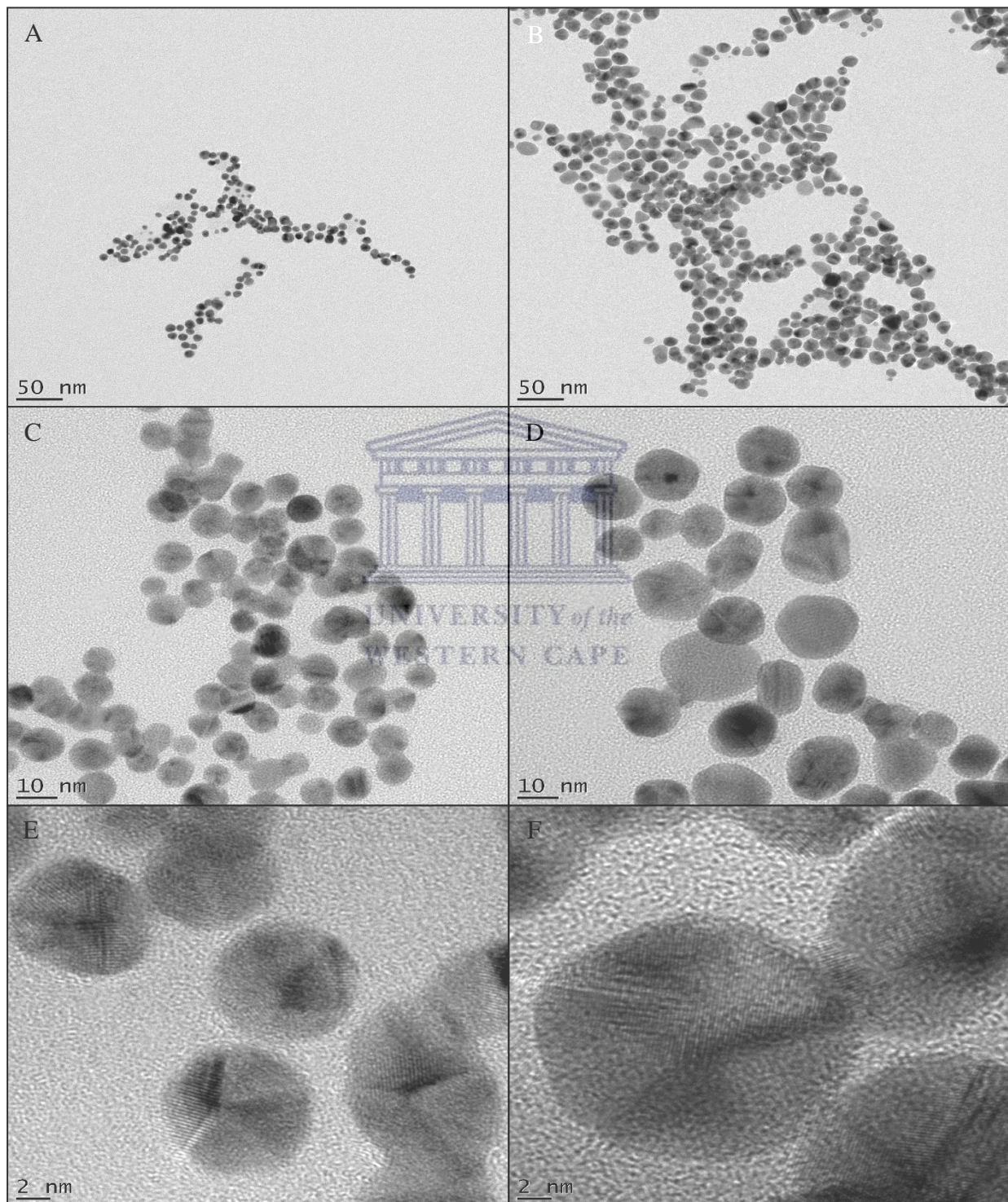


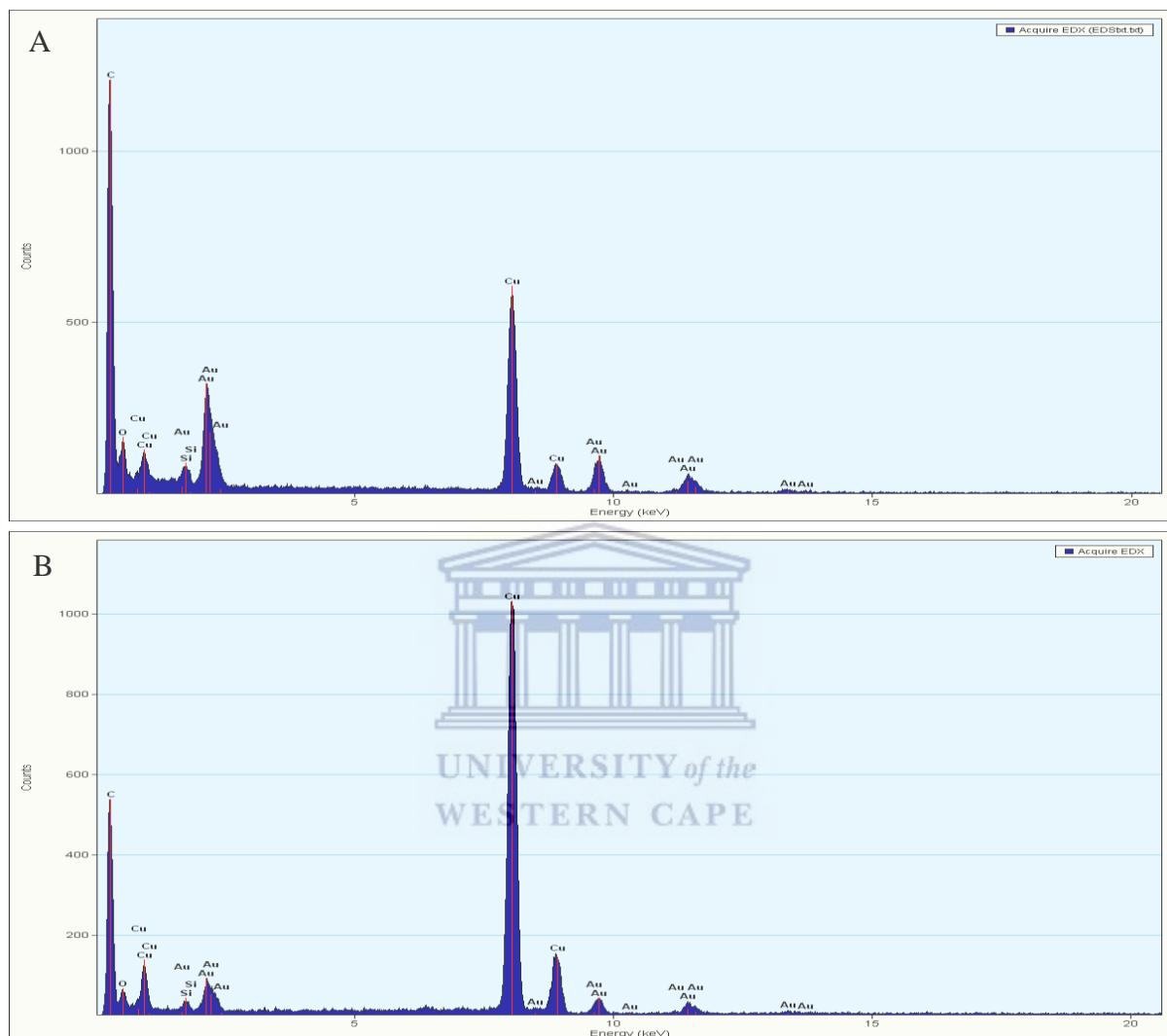
**Figure 3.7:** TEM images of Car-AuNPs synthesized at 85°C where images on the left (A, C and E) depict crushed cardamom pod seeds and images on the right (B, D and F) show AuNPs synthesized from whole cardamom pod seeds.

The images in Figure 3.7 reveal AuNPs that are largely similar in size with conformal shapes (spherical) in Car-AuNPs synthesized with crushed AuNPs whereas Car-AuNPs synthesized with whole cardamom seeds produced AuNPs of various shapes (spherical, rod shaped, triangular, and pentagonal) and sizes. The TEM images allow a visual confirmation of the NP shape and affirm results obtained and outlined in Table 3.1. The core sizes of the Whole-AuNPs were highly variable with measurements of 30 and 20 nm whereas the Crushed-AuNP measurements were within 10-12 nm size range (as measured by the technician).



### 3.1.5. Energy dispersive X-ray spectroscopy (EDS)

EDS was performed in addition to TEM in order to determine the elemental composition of the NPs and confirm that Au atoms are present within the sample. The graphs presented in Figure 3.8 confirm that there are Au atoms present within the sample.



### 3.1.6. Selected area diffraction (SAED)

SAED was the final confirmatory test used to identify the nature of AuNPs. Like EDS, it is performed in addition to TEM by changing the detector of the electron microscope.

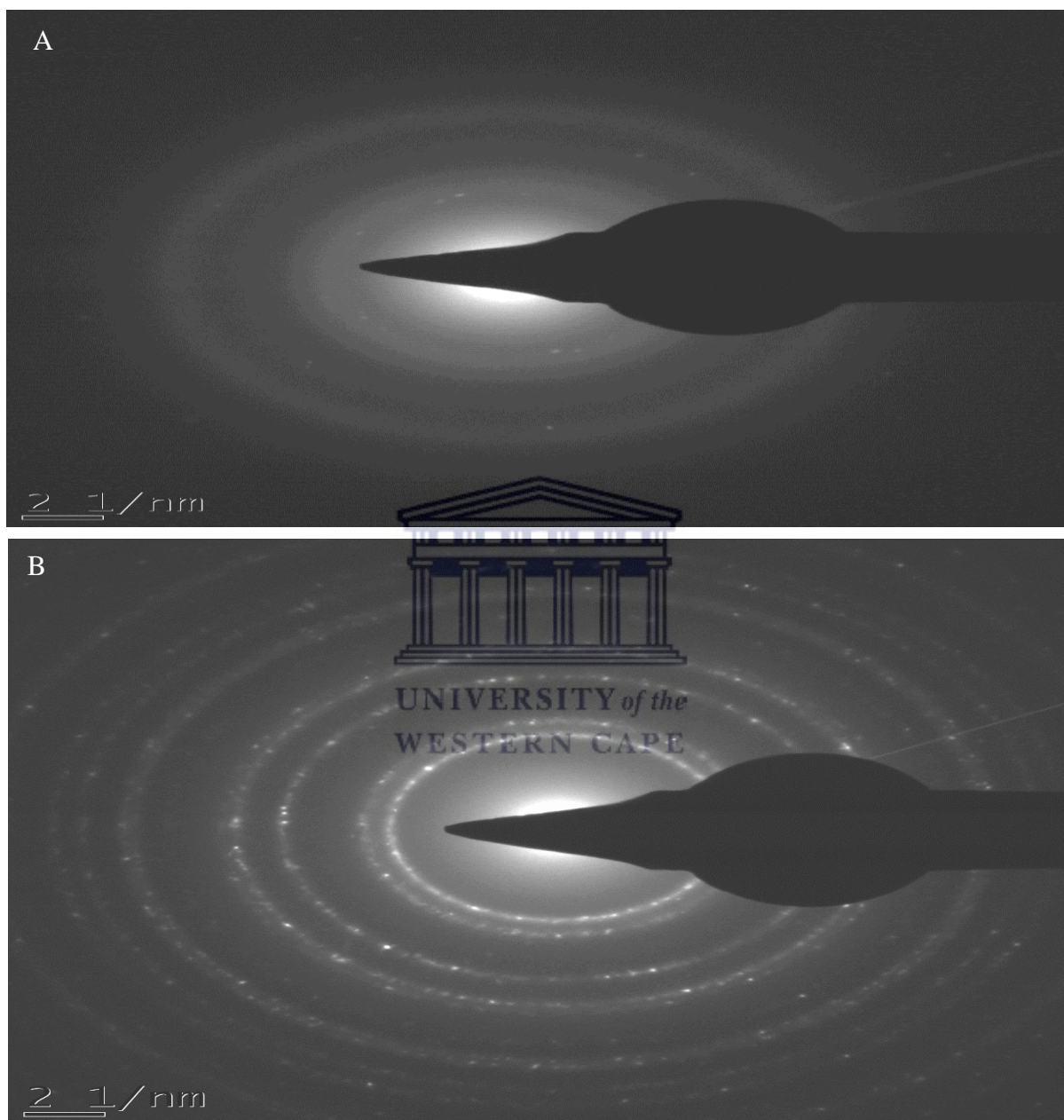


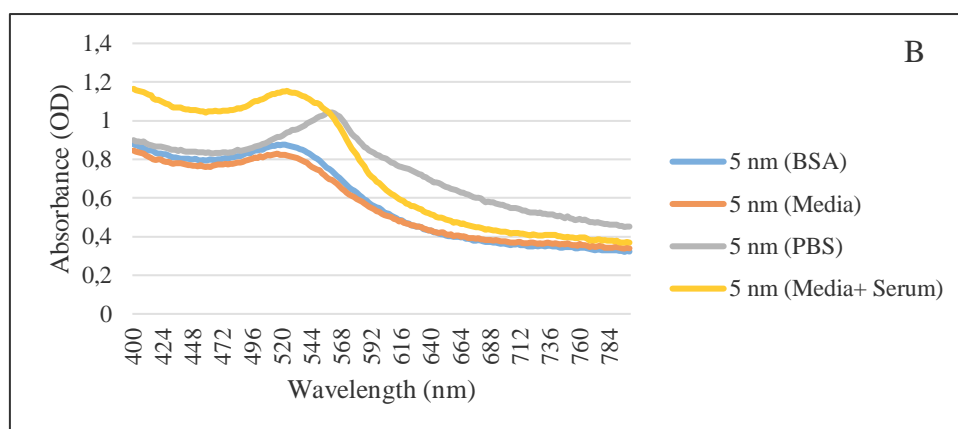
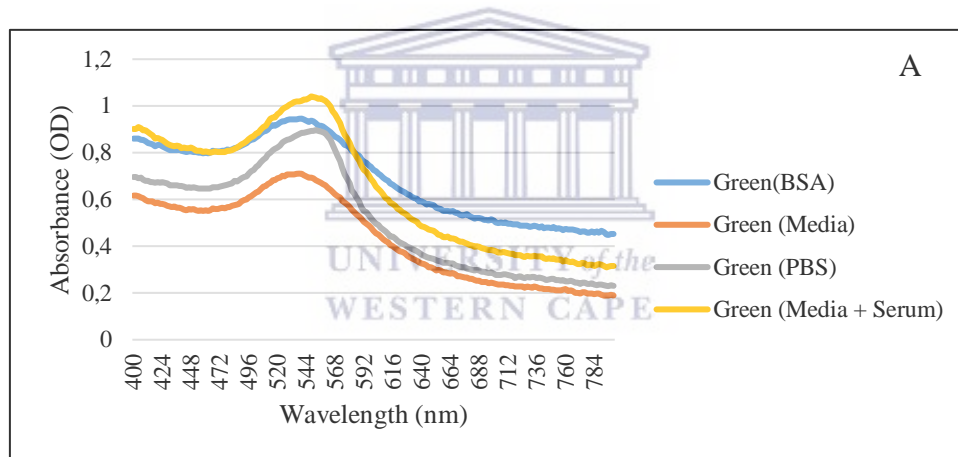
**Figure 3.9:** Images depicting SAED results of Car-AuNPs synthesized at 85°C using A) crushed cardamom seed pods and B) whole cardamom seed pods.

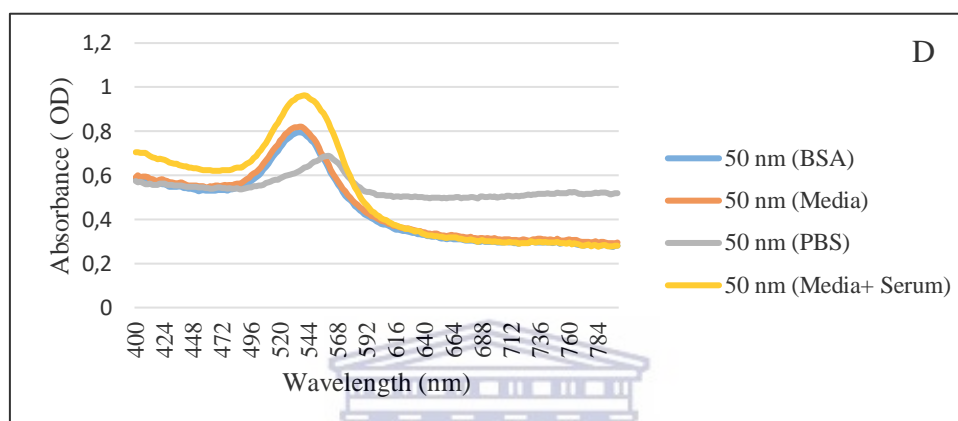
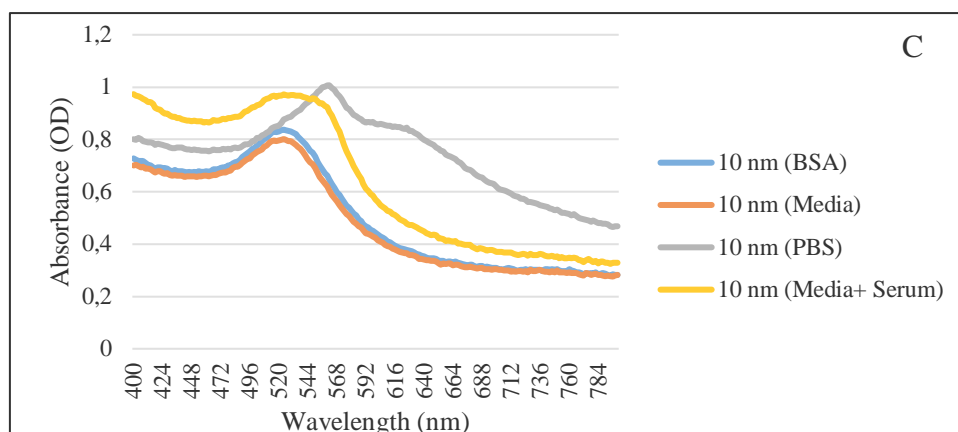
The elliptical rings containing bright spots are characteristics of crystalline AuNPs (Figure 3.9). It could thus be deduced that AuNPs are crystalline in nature with a probable face

centred cubic (fcc) unit cell structure that is characteristic of metallic crystalline structures (Page, et al., 2004).

### 3.1.7. Stability testing

Stability testing was performed in order to obtain the level of stability that AuNPs exhibit after exposure to cell culture media. AuNPs were incubated in commonly used buffers and cell culture media for 24 hours reflecting the longest incubation period of the AuNPs within cultures during experimental exposure scenarios. Each particle type was incubated in four different increasingly biologically complex media i) Phosphate Buffer (PBS) ii) Bovine Serum Albumin (a high molecular weight protein and major component of serum (5 mg/ml) iii) RPMI 1640 medium and iv) RPMI 1640 medium supplemented with 10 % FBS at 25°C and 37°C.

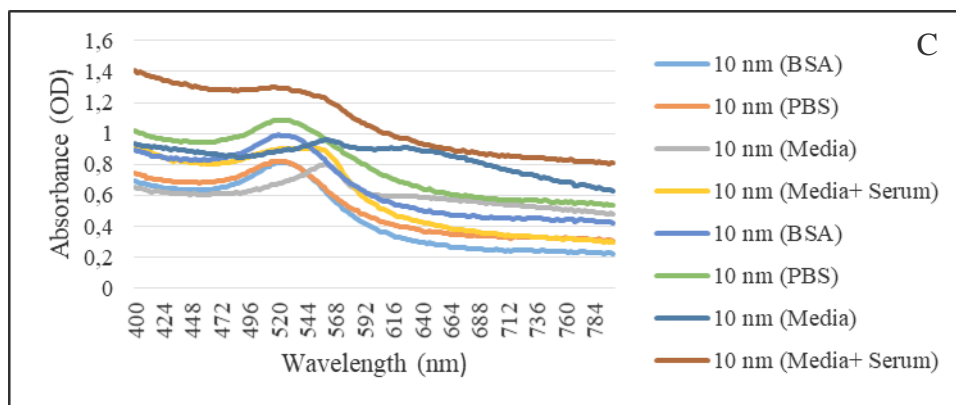
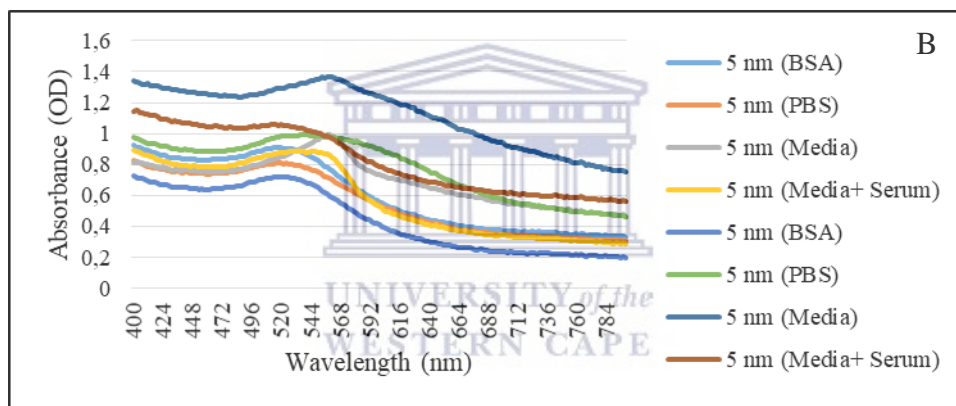
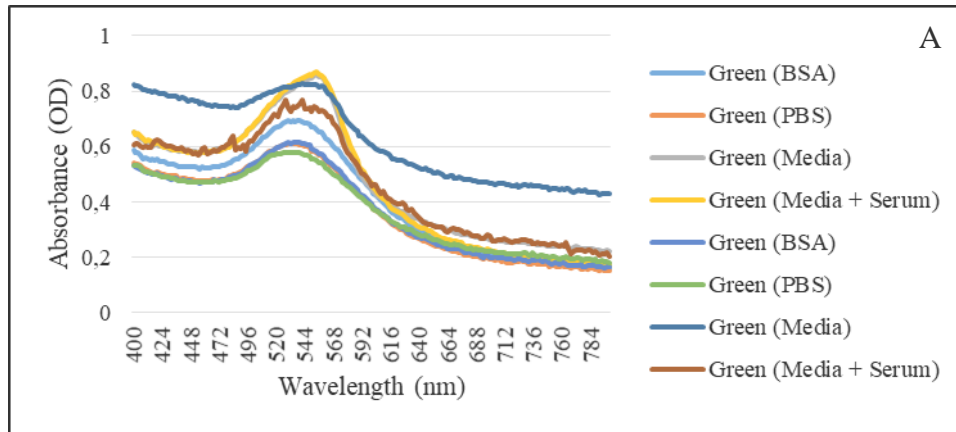




**Figure 3.10: Absorption profiles of AuNPs immediately after the addition of biological media to the respective AuNPs. A) represents Car-AuNPs B) 5 nm AuNPs C) 10 nm AuNPs and D) 10 nm AuNPs**

Compared to the normal spectra of the AuNPs seen in Figure 3.3 and Figure 3.4 agglomeration is present upon the addition of media. This agglomeration is apparent from the spectral shift seen from  $\lambda_{max}$ : 544 nm, to 535 nm (BSA), 530 nm (Media), 570 nm (PBS) and 540 nm (media and serum) for the 5 nm AuNPs. Though decreases in  $\lambda_{max}$  values occurred, the increase in the SPR band width occurred and could be used as confirmation of AuNP agglomeration within culture media. 10 nm AuNPs wavelengths shifted from 542 nm to 525 nm (BSA), 520 nm (PBS), 582 nm and 540 nm (media and serum). Spectral shifts were also evident for 50 nm AuNPs with spectral curves seen from 536 nm to 544 nm (BSA), 544 nm (media), 554 nm (PBS) and 552 (media and serum). Spectral shifts in the UV-spectrum of Car-AuNPs was also visible with the recorded  $\lambda_{max}$  increasing from 525 nm to 544 nm (BSA), 536 (Media), 566 (PBS), and 550 nm (media and serum). The addition of BSA or media to the AuNP solutions resulted in negligible agglomeration within some samples whilst other AuNP solutions remained unaffected by the addition of the biological

media (50 nm). The greatest level of agglomeration across all samples was caused by the addition of PBS, whilst increased levels of agglomeration are indicated by the major shifts of AuNP spectra when compared to the effects of the other biological media.



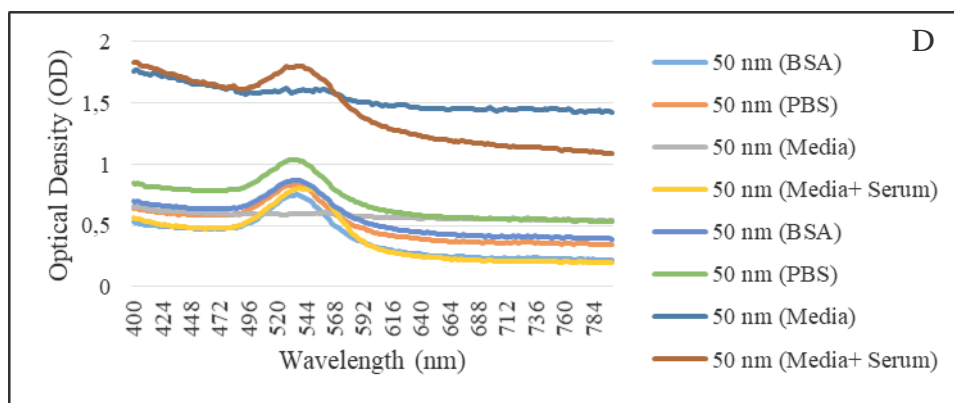


**Figure 3.11: The Absorption spectra of AuNP solutions after a 24 hour incubation period with biological media.** 24 hour spectral curves depict 25 °C incubation (top half of legend) and 37 °C (bottom half of legend) incubation temperatures.

After 24 hours the 5 and 10 nm AuNPs exhibited similar levels of agglomeration at both temperatures (Figure 3.11 C and E) whilst the Car-AuNPs and 50 nm (Figure 3.11 A and D) AuNPs remained relatively stable. With the exception of Car-AuNPs, media, and supplemented media affected the spectral shifts the most. In all cases with upwards of 5 nm shifts in absorbed spectra for all samples along with SPR flattening when compared to absorbance profiles without biological media indicating AuNP agglomeration within the solutions. The AuNP agglomeration levels also increased when exposed to the 37 °C incubation temperatures as opposed to the 25 °C temperatures.

WESTERN CAPE

### 3.1.8. Gold Nanoparticle uptake (ICP-MS)

ICP-MS was used to quantify the uptake of AuNPs in CHO cells and to correlate the difference in uptake between the 10 nm and 50 nm AuNPs.

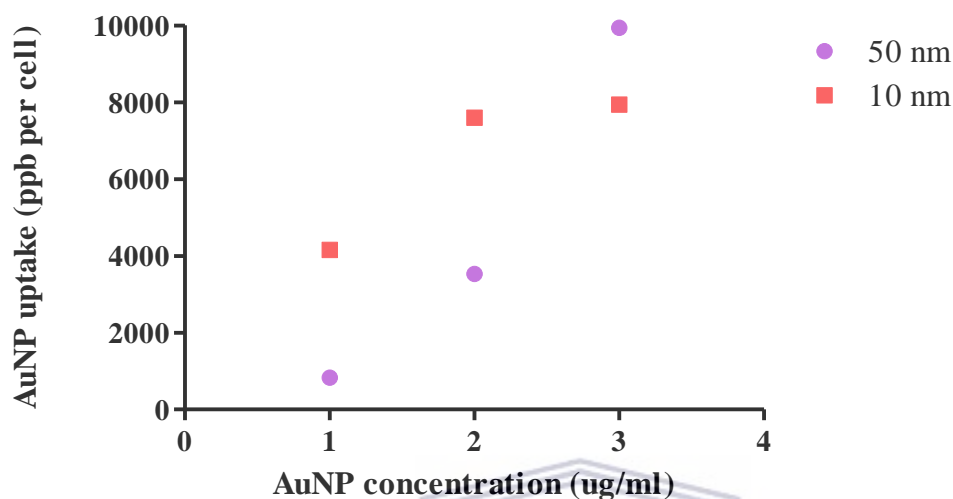


Figure 3.12: Quantities of AuNPs taken up by CHO cells after a 24 hour incubation with 10 nm and 50 nm AuNPs. The decreased uptake of the 10 nm AuNPs at the highest concentration was treated as an outlier.

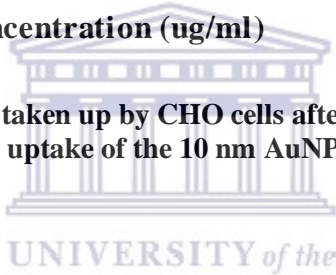


Table 3.2: Estimated quantities of AuNP uptake after a 24 hour incubation period with increasing concentrations of each AuNP type.

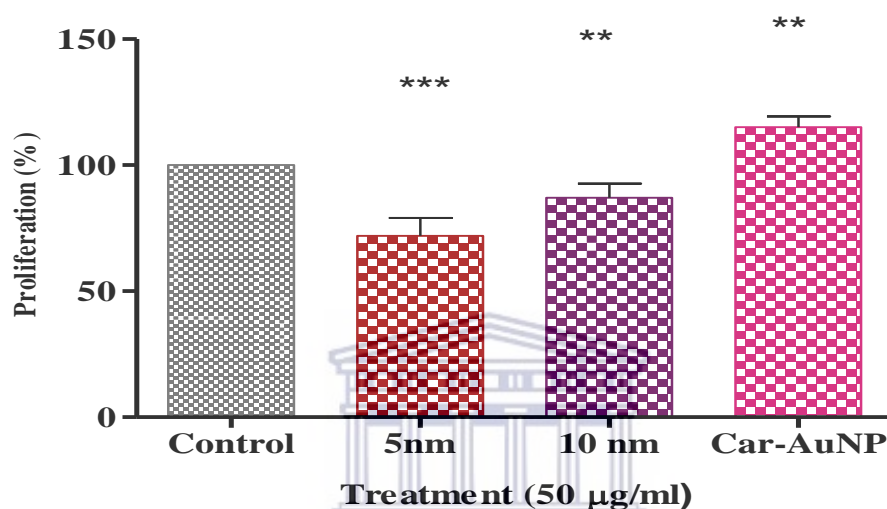
Key of concentration on graph	Applied concentration of 10 nm and 50 nm AuNPs	Approximated amount of 10 nm AuNPs endocytosed by cells	Approximated amount of 50 nm AuNPs endocytosed by cells
1	2.5 $\mu\text{g/ml}$	2.3 $\mu\text{g/ml}$	1.8 $\mu\text{g/ml}$
2	5 $\mu\text{g/ml}$	4.5 $\mu\text{g/ml}$	3.6 $\mu\text{g/ml}$
3	10 $\mu\text{g/ml}$	8.4 $\mu\text{g/ml}$	7.3 $\mu\text{g/ml}$

Figure 3.12 illustrates an increase in uptake efficiency in response to an increase in AuNP concentration. The 10 nm AuNPs are taken up more efficiently than the 50 nm AuNPs as can be seen in Table 3.2. This higher uptake of 10 nm AuNPs in CHO cells is also clear in Figure 3.12, where there is an increased uptake of 10 nm AuNPs (red square) when compared to 50 nm AuNPs (purple dots) up to an AuNP concentration of 10  $\mu\text{g/ml}$ .

## 3.2 *In vitro* analysis

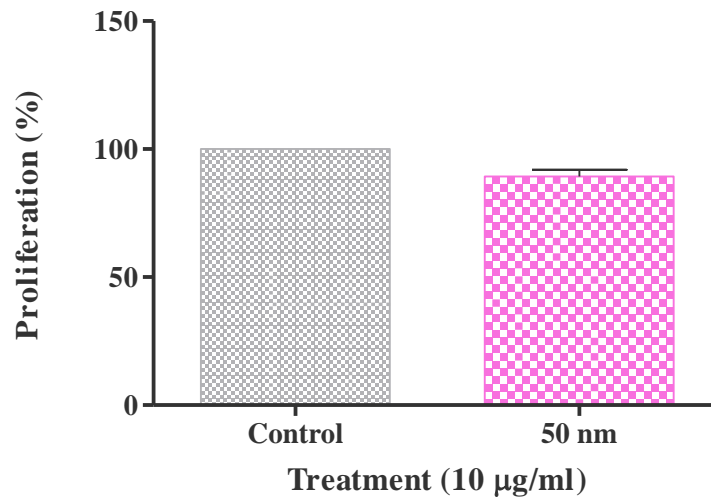
### 3.2.1 Cell Proliferation

The effect AuNPs on cell proliferation was investigated, using a crystal violet assay prior to irradiation experiments. The time frames of 4h (Figure 3.13 and 3.14) and 24 h (Figure 3.15) were used for these experiments, since they reflect the pre-incubation periods that were used to expose the CHO cells to AuNPs before proton radiation.



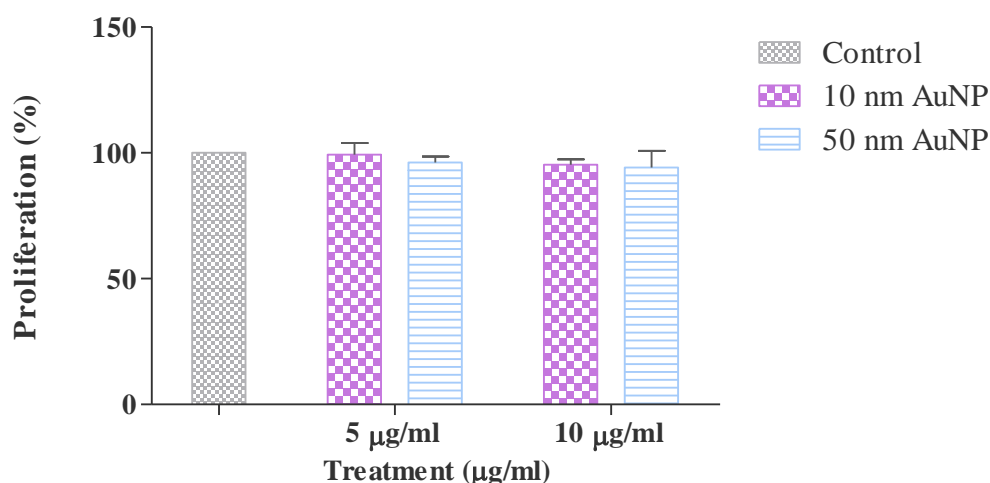
**Figure 3.13: Effect of AuNPs on cell proliferation after 4 h incubation period.** Bars labelled \*\*\* and \*\* depicts mean values that were significantly different from controls. \*\*\* (P<0.001) \*\* (P<0.01).

Figure 3.13 shows that the greatest level of cytotoxicity was exhibited by the 5 nm AuNPs, wherein 28 % reduction in cell proliferation was caused, whilst the 10 nm AuNPs reduced the cell proliferation by 13 % when compared to controls. The Car-AuNPs had an opposite, stimulatory effect on the cell proliferation of CHO cells increasing the cell proliferation from 100 % expressed by controls to 115% in Car-AuNP treated samples.



**Figure 3.14: Effect of 50 nm AuNPs on cell proliferation after 4 hour incubation period.** 50 nm AuNPs had a slight effect on cell proliferation after a 4 hour exposure period. Mean did not differ statistically significantly ( $p>0.05$ )

The 50 nm AuNPs caused minimal decreases in cell proliferation after 4 hours (Figure 3.14) resulting in a ~10 % decrease in cell population when compared to controls. One must note that a lower concentration of 50 nm AuNPs was used for the cell proliferation experiments compared to the 50µg/ml concentration used for the 4 h incubation experiments with the commercial 5 nm and 10 nm AuNPs and the Car-AuNPs (see Figure 3.13). This was done to limit the volume of 50 nm stock solution that had to be added to the cell culture as previously described in section 2.5.2.1 Cell proliferation.



**Figure 3.15: Effect of larger AuNPs (10 nm and 50 nm) at low concentrations on cell proliferation after a 24 hour incubation period.** The AuNPs exhibited very little to no effect on the proliferation of the cells when compared to their controls Means were not significantly different from control ( $P>0.05$ ).

The 10 nm AuNPs had no effect on cell proliferation at lower concentrations (5  $\mu\text{g/ml}$ ) whilst at higher concentrations (10  $\mu\text{g/ml}$ ) cell proliferation was minimally decreased by 5% (Figure 3.15). The 50 nm AuNPs reduced the cell proliferation by 4% (at 5  $\mu\text{g/ml}$ ) and 6% (10  $\mu\text{g/ml}$ ) respectively.



### 3.2.2 Cell Viability

In order to determine whether or not 1.8 cineole affected cell viability, the MTT assay was selected. Due to 1.8 cineole being a compound, spectral overlap did not have to be considered in this assay selection as was the case with AuNPs. The MTT assay could be performed in lieu of the crystal violet assay which allows rapid detection on the same day and requires less preparation but yields result outcomes that are as reliable and reproducible as the latter. 1.8 cineole is the active compound of cardamom. Accordingly, it was imperative to determine the optimal inhibitory concentration of 1.8 cineole in order to allow the correlation between 1.8 cineole and Car-AuNPs and deduce whether or not they would induce similar effects in the same experimental conditions.

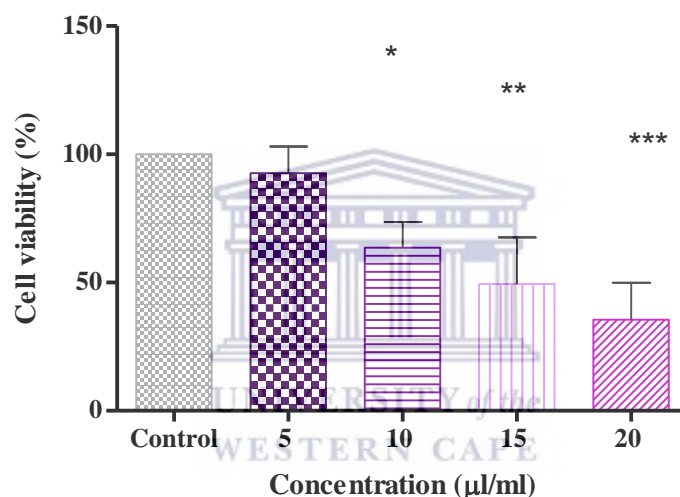


**Figure 3.16: The effect of different 1.8 cineole concentrations on cell viability.** \* indicates P value <0.05, \*\* indicates P value < 0.01 and \*\*\* indicates P value <0.001.

1.8 cineole inhibited cell viability in a dose dependent manner (Figure 3.16) in which the 20 µl/ml concentration caused the greatest level of inhibition of cell viability. In all cases the means were statistically different from the control except for the 5 µl/ml concentration of the 1.8 cineole. Conversely the 20 µl/ml of the 1.8 cineole showed highly significant levels of inhibition reducing cell viability by more than 50%.

### 3.2.3 Mitotic Index

Mitotic index was quantified in order to determine the effects of 1.8 cineole and the AuNPs on the mitosis of CHO cells. Additionally, the assay was performed in order to determine whether the compound and AuNPs would induce similar effects when applied under the same experimental conditions.

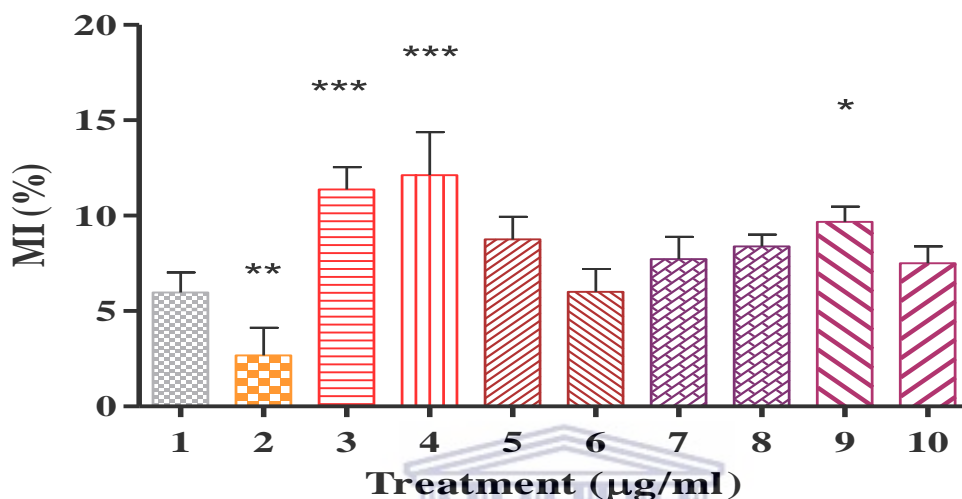


**Figure 3.17: The effect of 1.8 cineole and AuNPs on mitotic index.** 1) Control 2) 1.8 cineole (20 µl/ml) 3) Car-AuNPs (5 µg/ml) 4) Car-AuNPs (10 µg/ml) 5) 5 nm AuNPs (5µg/ml) 6) 5 nm AuNPs (10µg/ml) 7) 10 nm AuNPs (5 µg/ml) 8) 10 nm AuNPs (10 µg/ml) 9) 50 nm AuNPs (5µg/ml) 10) 50 nm AuNPs (10 µg/ml)

Quantification of the effects of 1.8 cineole and AuNPs on mitosis is shown in Figure 3.17. The study showed that 1.8 cineole had an inhibitory effect on the MI of the cells after 24 h. The 5 µg/ml and 10 µg/ml Car-AuNPs stimulated mitosis (11 and 12% respectively). Both concentrations of 10 nm AuNPs stimulated the CHO cells to the same extent (8 and 9%) whereas 5 µg/ml of 50 nm AuNPs stimulated mitosis (10%) whilst 10 µg/ml 50 nm AuNPs induced a ~78% stimulation in mitosis. 5 µg/ml 5 nm AuNPs stimulated mitosis up to ~9% when compared to the 6 % of controls whereas the addition of 10 µg/ml of 5 nm AuNPs to cells had no effect on the MI of CHO cells. Both concentrations of Car-AuNPs applied to cells showed statistically significant ( $P < 0.001$ ) differences when compared to controls whilst statistically significant ( $P < 0.05$ ) were seen in cells exposed to 5 µg/ml of 50 nm AuNPs when compared to controls. The active compound of cardamom (1.8 cineole) statistically significantly reduced mitosis ( $P < 0.01$ ) after 24 hours. The effects of 5 nm and 10 nm at

different concentrations were not statistically significant from those of the control and did not influence mitosis of the CHO cells.



### 3.3. Proton experiments

#### 3.3.1 Cell Survival

The cellular radiosensitivity expressed as surviving fraction at 6 Gy was determined by the cell survival clonogenic assay. Cell survival data for the CHO cells are shown in Fig 3.18.

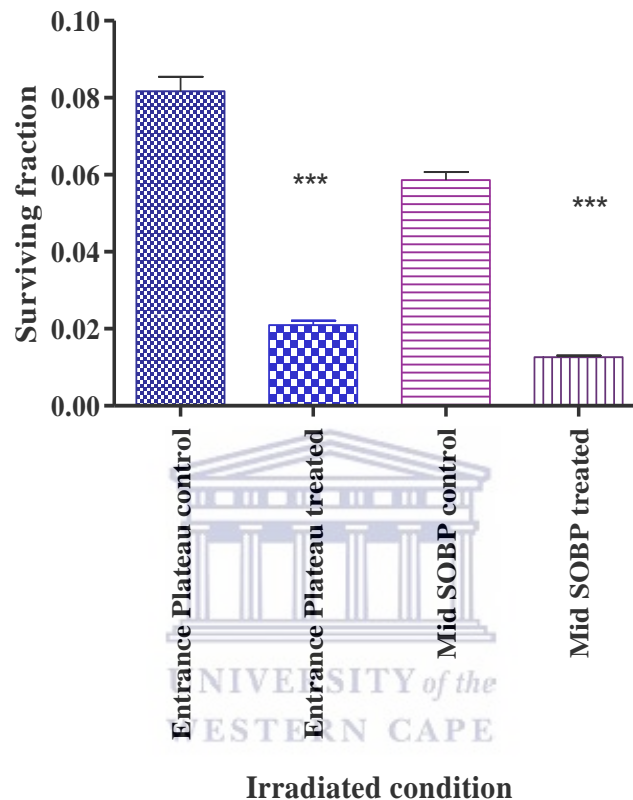


**Figure 3.18:** Surviving fractions of cells after the concurrent treatment of 6Gy protons in the entrance plateau and the middle of the SOBP (control) and a combined treatment of 6 Gy protons with 50 nm AuNPs (37  $\mu$ M) at the same positions. Plating Efficiency (PE) of 0.82 for CHO cells treated with AuNPs without radiation was taken into account.

A visible reduction in the surviving fractions of cells can be seen when comparing the surviving fraction of CHO cells irradiated in the middle of the SOBP position compared to cells irradiated at the entrance plateau position in Figure 3.18. The addition of AuNPs to proton irradiation resulted in an even greater decrease in the surviving fractions of the cell populations in both positions compared to controls that were not treated with 50 nm AuNPs ( $p < 0.001$ ). These results show a clear dose enhancement effect of 50 nm AuNPs in CHO cells irradiated with 200 MeV protons.

### 3.3.2 Chromosomal Damage

Chromosomal damage in CHO cells treated with AuNPs and irradiated with protons was determined by using the micronucleus assay. Micronuclei provide a convenient and reliable index of both chromosome breakage and loss due to radiation damage. The CBMN assay was carried out in samples with the addition of Cyt-B leading to BN cell formation (see Figure 3.19). The assay allows better precision analysis because the results cannot be confounded by cell division kinetics.

For the CBMN experiments, CHO cells were exposed to 50  $\mu\text{g/ml}$  of 5 nm AuNPs, 10 nm AuNPs and Car-AuNPs for 4 hours prior to irradiation with a 2 Gy dose of protons. For the experiments with 50 nm AuNPs cells were exposed to 10  $\mu\text{g/ml}$  (37  $\mu\text{M}$ ) of 50 nm AuNPs for 4 and 24 hours prior to proton irradiation with 2 or 4 Gy doses. A low background number of MNi was observed in the control samples that were treated with different AuNP types (~12 MNi/500 BN cells) and not irradiated with protons. However, a noticeable increase in MNi could be seen when cells were exposed to protons, AuNPs with protons and with increasing proton dose (4 Gy).

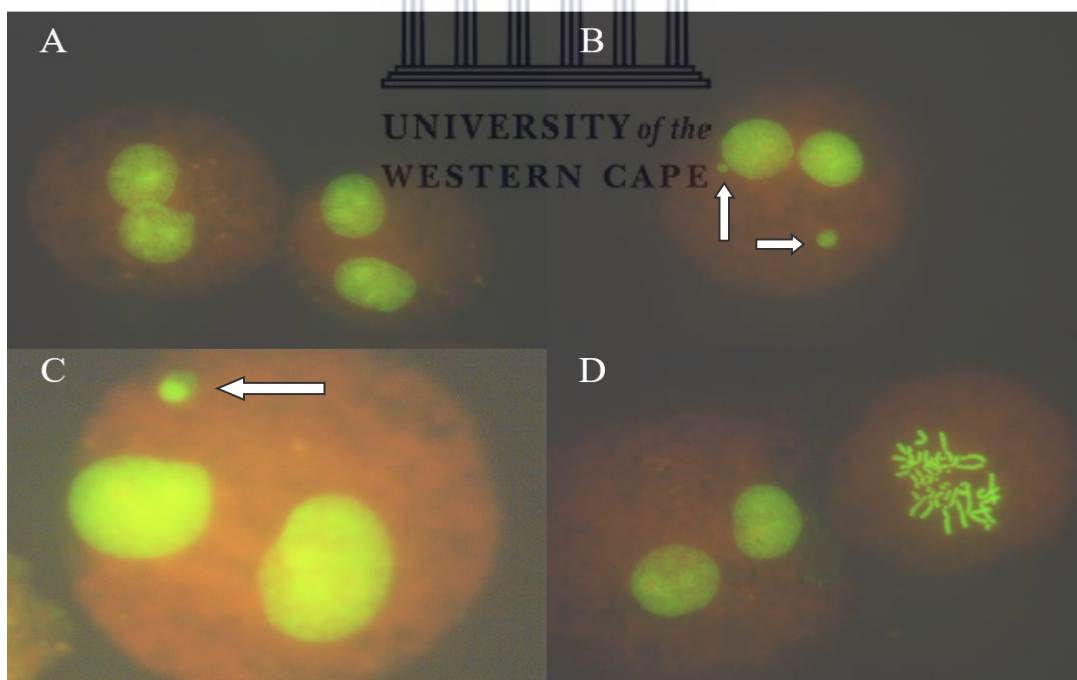


**Figure 3.19** Images of BN cells containing A) no MNi B) two MNi C) one MNi and D) BN cell containing no MNi and a mononucleated cell in prometaphase of mitosis.

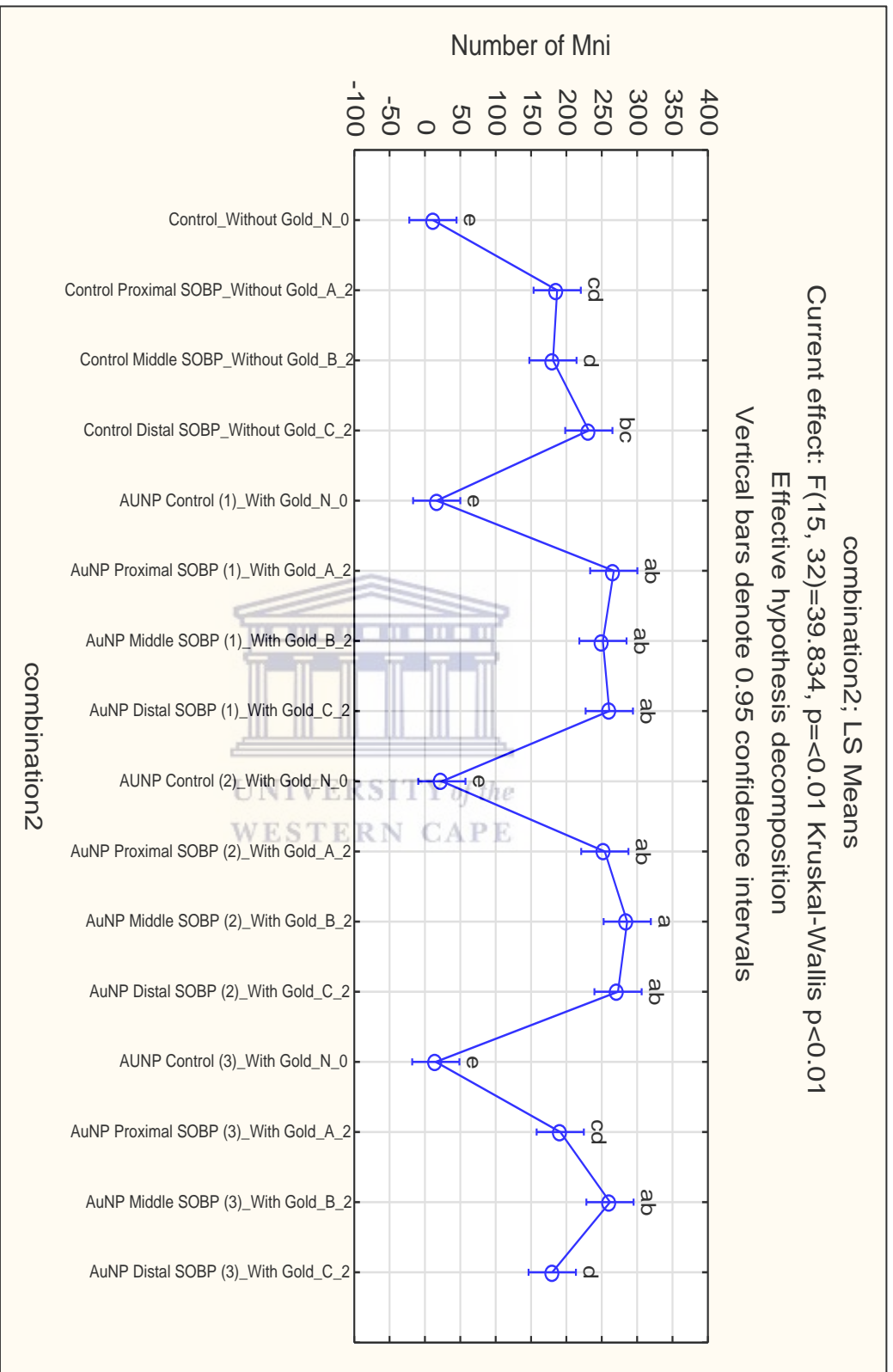


**Figure 3.20: MNI frequencies measured for protons with 5 and 10 nm AuNPs after a 4 hour incubation period.** 1) Represents 5 nm AuNP 2) 10 nm AuNP and 3) Car-AuNP exposures with a concentration of 50 µg/ml. MNI/500 BN cells was scored of 3 replicates per sample. Samples labelled **a** and **ab** or **bcd** and **abc** were significantly different statistically indicated by the difference in alphabetic letters and letter arrangements.

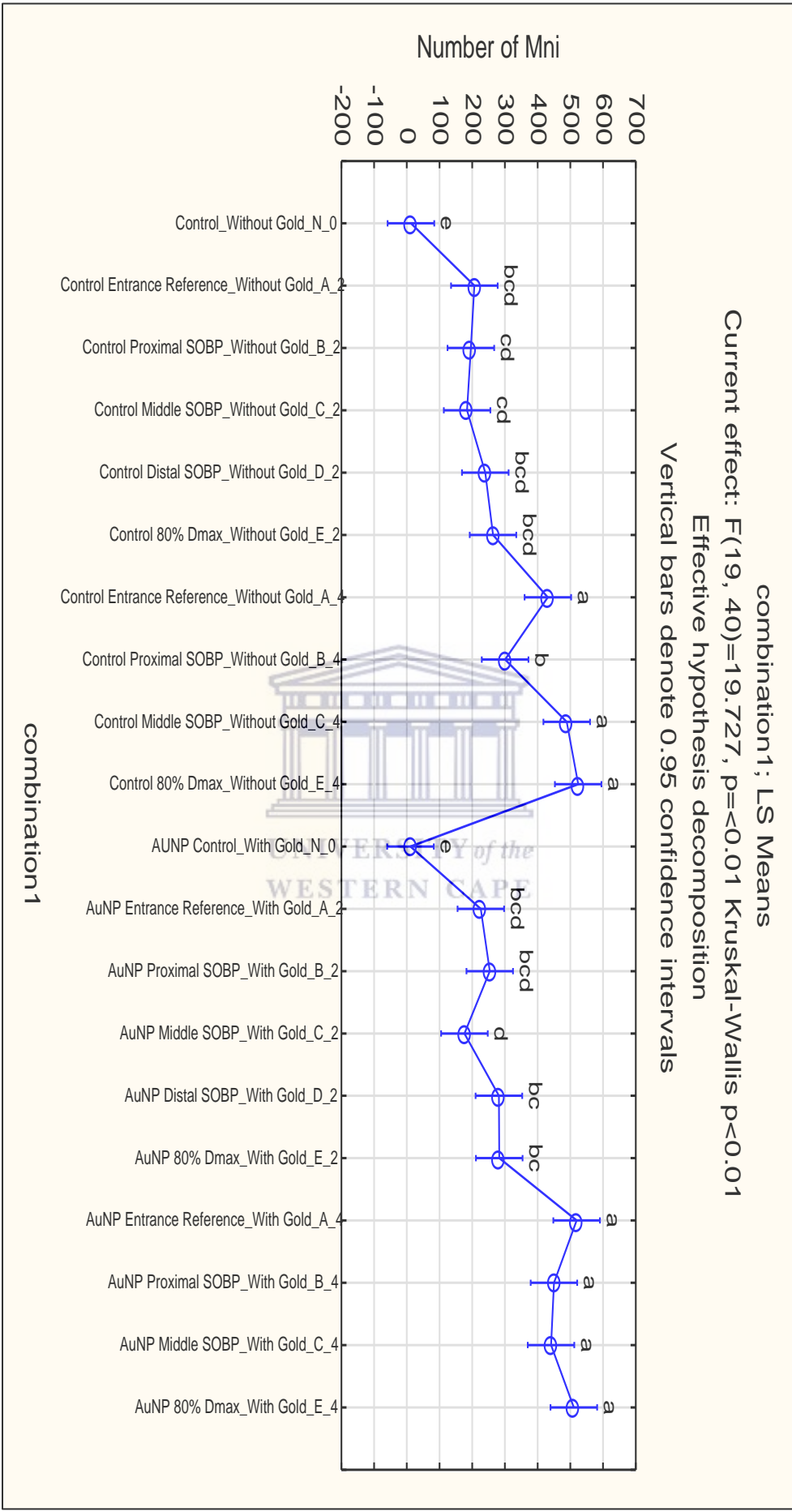
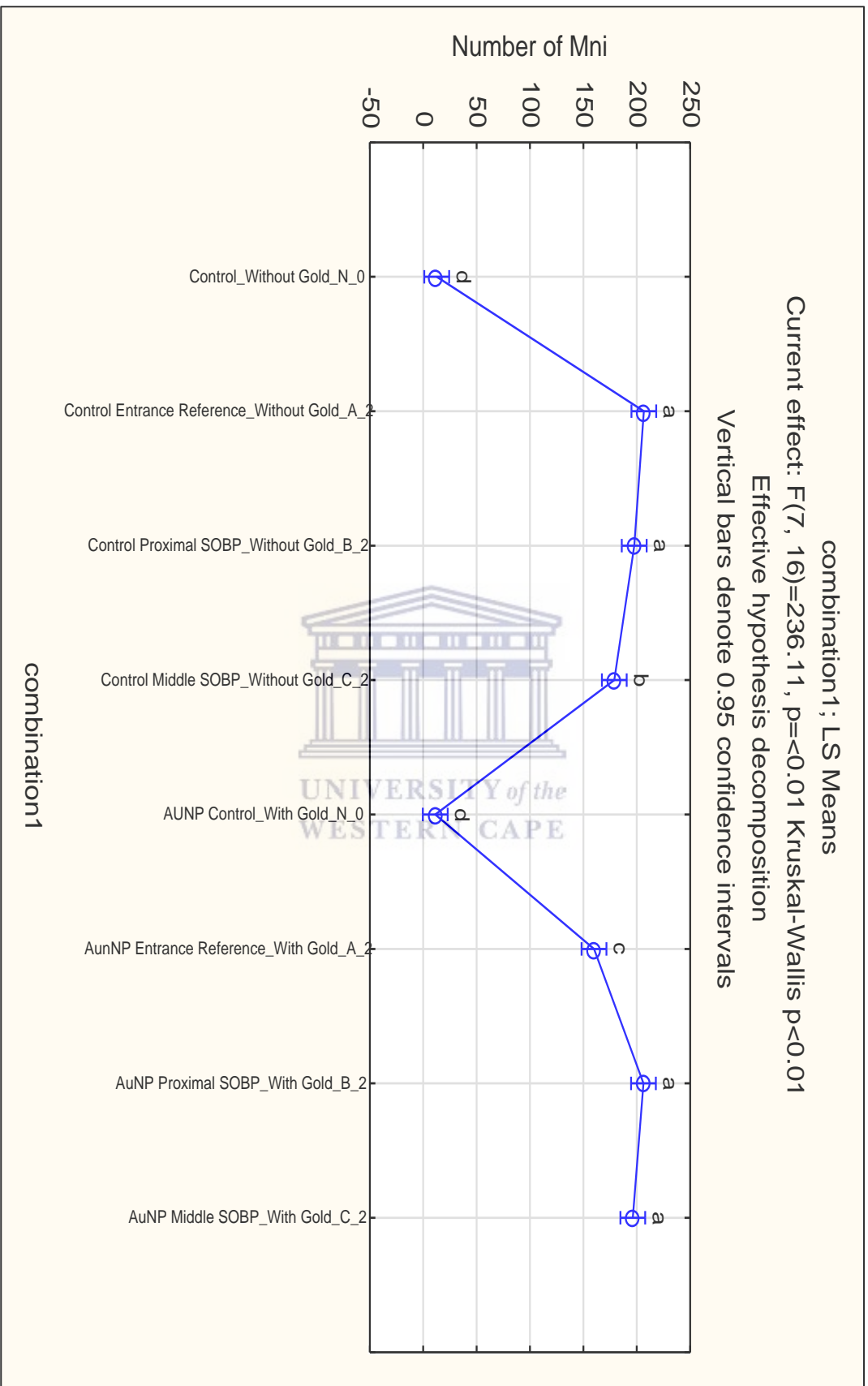


Figure 3.21: Frequency of MNi measured after exposure with 2 and 4 Gy protons and 10 µg/ml (3 7µM) of 50 nm AuNPs after 4 hours. MNi were scored in triplicate for each sample per 500 BN cells respectively.



**Figure 3.22 MNI frequency after exposure with 10 µg/ml of 50 nm AuNPs at a concentration for 24 hours and subsequent administration of protons. 3 replicates of each sample were prepared and MNI scored per 500 BNs.**

Figure 3.20 illustrates the number of MNi/500 BN cells after a 4 h incubation with 50µg/ml of 5 nm, 10 nm and Car-AuNPs followed by 2 Gy proton irradiation. The cells were irradiated at 3 different positions in the SOBP (see Figure 2.2). Statistically significant differences were seen in all cases comparing the MNi yield of samples exposed to AuNPs and protons compared to the MNi yields of samples exposed to protons alone ( $P < 0.01$ ). The 5 nm and 10 nm AuNPs with protons showed significantly higher MNi yields when compared to irradiated controls at the same positions (proximal and middle positions of the SOBP). Car-AuNPs increased the number of MNi in the middle of the SOBP only ( $P < 0.01$ ). The MNi yields for CHO treated cells with 10 nm AuNPs and 2 Gy protons was 254 MNi/500 BN cells ( $P < 0.05$ ), 284 MNi/500 BN ( $P < 0.01$ ) and 273 MNi/500 BN cells compared to 187 MNi/500 BN cells, 181 MNi/500 BN cells and 231 MNi/500 BN cells for CHO cells treated with protons alone at the proximal, middle and distal positions of the SOBP respectively. Car-AuNPs influenced MNi expression minimally in the proximal and distal SOBP positions.

Exposure of cells to 50 nm AuNPs for 4h and 2 Gy proton irradiation did not result in a pronounced dose enhancement effect (Figure 3.21). However, the incremental increase in MNi expressed with increasing depth along the SOBP was not clear in samples treated with 50 nm AuNPs exposed to 2 Gy doses of proton radiation. A radiosensitization effect was observed in cells exposed to the combination of 4 Gy protons and AuNPs compared to its irradiated controls, but this was less clear for the middle of the SOBP position. From Figure 3.21, it is suggested that a dose enhancement effect occurred in the entrance plateau with an increase of 431 MNi/500 BN to 519/500 BN cells and an increase from 300 MNi/500 BN cells to 450 MNi/500 at the proximal SOBP position. This effect disappeared with increasing depth.

After treatment of CHO cells with 10 µg/ml of 50 nm AuNPs for 24 h a, decrease in MNi frequency was seen with the presence of 50 nm AuNPs and 2 Gy protons (160 MNi/500 BN cells) in the entrance plateau when compared to irradiated control values (207 MNi/500 BN cells). Whilst a significant increase MNi frequency is reflected in cells containing AuNPs irradiated in the middle of the SOBP when compared to controls.

### 3.3.3. Cell cycle kinetics

Propidium iodide (PI) staining detected by flow cytometry was utilized to investigate the effects of proton radiation with and without AuNPs on cell cycle progression. Figure 3.23 depicts the most pronounced effects on cell cycle kinetics caused by specific AuNPs alone and AuNPs with a 6 Gy dose of protons. All exposure scenarios can be found within the addendum.

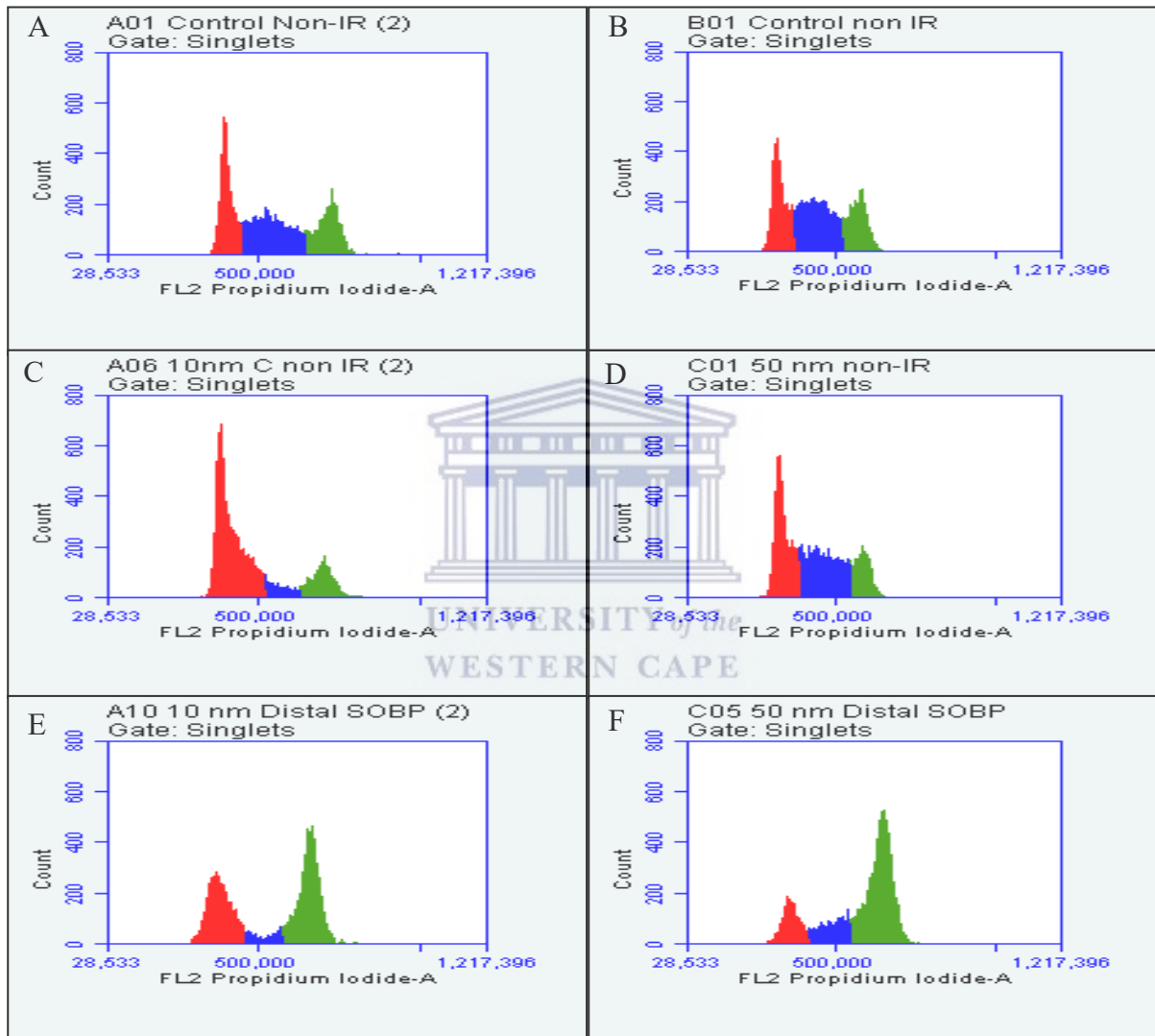


**Figure 3.23: The effect of 10 nm (50 µg/ml) and 50 nm (10 µg/ml) AuNPs and a 6 Gy dose of protons on cell cycle progression (A and B) depict negative controls for each condition, C) and D) show corresponding AuNP treated controls and E) and F) show the combined effect of AuNPs and 6 Gy protons.**

Both the 10 and 50 nm AUNPs depicted in figure 3.23 showed pronounced radiosensitization effects in the distal positions of the SOBP. Additionally both AuNPs induced a G0/G1 accumulation (increasing from 33.94% to 71.70% in the presence of 10 nm AuNPs and from 33.27% to 42.26% in the presence of 50 nm AuNPs when compared to controls) without irradiation.

Cell populations shifted towards G<sub>2</sub>M in an incremental manner with increasing depth along the SOBP when concurrently administered with protons as shown within the tables that follow.

**Table 3.3: The effect of Car-AuNPs and protons on cell cycle progression**

CONDITION	SOBP POSITION	G0/G1	S	G2/M
<b>Non-Irradiated Control</b>	N/A	33.27%	40.88%	25.49%
<b>Car-AuNP Treated, Non-IR</b>	N/A	42.26%	39.39%	18.03%
<b>Control IR</b>	Entrance Plateau	38.26%	16.63%	41.86%
<b>Car-AuNP treated, IR</b>	Entrance Plateau	49.95%	16.96%	32.20%

Car-AuNPs caused a 9% increase in the G0/G1 population and caused a 7% decrease in the G2/M population as shown in Table 3.3. The S phase cells remained unchanged. A similar effect is visible when assessing the irradiated conditions in the presence of AuNPs.

**Table 3.4: The effect of 5 nm AuNPs and protons on cell cycle progression**

Condition	SOBP POSITION	G0/G1	S	G2/M
<b>Non-IR Control</b>	N/A	55.22%	9.17%	31.92%
<b>5 nm-AuNP Treated, Non-IR</b>	N/A	48.96%	11.83%	37.27%
<b>Irradiated Control</b>	Entrance Plateau	26.18%	20.66%	45.08%
	Proximal	23.74%	19.70%	45.16%
	Middle	22.03%	20.54%	48.03%
	Distal	22.20%	21.58%	45.94%
<b>5 nm-AuNP Treated, Irradiated</b>	Entrance Plateau	23.04%	20.09%	48.06%
	Proximal	22.51%	17.89%	49.15%
	Middle	24.59%	17.79%	47.18%
	Distal	21.03%	21.52%	48.78%

5 nm AuNPs on their own influenced the cell cycle progression by causing an increase in G2/M population shown above in Table 3.4. In conjunction with 6Gy protons, minimal

influences on all phases of the cell cycle were observed when compared to the irradiated controls.

**Table 3.5: The effect of 10 nm AuNPs and protons on cell cycle progression**

Condition	SOBP Position	G0/G1	S	G2/M
<b>Non-Irradiated Control</b>	N/A	33.94%	37.63%	26.81%
<b>10 nm-AuNP treated, non-IR</b>	N/A	71.70%	8.12%	19.04%
<b>Irradiated Control</b>	Entrance Plateau	28.93%	11.48%	58.45%
	Proximal	28.54%	9.98%	60.29%
	Middle	28.48%	8.27%	61.25%
	Distal	13.66%	15.01%	68.98%
<b>10 nm-AuNP treated, Irradiated</b>	Entrance Plateau	37.72%	6.83%	54.30%
	Proximal	33.97%	10.00%	55.16%
	Middle	36.43%	9.19%	53.24%
	Distal	39.42%	7.33%	52.23%

10 nm AuNPs caused an increase the cell fraction in the G1-phase (Table 3.5). Cells in G1 increased from 33.94% to 71.70% seen in non-irradiated controls. When applied in combination with protons however, cells became more evenly distributed between G0/G1 and G2M and a large decrease in the fraction of cells in the S-phase could be seen across all conditions when compared to irradiated controls. Irradiated conditions compared to their internal reference control position revealed that the largest difference in cell phase populations is seen when comparing the distal position to the reference irradiated position. Additionally, the G2/M block induced at the irradiated control distal position is reduced by approximately 15% in the AuNP exposed condition whilst the G0/G1 increased by 25.76% and the S-phase population decreased.

**Table 3.6: The effect of 50 nm AuNPs on cell cycle progression.**

Condition	SOBP POSITION	G0/G1	S	G2/M
<b>Non-Irradiated Control</b>	N/A	33.27%	40.88%	25.49%
<b>50 nm-AuNP Treated, Non-IR</b>	N/A	42.26%	39.39%	18.03%
<b>Irradiated Control</b>	Entrance Plateau	44.78%	14.87%	39.47%
	Proximal	27.21%	28.86%	43.14%
	Middle	45.74%	15.87%	39.23%
	Distal	20.28%	18.29%	60.25%
<b>50 nm-AuNP Treated, Irradiated</b>	Entrance Plateau	34.20%	28.91%	36.33%
	Proximal	36.70%	28.74%	34.06%
	Middle	31.29%	30.09%	38.17%
	Distal	17.64%	16.35%	64.88%

An approximate 10% increase in the G0/G1 fraction can be seen in the presence of 50 nm AuNPs when compared to non-irradiated controls. This influenced the amount of cells in G<sub>2</sub>/M with a corresponding decrease of approximately 7%. Irradiation with protons, caused an incremental increase that correlates to depth in cell migration to G<sub>2</sub>/M in the controls. This resulted in decreases in G0/G1 populations sharing the most pronounced effect to be existed in the distal position of the SOBP with 60.25 % cells having migrated to G<sub>2</sub>/M. An anomalous decrease in the G<sub>2</sub>/M population is evident in G<sub>2</sub>/M population irradiated in the middle of the SOBP. The combination of protons and AuNPs revealed decreases in G0/G1 populations by approximately 10 % when compared to irradiated controls. This resulted in cell migrations into the S and G<sub>2</sub>/M phases resulting in slight increases in their respective populations when compared to irradiated controls.

---

## CHAPTER 4: DISCUSSION

---

### 4.1 Introduction

Radiation therapy (RT) is central to cancer treatment. About fifty percent of cancer patients receive radiotherapy as part of their treatment. Despite rapid technological advances, studies have reported high incidences of treatment related morbidity and side effects including secondary cancers, cardiovascular complications and fertility issues (Newhauser & Zhang, 2015). It is thus imperative to explore other unconventional radiation therapy modalities that have the potential to improve radiotherapy outcomes along with the patient's quality of life during treatment. The advantage that proton therapy (PT) could bring in sparing normal healthy tissue is an important evolution in modern radiation oncology (Valdivieso, et al., 2012).

Along with the rapid advancement of nanotechnology in recent years, the potential value of AuNPs as novel radiosensitizers has been discovered (Su, et al., 2014). For this study, the aim of incorporating AuNPs into radiation therapy is to increase its therapeutic efficacy while limiting damage to the surrounding cells. More specifically, the incorporation of AuNPs with the radiation is to improve the differential effect between tumours and healthy tissue (Retif, et al., 2015).

The aim of this study was to explore the possible dose enhancement effect that AuNPs have on cells impacted with protons at clinically relevant energies (200 MeV beam of protons). Preliminary time and dose dependent effects of different sized AuNPs as well as AuNPs synthesized from cardamom that previously displayed radioprotective effects when exposed to X-rays, influenced the choice of AuNPs used in this study. Cells treated with different sized (5, 10 and 50 nm) AuNPs were irradiated as attached monolayers with 200 MeV protons at different depths along the SOBP in order to determine whether AuNPs could induce a depth-dependent radioenhancement effect in PT.

## 4.2 AuNP characterization

### 4.2.1 UV-vis Spectroscopy

UV-visible spectroscopy is widely used in the study of nanomaterials as a diagnostic of nanoparticle formation. UV-vis spectroscopy often provides a means of choice to gauge responses in analysis to changes applied to AuNP colloidal systems. It has been further suggested that the spectroscopic properties of nanoparticles can provide an indicator of their size distribution by fitting the position of their surface plasmon resonance (SPR). SPR occurs when AuNPs are excited by electromagnetic waves resulting in the support of coherent oscillations of conduction electrons at the surface of the AuNPs. Upon scattering, SPR coupled with these electromagnetic waves results in a depolarized speckle pattern whose fluctuations yield precise information on the AuNP size (Tanev, 2009).

#### 4.2.1.1 Car-AuNPs

Adjusting multiple parameters in the synthesis procedure of Car-AuNPs revealed that the combination of optimal extract preparation and temperature played the greatest role in ensuring the production of Car-AuNPs with moderate size distributions that were stable in suspension. Optimal synthesis occurred at higher temperatures (75-85 °C). A change in AuNP suspension colour and the production of a more purple hue as opposed to a ruby red colour indicated AuNP agglomeration at lower temperatures (see Fig 5.1 of Addendum). Conversely, the deep purple colour was replaced by ruby red with increasing temperatures in a rapid 11 minute reaction. The change in colour was reflected in the absorptive intensity of the AuNPs, producing AuNPs with smaller  $\lambda_{max}$ . The decrease in  $\lambda_{max}$  values indicates a decrease in AuNP size (Figure 3.2). Corresponding findings were presented by Mountrichas *et al.* It was revealed that higher temperatures speed up the reaction mechanics and that the produced nanoparticles were more uniform in size (Mounthricas, et al., 2014). Furthermore, an additional study by Tran *et al.*, revealed that increasing the synthesis temperature of AuNPs resulted in smaller AuNPs and consequently smaller SPR bands. This corresponds to the findings depicted in Figure 3.2. In addition, the authors showed that even though reactional temperature played a role in the outcome of the NPs, the parameter with the greatest influence on AuNP quality was the amount of reducing and capping agents (Tran, et al., 2016). This effect was also observed in this study wherein cardamom extract served as the reducing and capping agent.

The same change in colour was observed when the extract was prepared differently by changing the parameters of the synthesis procedure (Figure 3.1A) as displayed by the absorbance profiles produced for each sample (Figure 3.3). The absorbance profile of the Car-AuNPs synthesized with whole cardamom seeds had a much longer SPR band ( $\lambda_{\text{max}}$ : 534 nm) than the Car-AuNPs synthesized with extract prepared from crushed cardamom seeds ( $\lambda_{\text{max}}$ : 580 nm). The long SPR band exhibited, is a well-known sign of particle aggregation within solution and the accompanying purple colour of the solution allows visual affirmation of the agglomeration (Huang & El-Sayed, 2010). This difference in AuNP quality could suggest that extract quantity or, more specifically in this instance, the amount of phytochemicals present within the extract, directly affects NP size, shape and stability which in turn affects the quality of the NP. From the results depicted in Figure 3.1 A and Figure 3.3, it can be speculated that by crushing the cardamom seed a greater amount of biomolecules may have been freed into the extract solution resulting in a more efficient reduction of  $\text{HAuCl}_4$  and subsequent AuNP capping with phytochemicals. According to Sujitha and Kannan, 2013, at higher quantities of extract, nanoparticle synthesis is greatly favoured due to the availability of sufficient biomolecules that are responsible for capping and stabilizing AuNPs (Sujitha & Kannan, 2013). This finding is further supported by a study performed by Singh and Srivastava. Using an extract prepared from black cardamom, the authors varied the  $\text{HAuCl}_4$  to quantity of black tea extract applied in the synthesis procedures at ratios of 1:1, 1:05 and 1:01 respectively. A gradual increase in the size of the AuNPs occurred when the amounts of extract was decreased (Singh & Srivastava, 2015). The increased size directly correlated to an increase in SPR band width. A similar phenomenon was seen in AuNPs synthesized using *Phoenix dactylifera L.* leaf extract. Varying the volume between 200-400  $\mu\text{l}$  of extract, the authors observed a shift in the SPR from 544-538 respectively, citing an increase in the number of AuNPs formed due to an increase in extract volume as the reason for the greater level of absorbance intensity (Zayed & Eisa, 2014).

#### 4.2.1.2 Citrate stabilized AuNPs

The absorbance profiles of the 5, 10 and 50 nm AuNPs revealed  $\lambda_{\text{max}}$  values of 540, 542 and 536 nm respectively (Figure 3.4). According to the specifications by supplier Sigma Aldrich, the 5 nm and 10 nm AuNPs absorb at an optical density of 1 between wavelengths measuring 510-525 nm. The increase in SPR band widths seen, could be due to the AuNPs losing a proportion of stability over time, causing some agglomeration and a longer SPR band.

However, the AuNPs absorbed light within the characteristic wavelength of AuNPs and exhibited ruby red colours that varied in shade (Figure 1.1 B) due to AuNP size. Thus it could be deduced that the AuNPs were relatively stable and acceptable for *in vitro* use. The same statement could be made for the 50 nm AuNPs, however no agglomeration was evident and the absorbance of the 50 nm AuNPs was within the range outlined by Sigma Aldrich (535-539 nm) indicating appropriate levels of stability.

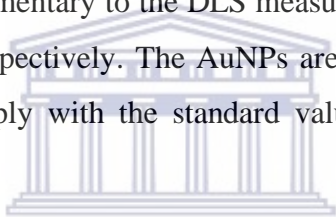
### 4.3 Dynamic Light Scattering (DLS) and Zeta Potential

#### 4.3.1. Car-AuNPs

Crushing the cardamom seeds prior to synthesis clearly yielded a more favourable colloidal solution with the resultant colour comparing positively to that of the citrate stabilized AuNPs (Figure.1.1 A and C). Whole cardamom seeds yielded AuNPs that were considerably polydisperse (PDI:  $\pm 0.4$ ), and prone to aggregation made clear by the colour of the AuNP solution. The AuNPs synthesized from extracts of crushed cardamom seeds differ from the whole Car-AuNPs both in size, shape and dispersity. Crushed seed extract yielded AuNPs that were monodisperse (PDI:  $\pm 0.2$ ). In both cases however, there was a discrepancy between the sizes with DLS and those measured with TEM (Table 3.1). This discrepancy is possibly due to organic molecules that are absorbed or chemisorbed onto the surface of the AuNP in suspension (Salata, 2004). This suggests that additional phytochemical solvent layers are present containing biomolecules with varying molecular weights causing the greater size measured when compared to TEM (approximately 11 nm in diameter) and the commercial AuNPs. According to Green and Hersam, 2010, the extreme variability in composition and concentration in different plant extracts present a challenge, making it difficult to establish tightly controlled, reproducible synthesis protocols (Green & Hersam, 2010). With that being said, the Car-AuNPs produced in this project appear to be superior to the Car-AuNPs initially produced by Pattanayak *et al* in 2013, their final AuNPs were double the size (hydrodynamically measured: 423.3 nm) of those created in this project (Pattanayak, et al., 2013). It is probable that the specific adapted extract preparation that was used in this study together with the temperature controlled synthesis caused the improvement in AuNP quality.

#### 4.3.2 Commercial (Citrate Stabilized) AuNPs

The sizes of AuNPs are measured with TEM, which is used as an estimate of the core size of AuNPs. DLS measures the core of the AuNPs within suspension, however, hydrodynamic light scattering layers surrounding the AuNPs result in larger sizes than what is recorded by other methods. (Abbai, et al., 2016). According to Coradeghini *et al*, it is normal to observe a difference in particle size made in a vacuum by electron microscope than those made in solution using DLS, since the physical parameter measured is fundamentally different. Using 5 nm and 15 nm citrate stabilized AuNPs, Coradeghini *et al* revealed that DLS measurements yielded sizes that were 4.5 and 5 nm greater in size than AuNPs measured by STEM respectively. Both the measured 10 nm and 50 nm AuNPs sizes, were greater than the core sizes recorded by electron microscopy (Table 3.1). Both measured an additional 23 nm (33.47 d.nm) and 15 nm (65.64 d.nm) respectively. The sizes remained relatively confined (to core sizes and DLS measurements outlined by suppliers) and the presence of single peaks for each AuNP, referred to moderate size distributions as confirmed by the polydispersity indices of the AuNPs (0.2 and 0.1). Based on this data, it could be concluded that the AuNPs were stable and monodisperse. Supplementary to the DLS measurements, the charge of the AuNPs were -32.8 mV and -35.1mV respectively. The AuNPs are considered anionic and stable as the charges of the AuNPs comply with the standard values of AuNP charge as outlined above.



The 5 nm AuNPs, however, showed an unexpected increase in size (176.4 nm). The result suggested a level of agglomeration in the AuNPs which was made evident by the multiple peaks present (Figure. 3.5 A). Additionally, a high PDI of  $\pm 0.4$ , indicated that the distribution of the NPs within solution was imbalanced and that agglomerates detected as large AuNPs existed within solution. Analysis of the percentage of AuNPs falling within certain size ranges however, revealed that the greater proportion of AuNPs in solution measured 15 nm whereas the minor proportion measured above 1000 nm which affected the average diameter recorded. The major proportion of AuNPs falling within the appropriate size range still served as confirmation of the correct AuNP size. The zeta potential (-44.1 mV) of the 5nm AuNPs indicated that the solution was relatively stable along with the wine red colour (Figure 1.1 B) of the 5 nm AuNP solution. In order to resolve the problem of agglomeration, the AuNPs were all filtered prior to experimentation. Filtering AuNPs prior to treatment served an additional purpose of alleviating the polydispersity seen within the AuNPs. We believe that by filtering the AuNPs through 0.2  $\mu\text{m}$  filters, a narrower size distribution is achieved due to the agglomerates becoming trapped within the filter (see Figure 5.4 of the Addendum).

#### 4.4 TEM, EDS and SAED

Transmission electron microscopy is a commonly used imaging technique which allows the visualization of multiple substances at a high resolution. It provides the true (core) size of an AuNP. The Car-AuNP size and shape was visually confirmed by TEM. The images revealed morphological variability (spherical, triangular, rod-shaped, cuboid and hexagonal) among the AuNPs synthesized with whole cardamom seeds (Figure 3.7 B and D) whilst the AuNPs synthesized with crushed cardamom were uniformly spherical (Figure 3.7 A and C). Levels of agglomeration were also present in both samples but to greater levels within the AuNPs synthesized from the whole cardamom seeds. At greater resolutions (2 nm), the crystalline nature of the AuNPs were revealed by the lateral fringes demarcating the AuNPs from its centre to its edge (Figure 3.7 E and F). Furthermore, elemental analysis (Figure 3.8 A and B) showed that the NPs consisted of gold (the Copper (Cu) and Carbon (C) present within the EDS spectra is due to the grid (coated with Cu and C on each surface respectively) on which the AuNP samples were placed for imaging)). The intense bright spots on the speckle pattern of SAED (Figure 3.9) showed that the NPs were indeed crystalline corresponding to the lateral fringes seen within the TEM images and thus served as final confirmation of successful AuNP synthesis. Similar results could be seen in a study by Sujitha & Kannan, 2013 wherein morphological variability in AuNP shapes produced by green synthesis was exhibited with TEM (Sujitha & Kannan, 2013). According to Sujitha & Kannan, 2013, blunt angled nanotriangles are a result of the shrinking process arising from the minimization of surface energy. The presence of large extract quantities cause strong interactions between protective biomolecules and surfaces of nanoparticles preventing nascent nanocrystals from sintering. Increasing the quantities of extract, increases the interaction, leading to size reduction of nanoparticles and sphere formation (Sujitha & Kannan, 2013). Additionally, the authors confirmed AuNP crystallinity and fcc structure by SAED analysis corresponding to the findings of this study.

## 4.5 Stability testing

An important aspect of nanoparticle characterization is measurement under conditions that resemble a physiological *in vitro* environment. One of the important parameters is the stability and the level of aggregation of AuNPs in different media commonly used with biological assays (Pavlin & Bregar, 2012). Therefore, stability tests were performed wherein AuNPs were exposed to increasingly complex biological media for 24 hours at 25 and 37 °C. The addition of AuNPs to biological media resulted in an immediate change in their spectra. However, with the exception of the spectral curves for PBS (due to particle aggregation occurring upon the addition of salt containing buffers) (Sharma, et al., 2015) (Figure 3.10 A-D), the AuNPs maintained their spectra when compared to the spectral curves of AuNPs without the addition of media (Figure 3.2-3.4.). This stability disappeared with certain conditions after a 24 hour incubation with the 5 nm, 10 nm and 50 nm AuNPs whilst the Car-AuNPs retained a level of stability (Figure 3.11 A-D).

A multitude of factors may have contributed to the findings obtained, however the most likely factor is the specific synthesis method. The 5, 10 and 50 nm AuNPs had previously been synthesized commercially and stabilized by capping with citrate. These AuNPs remained in storage at 4 °C until required whereas the Car-AuNPs were synthesized when needed. Thus, the difference in the storage time frame between the green AuNPs and chemically synthesized AuNPs may have affected the difference in stability over time prior to stability testing. The second factor for consideration is the citrate coating of the AuNPs. According to Sharma *et al*, citrate as a capping agent weakly associates with the NP surface and is readily displaced by a range of other molecules including amines, thiols, polymers, proteins and antibodies (Sharma, et al., 2015). As soon as the particle comes into contact with heterogenous environments, liquid or gaseous, smaller structures attach to the surface of the particle. This surface is known as the corona in biological environments where biomolecules are present (Elsaesser & Vyvyan Howard, 2012). According to the findings of Chegel *et al*, these organic molecules contain both thiol and amine groups that both strongly promote NP aggregation (Chegel, et al., 2012).

Closer assessment of the incubation conditions revealed that the greatest level of agglomeration occurred at 37 °C within media and supplemented media. This could be due to the activation of serum proteins at 37 °C within the culture media, usually present to cater to the cells cultured in it. In this case, the increased activation of these proteins may have

resulted in greater protein corona development resulting in higher levels of AuNP aggregation. According to Elbagory *et al*, the flattening of SPR is due to the formation of larger particles. The stability levels of Car-AuNPs are also substantiated by the findings of their study wherein green AuNPs synthesized from different extracts exhibited excellent stability after 24 hours (Elbagory, et al., 2016).

#### 4.6 AuNP uptake

ICP-MS was performed in order to determine whether AuNPs had successfully been taken up into the cells. Concentrations of 2.5 µg/ml, 5 µg/ml and 10 µg/ml of 10 nm and 50 nm AuNPs were applied to the cells for 24 hours and their uptake measured after the respective incubation period. The quantities yielded in parts per billion (ppb) were converted in order to obtain the amount of AuNP uptake per cell as well as the total quantity in µg/ml (Table 3.2). The uptake of AuNPs by the cells was influenced by the concentration of the AuNPs used. More gold was detected in cells exposed to higher concentrations of AuNPs. The greatest level of uptake was exhibited by the 10 nm AuNPs (Figure 3.12). Approximately 92%, 90% and 84 % of the 10 nm AuNPs were taken up after exposure to concentrations of 2.5 µg/ml, 5 µg/ml and 10 µg/ml respectively whereas ~72% of all the concentrations applied of the 50 nm AuNPs were effectively, internalised by the cells. These findings contradict a multitude of studies wherein comparisons between AuNPs of different sizes were assessed for their uptake capabilities. A study by Chitrani *et al*, using ICP-AES, revealed that the larger AuNPs (50 nm spherical AuNPs) were taken up more efficiently than smaller AuNPs (14 nm) and larger AuNPs (74 nm) (Chitrani, et al., 2010). Additionally, different types of NPs (50 nm in size) have been shown to exhibit highly efficient endocytosis capabilities which is conjectured to be due to similar vesicle sizes required at the initial cellular stage of entry for several viruses (Osaki , et al., 2004; Chitrani, et al., 2010; Chu, et al., 2011).

Endocytosis is the major route of NP transport across the membrane and is generally classified into phagocytosis and pinocytosis. Four subclasses of pinocytosis are present in all cell types namely, clathrin-dependent endocytosis, caveolae-dependent endocytosis, micropinocytosis and clathrin-and-caveolae independent endocytosis based on the proteins involved in the pathways (Hillaireau & Couvreur, 2009). NPs are generally considered to enter the cells via either of these pinocytic pathways however, it has been described that there are differences in how nanomedicines interact with the cytomembrane. Different types of NPs enter cells and travel into the cells via different routes (Kou, et al., 2013). However,

some pathways are still insufficiently understood and factors affecting the pathway of nanomedicines entering the cells are not absolutely proven (Sahay, et al., 2010). Although a trend in size dependent endocytic mechanisms exists, additional factors may contribute to AuNP uptake other than size. According to Sahay *et al*, most studies performed so far do not emphasize the link between cell origin and various endocytic pathways. Furthermore, the known cellular pathways may be differentially expressed or even totally absent in selected cell types depending on cell phenotype (Sahay, et al., 2010). Self-regulated membrane tension by cells are usually small. However, with increasing NP size, wrapping the NP would put the membrane in increasingly high tension (Zhang, et al., 2015). Thus an upper limit of NP radius exists beyond which endocytosis does not occur. This tension could also be a contributing factor to consider as various studies revealed decreasing cellular uptake with larger AuNPs. Therefore, the possibility exists that a difference in cell type may cause an alteration in membrane tension resulting in lowered tolerance of larger AuNPs and could be a contributing factor towards the discrepancy in uptake effect seen here when compared to literature (Osaki, et al., 2004; Chitrani, et al., 2010; Chu, et al., 2011).

#### 4.7 *In vitro* assessments

The mitotic index (MI) (Figure 3.17) indicated that the active compound of cardamom (1.8 cineole) greatly inhibited the capacity of the cells to divide whilst Car-AuNPs stimulated the division of the cells when compared to controls. 1.8 cineole has been found to inhibit cell growth (Murata, et al., 2013). In this study, 1.8 cineole also exhibited an outspoken inhibitory effect on cell viability and thus cell growth. Based on work by Rajan, *et al*, Car-AuNPs were shown to inhibit cell growth (Rajan, et al., 2017). According to Diaz *et al*, the inhibitory and sometimes toxic effects of the Car-AuNPs nanoparticles is highly dependent on the type of cell encountered. This is due to variations in cell physiology, proliferation state, membrane characteristics and phagocyte characteristics among different cell types (Díaz, et al., 2008). This statement is further supported by the findings of Patra *et al*, who explored non functionalized AuNPs in multiple *in vitro* models. Whilst the AuNPs managed to induce death responses in the lung cancer cells, no effect was seen in hamster kidney cells nor liver cancer cells (Patra, et al., 2007). Another possible explanation is that green synthesized AuNPs possess several more solvent layers than the AuNPs synthesized via chemical synthesis procedures (Salata, 2004). Thus, even though 1.8 cineole was found to drive the synthesis reaction of Car-AuNPs (Singh & Srivastava, 2015), it is possible that 1.8 cineole

does not form part of the proportion of phytochemicals surrounding the AuNPs. In a study by Nune *et al*, a number of phytochemicals present in black tea were considered the major role players in the overall reduction reactions of  $\text{HAuCl}_4$ . Via a systematic investigation of their individual roles, the authors found that the cocktail of phytochemicals present in the tea acted synergistically in stabilizing the AuNPs (Nune, et al., 2009). It can therefore be speculated that the AuNPs stemming from the cardamom aqueous extract were created by a chemical reaction that was driven by 1.8 cineole. However, there is a likelihood that the phytochemicals existing in addition to 1.8 cineole within the bulk phytochemical complex, were responsible for capping the AuNPs, resulting in phytochemicals with stimulatory capacities covering the AuNP surface.

Stimulation of mitosis exhibited by Car-AuNPs could also be seen in cells exposed to the 5nm, 10nm and 50 nm AuNPs (Figure 3.17). However, the level of stimulation was minimal when compared to Car-AuNPs. Additionally, doubling the concentration of citrate stabilized AuNPs (10  $\mu\text{g}/\text{ml}$ ), either had no effect on mitosis or decreased the level of cell division stimulation. The effect was dose and size-dependent. The higher (10  $\mu\text{g}/\text{ml}$ ) concentration of AuNPs, decreased the mitotic index and 5 nm AuNPs at 5  $\mu\text{g}/\text{ml}$  caused a minimal increase (from 6% in controls to 8.5% in the 5nm treated sample) in mitosis but no effect at the higher concentration (10  $\mu\text{g}/\text{ml}$ ). Both concentrations of the 10 nm and 50 nm (5 and 10  $\mu\text{g}/\text{ml}$ ) AuNPs had no significant effects on mitosis of the CHO cells (Figure 3.17). Although, the effect of the commercial AuNPs on mitotic index contrasts what is exhibited in the cell proliferation experiment however, it is important to note that the cell proliferation experiment occurred under high concentrations of AuNPs (50  $\mu\text{g}/\text{ml}$ ) (Figure 3.13). Thus, it is plausible that the stimulatory effect on mitosis shown in Figure 3.17 is lost with increasing concentrations of citrate stabilized AuNPs. Although of the commercial AuNPs, the 50 nm AuNPs caused the greatest stimulatory effect (from 6 % seen in control to approximately 9% exhibited in the treated sample) on the mitosis of the cells; its influence on the proliferative capacities of the CHO cells at higher concentrations did not affect cell proliferation in the same cytotoxic manner as the smaller AuNPs and had no effect on cell proliferation at lower concentrations after 24 hours (Figure 3.15).

Similarity does exist in the cell proliferation and mitosis experiments, in that the Car-AuNPs stimulates cell propagation in both cases and to greater extents at increasing concentrations. Furthermore, The 5 nm and 10 nm AuNPs affect cell proliferation and mitosis similarly in that the 5 nm induced the greatest response (both inhibitory and stimulatory) whilst the 10 nm

AuNPs took on a more modulatory role. Simply put, the responses induced, though different, was similar in magnitude in both assays per exposure (AuNP type) condition. Similar results on the invasive capacities of cells and AuNP size were observed by Liu *et al.* In a lung cancer model, the authors found that 5 nm AuNPs inhibited the growth of A549 cells but increased cell invasion. Corresponding increases in cell invasion was exhibited by cells exposed to 10 nm AuNPs, but no influence on viability or invasion could be seen in cells exposed to larger AuNPs (20 and 40 nm). These results suggest that the increased level of reactivity exhibited by smaller AuNPs relative to the larger AuNPs could be due to their increased surface area resulting in a greater AuNP to cell interaction. Additionally, the study by Liu *et al.*, shows that AuNPs can induce variable stimulatory and inhibitory effects *in vitro* when applied in different assays corresponding to the findings of the current study (Liu, et al., 2014).

## **4.8 Radiation Damage**

### **4.8.1 The Clonogenic cell survival assay**

To evaluate the radiosensitization effects of 50 nm AuNPs, the cell survival clonogenic assay was conducted to assess the self-renewal efficiency of CHO-K1 cells after exposure to the abovementioned treatments (see Figure 3.18).

Decreases in colony formation were observed when comparing the reference radiation position to the middle of the SOBP, pointing to a gradual decrease in cell survival and thus an increase in biological effectiveness with depth. There was a reduction in surviving fractions from 0.082 in the entrance plateau position to 0.059 in the middle position of the SOBP. The presence of the AuNPs resulted in an even greater decrease in cell survival from 0.021 at the entrance plateau to 0.013 in the middle of the SOBP.

Compared to the cell survival fractions observed for proton radiation alone, a clear dose enhancement effect of 74.4% for the entrance plateau positions and 78% for the middle position of the SOBP is visible. In a study by Ma *et al.*, AuNPs of different shapes (gold nanospheres (GNPs), gold nanospikes (GNS), and gold nanorods (GNR) of similar sizes (average size ~50 nm each) were investigated as potential radiosensitizers (Ma, et al., 2017). After an incubation period of 24 h with the AuNPs, cellular uptake was revealed to increase in order of GNP>GNS>GNR. Based on gold mass, the GNPs showed the highest level of uptake. Additionally, employing the colony forming assay, the study revealed that radiosensitization with 6 MV X-rays (4Gy) were most pronounced in the presence of GNPs and sensitization enhancement ratios (SER) proved that the AuNPs enhanced radiation

therapy. The ratios calculated were 1.62, 1.37 and 1.21 respectively, corresponding to the level of cellular uptake of the GNPs. The AuNPs used in this study were also 50 nm spherical AuNPs and based on the colony survival data for 6 Gy protons, an increase of approximately 75% in effectiveness could be observed for AuNP treated cells compared to untreated cells (Figure 3.18).

Polf *et al* 2011, investigated the enhancement of cell death and RBE based on the presence of AuNPs in prostate cancer cells upon proton radiation. The research group exposed DU145 cells containing phage-scaffold AuNPs with a diameter of  $44 \pm 8$  nm (internalizing phage plus gold nanoparticles) to 160 MeV protons. Reference data was produced by exposing non-treated cells to the same incremental doses of clinical  $^{60}\text{Co}$  photons to determine the baseline sensitivity of DU145 cells to the reference radiation quality. Using the standard *in vitro* clonogenic assay, the findings of the study revealed that DU145 cells are more sensitive to proton irradiation and the AuNP treated cells showed an even further decrease in cell survival, representing an approximate 15-20% dose enhancement for Au treated cells. The authors attributed the effect to proton-Au scatter interactions that increase the ionization density within cells (Polf, et al., 2011). The dose enhancement effect reported by Polf *et al*, was smaller than the effect observed in the current study, however, there are differences in the experimental conditions and both studies showed the reduction in cell survival due to increasing ionization events upon AuNP-proton interaction.

Unfortunately, limited data is currently available on the depth-dependent increase in the radiosensitization effect of AuNPs for proton irradiation. Li *et al*, observed an enhanced cell death with increasing LET of the proton radiation (Li, et al., 2016). However, this group worked with a 2 MV Tandem accelerator, resulting in protons of a very low energy and hence a higher biological effectiveness than the higher energy protons used in clinical practice. A human epidermoid carcinoma cell line (A431) was treated with 5 nm and 10 nm AuNPs and irradiated with protons of 25 keV/ $\mu\text{m}$  and 10 keV/ $\mu\text{m}$ . A marked radiosensitization effect was observed for the high LET protons, but not with the 10 keV/ $\mu\text{m}$  protons. Furthermore, the effect was more pronounced for 10 nm AuNPs than for 5 nm AuNPs. In our study, however, the LET of the protons at the entrance plateau position corresponded to 3.39 keV/ $\mu\text{m}$  for the entrance plateau position and 3.624 keV/ $\mu\text{m}$  for the SOBP position (unpublished data, Vandevoorde, 2017).

#### 4.8.2 Chromosomal Damage

The cytokinesis block micronucleus assay was used to determine the amount of radiation damage induced after exposing the cells to AuNPs and protons by using micronuclei as a biomarker for chromosomal damage.

The assessment of MNi yields in cells after pre-incubation with AuNPs after each individual incubation period in cells, and subsequent irradiation with protons revealed that the AuNPs do interact with protons. An increase in micronuclei frequency could be seen in cells exposed to 5 or 10 nm AuNPs (50 µg/ml) and protons compared to cells treated with protons or AuNPs alone. At all depths along the SOBP, the observed dose enhancement effects were different when compared to irradiated controls. However, when compared amongst each other, the middle of the SOBP showed a statistically significant difference between the 5 and 10 nm AuNP treated cells namely, 251MNi/500 BN cells and 286MNi/500 BN cells respectively. This finding is consistent with results reported by Li *et al*, wherein the A431 cell line was pre-incubated with 5 or 10 nm AuNPs and subsequently treated with 10 and 25 keV µm protons. As previously reported, a more pronounced effect was observed in cells incubated with 10 nm AuNPs compared to 5 nm AuNPs. This outcome could be partially attributed to AuNP uptake. Due to the greater size of the AuNPs, a greater AuNP mass is present within cells, increasing the probability of interaction with protons and AuNPs. Thus an increased enhancement is expected for AuNPs that are slightly larger due to an increased gold atom presence within the cells with which the protons can interact (Li, et al., 2016). Therefore, the size dependent effect seen (10 nm producing more chromosomal damage) in Figure 3.20 could be dependent on an increase in gold mass within the cells.

In contrast to the result obtained with the commercial AuNPs, cells pre-incubated with ± 11 nm Car-AuNPs showed a decrease in MNi expression in response to protons except for the position in the middle of the SOBP (see Figure 3.20). Both the proximal and distal position in the SOBP yielded interaction indices (Unity) lower than 1 (0.94 and 0.72 respectively) (addendum), pointing to a radioprotective effect, which might be due to the previously described stimulation of proliferation in CHO cells. This protective effect seen could also be credited to the biological species within the phytochemical complex. For low-LET radiation 1/3 of DNA damage occurs via direct damage whilst 2/3 of DNA damage occurs due to

indirect damage (Azzam, et al., 2012). As previously described in section 1.4 of Chapter 1, indirect damage produces a multitude of DNA lesions by producing free radicals. By free radical scavenging and upregulating endogenous enzymes capable of neutralizing free radical induced cellular damage, phytochemical constituents can effectively confer radioprotective capabilities onto cells (Paul, et al., 2011). In a study by Dhuley, rats fed with high fat diets and cardamom were monitored for antioxidant enzyme activity. The study showed a marked enhancement of antioxidant enzyme activity proving that an antioxidant protection effect appeared to occur due to a cardamom supplemented diet in rats (Dhuley, 1999). In addition to the bulk monoterpenes found in cardamom (section 1.3.2, chapter 1), a large reservoir of polyphenols (e.g flavonoids) exists within the phytochemical complex of cardamom (Daneshi-Maskooni, et al., 2017). Polyphenols are competent reactive oxygen species scavengers. Finally, as previously described in section 1.3.2 of chapter 1, it has been proven that Car-AuNPs are effective reactive oxygen species scavengers (Soshnikova, et al., 2017). Thus the radioprotecting effect seen with the Car-AuNPs could also be ascribed to the presence of polyphenols capping the AuNPs as solvent layers.

An interaction between 50 nm AuNPs and protons was also visible (Figure 3.21). As seen within the experiment mentioned above, a greater level of micronuclei frequency was seen in cells exposed to 50 nm AuNPs and protons when compared to cells exposed to 50 nm AuNPs or protons alone. Pronounced effects could be seen at all positions of the SOBP in cells exposed to 50 nm AuNPs and 2 Gy protons. Statistically significant differences existed between the MNi induced when the cells were irradiated at the different SOBP positions and their controls as well as the 80% Dmax position. However, no statistically significant differences existed between MNi at different positions (except the middle of the SOBP which is due to an uncharacteristic decline in micronuclei frequency within the irradiated controls). This radiosensitizing effect was also reflected in the dose enhancement factors seen at these positions with the distal portion of the SOBP in particular, producing a Unity of 1.2 (Figure 5.6 of Addendum). This effect is also present at higher doses (4 Gy), and after a longer pre-incubation period (24 hours) with 50 nm AuNPs (Figure 3.22). For the irradiated controls, we observe an increase in MNi frequency with depth along the proton beam as shown in both Figure 3.21 and 3.22. This is somewhat expected, as a great amount of studies has determined an incremental increase in RBE to be seen with increasing depth. This is a direct consequence of an increase in ionization density with greater depths along the proton beam due to a decrease in proton energy (Michaelidesová, et al., 2017).

However, this increase in induced radiation damage with depth was not observed in cells treated with AuNPs where the dose enhancement remained more or less the same for each position. This can be explained by a simulation performed by Lin *et al*, in which the Monte Carlo simulations predicted interactions of a single 50 nm AuNP particle with 10 MeV and 150 MeV protons (Lin, et al., 2014). Their results presented similarities to the findings of this study. The simulation anticipated that protons would interact with 50 nm AuNPs and that a DEF up to 14 times greater than normal proton irradiation could be seen. Additionally, AuNPs enhanced the dose of administered protons independently of the position along the peak and with greater efficiencies at 10 MeV than 150 MeV energies (Lin, et al., 2014). This finding could explain the effects seen in Figure 3.21. Per position, a randomized increase in micronuclei frequency was seen with dose enhancement being lost at the 80 % Dmax position when compared to the distal position of the SOBP. This loss of enhancement could be attributed to a steep increases in ionization energies in distal regions of the beam resulting in decreased dose enhancement capabilities by AuNPs. The minimal increase in MNi frequency when compared to non-treated controls at higher doses (4 Gy) on the other hand, could in fact be a direct result of increased dose.

Another factor to consider is AuNP size. Findings by Chitrani *et al*, showed that 50 nm AuNPs exhibited greater uptake efficiencies when compared to smaller AuNPs. Additionally, radiosensitization was seen to greater extents with photons with 50 nm AuNPs when compared to AuNPs that were larger and smaller than 50 nm AuNPs (Chitrani, et al., 2010). However, when comparing the dose enhancements of the 10 nm AuNPs (Figure 3.20) to that of the 50 nm AuNPs (Figure 3.21) in the current study, a greater level of enhancement is seen with the smaller AuNPs. This is in agreement with the ICP-MS results, which indicated a higher uptake of 10 nm AuNPs compared to 50 m AuNPs (Table 3.2), which may have been responsible for a larger dose enhancement effect. According to Li et al, due to the greater surface area of AuNPs with decreasing size, the “hit probability” of protons with AuNPs is vastly improved (Li , et al., 2016).

Due to the large number of electrons in atoms with high atomic numbers, such as gold, many electrons can be released in Auger cascades in addition to the primary ionization process. Radiosensitization with AuNPs is largely attributed to this Auger effect when working with keV X-rays, hence a Monte Carlo simulation by Lechtman *et al*, explored radiosensitization due to Auger electron emission as a function of AuNP size. The authors found that three distinct zones could be identified in the surrounding media from AuNP radiosensitization

upon interaction with photons. The first, comprised about 3-32% of the total escaping energy and extends about 2  $\mu\text{m}$  from the AuNP surface due to escaping Auger and photon electrons. Subsequently this zone has an increased RBE due to the increased LET of these particles. As a consequence, the radioenhancement due to AuNPs is largely caused by the energy deposits of this zone. The limiting factor for the use of larger AuNPs however, is that they tend to internally absorb the short range low energy electrons due to their high stopping power for low energy electrons, reducing the relative energy contributions of the Auger electrons (Lechtman, et al., 2011). The dominant process of proton interactions with gold is the production of secondary electrons via small angle scattering. While photon-induced ionizations occur homogeneously in the medium, the situation is drastically different for proton radiation. Considering fluences typically employed in proton therapy and the small diameter of AuNPs, the direct traversal of a proton through a NP is much less probable (Walzlein, et al., 2014). Contrasting the inner-shell ionizations seen in photon-gold interactions, these events commonly lead to the ejection of low energy electrons from outer atomic orbitals. It was revealed that Auger electrons contribute only 1.5 % of AuNP mediated dose and that of the variety of radiation modalities, clinically used energies produce secondary electrons of the lowest energies when compared to those produced by other types of irradiation (Lin, et al., 2014). Thus, the decrease in Auger electron production by protons and its possible absorbance by 50 nm AuNPs could explain the decrease in MN1 expression depicted in Figure 3.21. Even though the AuNPs did enhance the effect of the applied proton doses on the cells, the enhancement seen was not as pronounced as the level of dose enhancement caused by the 10 nm AuNPs in Figure 3.21. An additional factor to consider however, is AuNP quantity. As mentioned above, it is likely that the sensitization effect caused by the 10 nm AuNPs could be due to an increased gold mass within cells. In addition, ICP-MS results showed a better cellular uptake of the 10 nm AuNPs compared to the 50 nm AuNPs.

After exposing the cells to the 50 nm AuNPs for 24 hours (Figure 3.22), the same level of dose enhancement was exhibited when compared to the proton interaction with cells pre-incubated with 50 nm AuNPs for 4 hours. The increase in exposure time of CHO cells to AuNPs may have caused the minimal increase in dose enhancement effect exhibited. The estimated doubling time of CHO cells is 15 hours, thus, within the 24 hour incubation period the CHO underwent mitosis resulting in the division of endocytosed AuNPs between daughter cells causing a decreased quantity of AuNPs within individual cells though

increased AuNP uptake could have occurred due to the increased incubation period (Kim, et al., 2012). It is also important to note the enhancement effect caused by the 50 nm AuNPs was induced via an applied concentration that was 5 times lower than the concentration of the 10 nm AuNPs applied to the cells. According to Lechtman *et al*, the applied concentration of AuNPs to the cell is another important parameter governing optimal AuNP-irradiation interaction (Lechtman, et al., 2011). Thus it is plausible, that an increase in 50 nm AuNP concentrations to a quantity that does not distort the media: AuNP ratio *in vitro* could lead to greater levels of radiation damage due to an increased presence of AuNPs directly correlating to increased gold mass within cells.

It is unfortunately not possible to evaluate which size of the AuNP has the greatest dose enhancement capability, since the CHO cells were exposed to different concentrations of 5 or 10 nm (50 µg/ml) and 50 nm (10 µg/ml) for 4 hours. Future experiments are needed with similar concentrations of AuNPs and similar incubation times to investigate this further.



### 4.8.3 Cell cycle kinetics

Flow cytometry is a technique that is able to make multiple, objective, simultaneous measurements at the single-cell level at the rate of several events per second (Wilson & Marples, 2007). Flow cytometry incorporating the PI staining method was used to assess the effect of AuNPs, protons and the combination of AuNPs and protons on cell cycle progression.

CHO-K1 cells were exposed to 4 different exposure scenarios that involved Car-AuNPs and protons (50 µg/ml), 5 nm AuNPs (50µg/ml), 10 nm AuNPs (50 µg/ml) and 50 nm AuNPs (10 µg/ml). These were all pre-incubated within cells for 4 hours prior to irradiation with 6 Gy protons.

#### 4.8.3.1 Car-AuNPs

Car-AuNPs proved to have a minimal effect on the cell cycle when compared to controls (Table 3.3). Car-AuNPs stimulated cell growth (Figures 3.13 and 3.17) so no changes in cell cycle progression would be observed in these samples. Car-AuNPs exhibits no disruptive activity to cellular mechanics resulting in unperturbed cell cycle progression. The addition of protons however, revealed that the cell populations in G<sub>2</sub>/M decreased in favour of a 10 % increase of the cell population in G<sub>0</sub>/G<sub>1</sub>. The S-phase remained relatively unchanged. Also known as the growth and longest phase of the cell cycle, G<sub>0</sub>/G<sub>1</sub> occurs with the aid of stimulation by growth factors. Thus, the stimulatory mechanism previously exhibited by Car-AuNPs may have played the same stimulatory role on the cell cycle of the CHO-K1 cells resulting in a longer G<sub>0</sub>/G<sub>1</sub> and decreased G<sub>2</sub>/M. The shorter G<sub>2</sub>/M may also be due to the radioprotective mechanism of Car-AuNPs previously described resulting in Car-AuNPs desensitizing the cells to radiation causing a shorter G<sub>2</sub>/M. This was also made evident by a decrease in RCGG from 2.52 (Table 5.8 of Addendum) for irradiated controls to 1.90 for irradiated samples with Car-AuNPs.

#### 4.8.3.2 5 nm AuNPs

The 5 nm AuNPs showed some effect on cell cycle progression when compared to its non-irradiated control. A decrease in the G<sub>0</sub>/G<sub>1</sub> population from 55.22% to 48.96% (Table 3.4) with an increase in the G<sub>2</sub>/M population from 31.92% to 37.27% occurred whilst the changes to the S-phase population was minimal. The modest effect seen on cells could be due in part, to the uptake efficiency of the AuNPs. Uptake efficiencies measured by using the mean side scatter of the control and treated samples to produce a ratio (Roa, et al., 2009), revealed that the 5 nm AuNPs showed the least amount of endocytosis (0.82) when compared to its other AuNP counterparts (Fig of 5.2 of the Addendum). It has already been established in previous sections that in order to see similar effects to the larger AuNPs, greater amounts of smaller sized AuNPs need to be applied in order to observe any significant effects due to the smaller AuNPs resulting in less gold mass presence within the cells. However, this finding contradicts the work of Liu *et al*, wherein 5 nm AuNPs arrest the cell cycle within the G<sub>0</sub>/G<sub>1</sub> phase of the cell cycle (Liu, et al., 2014). However, the NPs applied by Liu *et al* had a longer incubation period (24 hours) with 50 µg/ml of AuNPs which could account for the difference in effect seen. When assessing the response to radiation on the cell cycle, similar minimal changes to the cell cycle kinetics could be seen. This could be attributed to the decreased amounts of AuNPs resulting in less interaction with protons. The effect seen does not correspond to the radioenhancement effect exhibited by the 5 nm AuNPs in the CBMN assay (Figure 3.20), thus further investigation is required to validate this result.

#### 4.8.3.3 10 nm AuNPs

The 10 nm AuNPs induced a substantial G<sub>1</sub>/G<sub>0</sub> block when compared to non-irradiated controls. An increase from 33.94% to 71.70% (Table 3.5) occurred with subsequent decreases in the S-phase and G<sub>2</sub>/M populations. As previously described in section 1.6.4.1., G<sub>1</sub> arrest occurs in response to genotoxic damage. Arrest can occur by either upregulating p53 or degrading Cdc25A with the ultimate goal of downregulating Cdk2 in order to repress kinase activity of D cyclins resulting in the eventual G<sub>1</sub> arrest. It is likely that the presence of the 10 nm AuNPs within CHO cells influenced the expression of these molecules resulting in G<sub>1</sub> arrest. In response to proton radiation, the majority of the cells accumulated in G<sub>2</sub>/M for all positions along the SOBPs. When comparing the AuNP irradiated samples to these controls, a decrease in the G<sub>2</sub>/M population is visible. The S-phase populations remains relatively unchanged

whilst increases in G<sub>1</sub>/G<sub>0</sub> populations are evident and most pronounced towards the end of the SOBP. One of two events may have occurred which explains the given effect. Either A) the effect seen is due to G<sub>0</sub>/G<sub>1</sub> taking on an intermediate position towards radiation sensitivity resulting in cells being re-distributed amongst G<sub>0</sub>/G<sub>1</sub> and G<sub>2</sub>/M or B) the stall seen without radiation in response to 10 nm AuNP presence at G<sub>0</sub>/G<sub>1</sub>, persists during radiation, thus a radiosensitizing mechanism may exist. The decline in cell populations stalled in G<sub>0</sub>/G<sub>1</sub> from 71.70% (10nm AuNP non-IR) to 39.42% (10 nm IR) in G<sub>1</sub> (distal SOBP position) and an increase in the accumulation of cells in G<sub>2</sub>/M (52.23%) when compared to the G<sub>2</sub>M populations of the 10 nm non-irradiated control (19.04%). This is further substantiated by the RCGG of the irradiated control in the distal position increasing from 4.60-7.13 (Table 5.2 of Addendum) with the addition of AuNPs. These findings contradict the findings of Liu *et al*, wherein no effect could be seen on the cell cycle kinetics of lung cancer cells with 10 AuNPs alone (Liu, et al., 2014). Additionally the findings of Geng *et al* are also contradicted wherein ~14 nm glucose capped AuNPs created a G<sub>2</sub>/M stall on their own (without radiation) and enhanced the delivered dose of 90kVp and 6 MV X-rays by further increasing the cell populations stalled in G<sub>2</sub>/M of SKOV3 cells. This difference in effect is most likely due to the different cell models used across these investigations in relation to ours (Geng, et al., 2011). Furthermore, the AuNPs used in this study were not modified with biomolecules and thus the additional physicochemical parameters that may play a role in the study by Geng *et al* do not factor into the findings of this study. However, the variety in effects reported combined with those from this study warrants further investigation.

#### 4.8.3.4 50 nm AuNPs

The 50 nm AuNPs showed decreased G<sub>2</sub>/M expression (from 25.49 % to 18.03%), increased G<sub>0</sub>/G<sub>1</sub> expression from (33.27% to 42.26%) and similar S-phase expression (from 40.88% to 39.39%) when compared to controls (Table 3.5). However, proton irradiation resulted in a decrease in S-phase accumulation and subsequent increases in G<sub>2</sub>/M cell populations, particularly for the distal SOBP position. Similar effects were observed in cells exposed to 50 nm AuNPs and protons. The increase in G<sub>2</sub>/M population when compared to irradiated controls was minimal. The latter suggests that the 50 nm AuNPs did not affect the radiosensitivity of the cells. Smaller RCGG values and even smaller differences between the values 3.92 and 3.29 (Table 5.11 of the Addendum) when comparing the distal position control to the irradiated AuNP treated sample, confirms the minimal influence on

radiosensitization. This finding is similar to those yielded by the micronucleus data described in section 4.8.2. However it contradicts the findings of Chitrani *et al* wherein 50 nm AuNPs ( $7 \times 10^9$  nanoparticles/ml) were found to exhibit the greatest uptake efficiency and radiosensitization effect in response to X-ray radiation (Chitrani, et al., 2010). Another study by Ma *et al*, 2017, revealed that ~ 50 nm AuNPs (50  $\mu\text{g/ml}$ ) had arrested cells in the G<sub>2</sub>/M phase of the cell cycle possibly sensitizing the cells to X-ray irradiation (Ma, et al., 2017). The lack in correspondence of these studies to the findings of this study could also be due to a different incubation periods. In the study by Chitrani *et al* HeLa cells were exposed to AuNPs for up to 72 hours whilst the report by Ma *et al*, indicated a 24 hour exposure time frame. Findings by Kim *et al*, 2012 revealed that within 10 hours of incubation AuNP uptake did not affect the phases of the cell cycle (Kim, et al., 2012). As the study showed that the 50 nm AuNPs were not endocytosed as efficiently as 10 nm AuNPs and that minimal effects were seen on cells containing 50 nm AuNPs and protons after a pre-incubation period of 4 hours (Figure 3.12), the allocated time (4h) for effective AuNP endocytosis may have been too short resulting in the minimal effect on cell cycle kinetics exhibited by the 50 nm AuNPs.



## SUMMARY

---

In this study, the differential effects induced by AuNPs synthesized using green methods and chemical methods were explored. AuNPs were then administered in conjunction with protons at clinical energies (200 MeV) in order to determine whether an enhancement in radiation effects could be seen due to AuNP presence within the cells.

Initial non-irradiative experiments revealed that chemically synthesized AuNPs induced variable effects in vitro. Decreases in cell proliferation were seen in cells exposed to 5 and 10 nm AuNPs whilst increased mitotic indices were expressed due to 5 and 10nm AuNPs. The 50 nm AuNPs showed little effect on cell proliferation whilst stimulation of mitosis was observed. This result, though variable indicated a size dependent effect of the commercial AuNPs. In contrast, results from both the cell proliferation and mitosis experiments showed that Car-AuNPs clearly stimulated cell growth leading to increased mitotic index readings along with corresponding increases in cell proliferation.

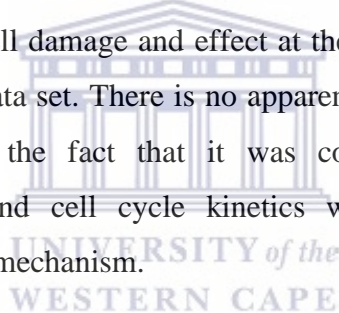
Incorporating AuNPs with proton radiation revealed that an interaction between protons and AuNPs exists. Results observed from the cell survival clonogenic assay showed a marked AuNP induced dose enhancement effect of approximately 75 % when compared to irradiated controls. Data from the chromosomal damage assessments revealed that with the exception of the middle of the SOBP, protons influenced the level of expressed MNi in a depth dependent manner. However, this depth dependent increase in MNi induction was not reflected in the data yielded from cells treated with protons and AuNPs. Furthermore, the effect of AuNP size contradicted the findings stated in literature. Data obtained from ICP-MS and chromosomal damage experiments revealed that the 10 nm AuNPs were internalised more efficiently and exhibited the most pronounced radioenhancement effect compared to the expected theory that this would be exhibited in cells exposed to 50 nm AuNPs. In addition, the radioprotective mechanism exhibited by Car-AuNPs in response to protons requires further investigation. The core size of the Car-AuNPs is similar to the 10 nm AuNPs (in size) yet exerted a completely opposite effect. This led to the suspicion that the biogenic molecules forming part of the corona of Car-AuNPs (Nune , et al., 2009) may have played a radioprotective role by scavenging DNA damaging reactive oxygen species.

Analysis of the effect of the aforementioned treatments on the cell cycle kinetics revealed that the radioprotecting mechanism of the Car-AuNPs persisted throughout different experiments.

On their own, Car-AuNPs affected the cell cycle minimally. Variable effects on the cell cycle were induced by the citrate stabilized AuNPs. The 5 nm AuNPs caused minimal effects with and without protons on cell cycle kinetics whilst 10 nm AuNPs caused cells to accumulate in G0/G1.

The findings of this study allowed for the following to be deduced;

1. AuNPs exert variable effects on cell proliferation, division and cell cycle kinetics that are largely dependent on AuNP size
2. AuNPs and protons do interact however the interaction does not occur in the depth-dependent manner expected
3. Different synthesis procedures can be associated with a differing capacity to modulate proton effects.
4. AuNP concentration plays a central role in AuNP-proton interaction presumably affecting the “hit probability” between protons and AuNPs
5. Though the protons on their own affected the cells in a depth dependent manner, an anomalous decrease in cell damage and effect at the middle of the SOBP occurs and persists throughout the data set. There is no apparent biophysical explanation for this occurrence. However, the fact that it was consistently observed as part of chromosomal damage and cell cycle kinetics warrants further investigation to illuminate an underlying mechanism.

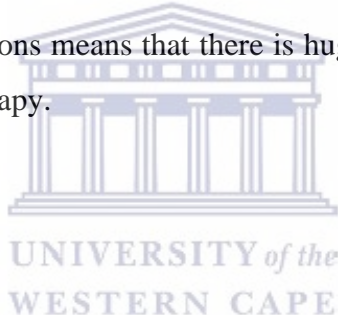


---

## CONCLUSION

---

Stereotactic radiosurgery is a valuable tool as an alternative to surgery for a variety of benign intracranial meningiomas due to the selection of doses that causes total destruction. Conceived to create functional lesions within physiological tracts or nuclei of the brain, stereotactic radiosurgery has been used to treat meningiomas, acoustic neuromas and arteriovenous malformations. Due to increases in the size of the target volume or its proximity to critical structures, clinicians are increasingly using treatment schedules consisting of more than one fraction (Vernimmen & Slabbert, 2010). However, large lesions are more difficult to treat with radiosurgery. Proton beam therapy, with its dose distribution advantage offers an alternative radiation therapy option (Vernimmen, et al., 2005). The interaction of AuNPs and protons in this study is a significant step towards the improvement in the treatment of carcinomas. The dose enhancement capabilities of the AuNPs with protons at clinically relevant energies, with the addition of site targeted radiotherapy due to the conformal delivered dose of protons means that there is huge potential for AuNP application as a radiosensitizer in proton therapy.



---

## REFERENCES

---

- Aaseth, J., Haugen, M. & Forre, O., 1998. Rheumatoid arthritis and metal compounds- perspectives on the role of oxygen detoxification. *Analyst*, Volume 1, pp. 3-6.
- Abbai, R., Mathiyalagan, R. & Markus, J., 2016. Green synthesis using multi-funtional silver and gold nanoparticles from the oriental herbal adaptogen: Siberian ginseng. *International Journal of Nanomedicine*, Volume 11.
- Abdel-Raouf, N., Al-Enazi, M. N. & Ibraheem, I. B., 2017. Green biosynthesis of gold nanoparticles using *Galaxaura elongata* and characterization of their antibacterial activity. *Arabian Journal of Chemistry*, Volume 10, pp. S3029-S3039.
- Adams, F. C. & Barbante, C., 2013. Nanoscience, nanotechnology and spectrometry. *Spectrochimics Acta Part B*, Issue 86, pp. 3-13.
- Ali, M. & Husain, S. S., 2014. Analysis of volatile oil of fruits of *Elataria Cardamomum* (L.) maton and its antimicrobial activity. *World journal of pharmacy and pharmaceutical sciences*, Volume 3, pp. 1798-1808.
- Amendola, V. & Meneghetti, M., 2009. Size evaluation of gold nanoparticles by UV-vis spectroscopy. *Journal of Physics and Chemistry*, Volume 113, pp. 4277-4285.
- Arvizo, R., Battacharya, R. & Mukherjee, P., 2010. Gold nanoparticles: Oppurtunities and Challenges in Medicine. *Expert Opinion in Drug Delivery*, Volume 7, pp. 753-763.
- Azzam, E., Jay-Gerin, J. & Pain, D., 2012. Ionizing radiation-induced metabolic oxidative stress and pro-longed cell injury. *Cancer Letters*, Volume 327, pp. 48-60.
- Balog, S. et al., 2015. Characterizing nanoparticles in complex biological media and physiological fluids with depolarized dynamic light scattering. *Nanoscale*, Volume 7, pp. 5991-5997.
- Barnum, K. J. & O'Connell, M. J., 2014. Cell Cycle regulation by Checkpoints. *Methods in Molecular Biology*, Volume 1170, pp. 29-40.
- Bartek, J., Bartkova, J. & Lukas, J., 1996. The retinoblastoma protein pathway and the resrtiction point. *Cell multiplication*, Volume 8, pp. 805-814.

Battacharjee, S., 2016. DLS and zeta potential- what are they and what are they not?. *Journal of Controlled Release*, Volume 235, pp. 337-351.

Bellie, M. et al., 1998. RBE-LET relationships for cell inactivation and mutation induced by low-energy protons in V79 cells: further results at the LNL facility. *International Journal of Radiobiology*, Volume 146, pp. 159-170.

Bertrand, N. et al., 2014. Cancer Nanotechnology: The impact of passive and active targeting in the era of modern cancer biology. *Advanced Drug Delivery Reviews*, Volume 66, pp. 2-25.

Bhagat, N. & Charturvedi, A., 2016. Spices as an Alternative Therapy for Cancer Treatment. *Systematic Reviews in Pharmacy*, Volume 7, pp. 46-56.

Biosciences, B., 2014. *Cell cycle phases*. [Online]

Available at: [WWW.BDBIOSCIENCES.COM/RESEARCH/APOPTOSIS/ANALYSIS](http://WWW.BDBIOSCIENCES.COM/RESEARCH/APOPTOSIS/ANALYSIS)

[Accessed 04 June 2017].

Blagosklonny, M. V. & Pardee, A. B., 2002. The Restriction Point of the Cell Cycle. *Cell Cycle*, Volume 1, pp. 102-109.

Blecher, K., Nasir, A. & Friedman, A., 2011. The role of nanotechnology in combating infectious diseases. *Virulence*, Volume 2, pp. 395-401.

Bohm, E. L. J. F. et al., 2010. *Radiation Biology: A Handbook for Teachers and Students*. 42 ed. Vienna: IAEA scientific and technical publications.

Britten, R. A. et al., 2013. Variations in the RBE for Cell Killing Along the Depth-Dose Profile of a Modulated Proton Therapy Beam. *Radiation Research*, Volume 179, pp. 21-28.

Brust, M. et al., 1994. Synthesis of thiol-derivatized gold nanoparticles in a two-phase Liquid-Liquid system. *Journal of the Chemical Society, Chemical Communications*, Issue 7.

Budirahardja, Y. & Gönczy, P., 2009. Coupling the cell cycle to development. *Development*, Volume 136, pp. 2861-2872.

Burma, S., Chen, B. P. & Chen, D. J., 2006. Role of non-homologous end-joining in maintaining genomic integrity. *DNA Repair*, pp. 1042-1048.

Butterworth, K. T., McMahon, S. J., Taggart, L. E. & Prise, K. M., 2013. Radiosensitization by gold nanoparticles: effective at megavoltage energies and potential role of oxidative stress. *Translational Cancer Research*, Volume 2, pp. 269-279.

Byrne, J. D., Betancourt, T. & Brannon-Peppas, L., 2008. Active targeting schemes for nanoparticle systems in cancer therapeutics. *Advanced Drug Delivery Reviews*, Volume 60, pp. 1615-1626.

Cappelletti, V., Fioravanti, L., Miodini, P. & Di Fronzo, G., 2000. Genistein blocks breast cancer cells in G2M phase of the cell cycle. *Journal of Cellular Biochemistry*, Volume 79, pp. 594-600.

Chanda, N. et al., 2011. An Effective Strategy for the Synthesis of Biocompatible Gold Nanoparticles Using Cinnamon Phytochemicals for Phantom CT Imaging and Photoacoustic Detection of Cancer Cells. *Pharmaceutical Research*, Volume 28, pp. 279-291.

Chegel, V. et al., 2012. Gold Nanoparticles Aggregation: Drastic Effect of Cooperative Functionalities in a Single Molecular Conjugate. *Journal of Physical Chemistry*, Volume 116, pp. 2683-2690.

Chitrani, D. B. et al., 2010. Gold Nanoparticles as Radiation Sensitizers in Cancer Therapy. *Radiation Research*, Volume 173, pp. 719-728.

Chu, Z., Huang, Y., Tao, Q. & Li, Q., 2011. Cellular uptake, evolution, and excretion of silica nanoparticles in human cells. *Nanoscale*, Volume 3, pp. 3291-3299.

Ciernik, F. et al., 2011. Proton-Based Radiotherapy for Unresectable or Incompletely Resected Osteosarcoma. *Cancer*, Volume 117, pp. 4522-4530.

Clémenson, C. & Marsolier-Kergoat, M.-C., 2009. DNA damage checkpoint inactivation: Adaptation and recovery. *DNA Repair*, Volume 8, pp. 1101-1109.

Curren, W. J. et al., 2011. Sequential vs. concurrent chemoradiation for stage III non-small cell lung cancer: randomized phase III trial RTOG 9410. *Journal of the National Cancer Institute*, Volume 103, pp. 1452-60.

Daneshi-Maskooni, M. et al., 2017. The effects of green cardamom on blood glucose indices, lipids, inflammatory factors, paraxonase-1, sirtuin-1, and irisin in patients with nonalcoholic fatty liver disease and obesity: study protocol for a randomized controlled trial. *Trials*, Volume 18.

Daraee, H. et al., 2014. Application of gold nanoparticles in biomedical and drug delivery. *Artificial cells, Nanomedicine and Biotechnology*, pp. 1-13.

- Das, I. et al., 2012. Antioxidative effects of the spice cardamom against non-melanoma skin cancer by modulating nuclear factor erythroid-2-related factor-2 and NF-kB signalling pathways. *British Journal of Nutrition*, Volume 108, pp. 984-997.
- Datta, L. C. R. & Jaitawat, B. S., 2006. Nanotechnology- The New Frontier of Medicine. *Medical Journal Armed Forces India*, Volume 62.
- DeLaney, T. F. et al., 2005. Radiotherapy for local control of osteosarcoma. *International Journal of Radiation Oncology Biology Physics*, Volume 61, pp. 492-498.
- Dhawan, A. & Sharma, V., 2010. Toxicity assessment of nanoparticles: methods and challenges. *Analytical and Bioanalytical Chemistry*, Volume 398, pp. 589-605.
- Dhuley, J. N., 1999. Antioxidant effects of cinnamon (*Cinnamomum verum*) bark and greater cardamom (*Amomum subulatum*) seeds in rats fed high fat diet. *Indian Journal of Experimental Biology*.
- Díaz, B., Sánchez-Espinel, C. & Arruebo, M., 2008. Assessing methods for blood cell cytotoxic responses to inorganic nanoparticles and nanoparticle aggregates. *Small*, Volume 4, pp. 2025-2034.
- Donzelli, M. & Draetta, G. F., 2003. Regulating mammalian checkpoints through Cdc25 inactivation. *EMBO Reports*, Volume 4, pp. 671-677.
- Dorsey, J. F. et al., 2013. Gold nanoparticle in radiation research: potential applications for imaging and radiosensitization. *Translational Cancer Research*, Volume 2, pp. 280-291.
- DSimaging, L., 2013. *Elemental Analysis using EDS*. [Online] Available at: <http://dsimagingllc.com/elemental-analysis-using-eds/> [Accessed 28 10 2017].
- Dubravka, D. & Scott, D. W., 2000. Regulation of the G1 phase of the mammalian cell cycle. *Cell Research*, Volume 10, pp. 1-16.
- Elbagory, A. M., Cupido, C. N., Meyer, M. & Hussein, A. A., 2016. Large Scale Screening of Southern African Plant Extracts for the Green Synthesis of Gold Nanoparticles Using Microtitre-Plate Method. *Molecules*, Volume 21, pp. 1-20.
- Elsaesser, A. & Vyvyan Howard, C., 2012. Toxicology of nanoparticles. *Advanced Drug Delivery Reviews*, Volume 64, pp. 129-137.

- Encalada, S. E., Willis, J., Rebecca, L. & Bowerman, B., 2005. A Spindle Checkpoint Functions during Mitosis in Early *Caenorhabditis elegans* Embryo. *Molecular Biology of the Cell*, Volume 16, pp. 1056-1070.
- Fenech, M., 2000. The in vitro micronucleus technique. *Mutation Research*, Volume 455, pp. 81-95.
- Fenech, M., 2007. Cytokinesis block micronucleus cytome assay. *Nature Protocols*, Volume 2, pp. 1084-1104.
- Foot, R. L. et al., 2012. The clinical case of proton beam therapy. *Radiation Oncology*, Volume 7, pp. 1-10.
- Fortakis, G. & Timbrell, J. A., 2006. In vitro cytotoxicity assays: Comparison of LDH, neutral red, MTT and protein assay in hepatoma cell lines following exposure to cadmium chloride. *Toxicology Letters*, Volume 160, pp. 171-177.
- Frances, Z., Villagrasa, C. & Clairand, I., 2010. Simulation of DNA clustering after proton irradiation using an adjusted DBSCAN algorithm. *Computer Methods and Programs in Biomedicine*, Volume 101, pp. 265-270.
- Francis, Z., Villagrasa, C. & Clairand, I., 2011. Simulation of DNA damage clustering after proton irradiation using an adapted DBSCAN algorithm. *Computer Methods and Programs in Biomedicine*, Volume 101, pp. 265-270.
- Frens, G., 1972. Particle size and sol stability in metal colloids. *Colloid and Polymer Science*, Volume 250, pp. 736-741.
- Gannon, C. J. et al., 2008. Intracellular gold nanoparticles enhance non-invasive radiofrequency thermal destruction of human gastrointestinal cancer cells. *Journal of Nanobiotechnology*, Volume 6, pp. 1-9.
- Geetha, R. et al., 2013. Green synthesis of gold nanoparticles and their anticancer activity. *Cancer Nanotechnology*, Volume 4, pp. 91-98.
- Geng, F. et al., 2011. Thio-glucose bound gold nanoparticles enhance radio-cytotoxic targeting of ovarian cancer. *Nanotechnology*, Volume 22, pp. 1-8.
- Girdhani, S., Sachs, R. & Hlatky, L., 2013. Biological Effects of Proton Radiation: What We Know and Don't Know. *Radiation Research*, Volume 179, pp. 257-272.

Gorbsky, G. J., 2014. The spindle checkpoint and chromosome segregation in meiosis. *FEBS Journal*, Volume 282, pp. 2471-2487.

Graves, P. R., Lovly, C. M., Uy, G. L. & Piwnica-Worms, H., 2001. Localization of human Cdc25 is regulated by both nuclear export and 14-3-3 protein binding. *Oncogene*, Volume 20, pp. 1839-1851.

Green, A. A. & Hersam, M. C., 2010. Emerging methods for producing monodisperse graphene dispersions. *Journal of Physical Chemistry Letters*, Volume 1.

Grossman, J. & Mc Neil, S. E., 2012. Nanotechnology in Cancer Medicine. *Physics Today*, Volume 65.

Grün, R., Friedrich, T., Krämer, M. & Scholz, M., 2017. Systematics of relative biological Systematics of relative biological radiation along the spread out Bragg peak: experimental validation of the local effect model. *Physics in Medicine and Biology*, Volume 62, pp. 890-908.

Guo, M. & Hay, B., 1999. Cell proliferation and apoptosis. *Current Opinion in Cell Biology*, Volume 11, pp. 745-752.

Haume, K. et al., 2016. Gold nanoparticles for cancer radiotherapy: a review. *Cancer Nanotechnology*, Volume 7.

Hayat, M. A., 1989. Colloidal gold: principles, methods, and applications. *Academic Press*.

Hillaireau, H. & Couvreur, P., 2009. Nanocarriers'entry into the cell: relevance to drug delivery. *Cellular and Molecular Life Science*, Volume 66, pp. 2873-2896.

Huang, X., El-Sayed, I. H., Qian, W. & El-Sayed, M. A., 2006. Cancer cell imaging and photothermal therapy in the near-infrared region using gold nanorods. *Journal of the American Chemical Society*, Volume 128, pp. 2115-2120.

Huang, X. & El-Sayed, M., 2010. Gold nanoparticles: Optical properties and implementations in cancer diagnosis and photothermal therapy. *Journal of Advanced Research*, Volume 1, pp. 13-28.

Jain, S. et al., 2011. Cell specific radiosensitization by gold nanoparticles at megavoltage radiation energies. *International Journal of Radiation Oncology Biology Physics*, Volume 79, pp. 531-539.

Jamil, B. et al., 2016. Encapsulation of Cardamom Essential oil in Chitosan Nano-composites: In vitro efficacy on Antibiotic -Resistant Bacterial Pathogens and Cytotoxicity studies. *Frontiers in Microbiology*, 7(Article 1580).

Jemal, A. et al., 2009. Cancer Statistics. *A Cancer Journal for Clinicians*, Volume 59, pp. 225-249.

Jeynes, J. C. G. et al., 2014. Investigation of gold nanoparticle radiosensitization mechanisms using a free radical scavenger and protons of different energies. *Physics in Medicine and Biology*, Volume 59, pp. 6431-6443.

Jeynes, J. C. G. et al., 2014. Investigation of gold nanoparticle radiosensitization mechanisms using a free radical scavenger and protons of different energies. *Physics in Medicine and Biology*, Volume 59, pp. 6431-6443.

Joh, D. Y. et al., 2013. Theranostic Gold Nanoparticles Modified for Durable Systemic Circulation Effectively and Safely Enhance the Radiation Therapy of Human Sarcoma Cells and Tumours. *Translational Oncology*, Volume 6, p. 6.

Kakoti, S., Khanna, N. & Laskar, S., 2016. The Current Role of Radiation Therapy for Osteogenic Sarcoma. *Journal of Bone and Soft Tissue Tumours*, Volume 2, pp. 33-35.

Kandikattua, H. . K. et al., 2017. Anti-inflammatory and anti-oxidant effects of Cardamom (*Elettaria repens* (Sonn.) Baill) and its phytochemical analysis by 4D GCXGC TOF-MS. *Biomedicine and Pharmacotherapy*, Volume 91, pp. 191-201.

Khan, A., Rashid, R., Murtaza, G. & Zahra, A., 2014. Gold Nanoparticles: Synthesis and Application in Drug Delivery. *Tropical Journal of Pharmaceutical Research*, Volume 13, pp. 1169-1177.

Kim, J. A., Aberg, C., Salvati, A. & Dawson, K. A., 2012. Role of cell cycle on the cellular uptake and dilution of nanoparticles in a cell population. *Nature Nanotechnology*, Volume 7, pp. 62-68.

Kim, J.-K. et al., 2010. Therapeutic application of metallic nanoparticles combined with particle induced x-ray emission effect. *Nanotechnology*, Volume 21, pp. 1-10.

Klebstov, N. G. & Dykamn, L. A., 2010. Optical properties and biomedical applications of plasmonic nanoparticles. *Journal of Quantitative Spectroscopy and Radiative Transfer*, Volume 111, pp. 1-35.

Kobayashi, H., Watanabe, R. & Choyke, P. L., 2014. Improving Conventional Enhanced Permeability and Retention (EPR) Effects; What Is the Appropriate Target?. *Theranostics*, Volume 4, pp. 81-89.

Kou, L., Sun, J., Zhai, Z. & He, Z., 2013. The endocytosis and intracellular fate of nanomedicines: implications for rational and design. *Asian Journal of Pharmaceutical Sciences*, Volume 8, pp. 1-10.

Kwatra, D., Venugopal, A. & Anant, S., 2013. Nanoparticles in radiation therapy: a summary of various approaches to enhance radiosensitization in cancer. *Translational Cancer Research*, Volume 2, pp. 330-342.

Lal, S. S. & Nayak, P. L., 2012. Green synthesis of gold nanoparticles using various extracts of plants and spices. *Internation Journal of of Science Innovations and Discoveries*, Volume 2, pp. 325-350.

Lechtman, E. et al., 2011. Implicatopns on the clinical scenario of gold nanoparticle radiosensitization in regards to photon energy, nanoparticle size, concentration and location. *Physics in Medicine and Biology*, Volume 56, pp. 4631-4647.

Li , S. et al., 2016. LET-dependent radiosensitization effect of gold nanoparticles for proton irradiation. *Nanotechnology*, Volume 27, pp. 1-9.

Li, G., Park, H. U., Liang, D. & Zhao, R. Y., 2010. Cell Cycle G2/M arrest through an S phase-dependent mechanism by HIV-1 viral protein R. *Retrovirology*, Volume 7.

Li, H., Carter, J. D. & Labean, T. H., 2009. Nanofabrication by DNA self-assembly. *Materialstoday*, Volume 12, pp. 24-32.

Linton, S. s., Sherwood, S. G., Drews, K. C. & Kester, M., 2016. Targeting cancer cells in the tumour microenvironment: oppurtunities and challenges in combinatorial nanomedicine. *WIRES Nanomed Nanobiol*, Volume 8, pp. 208-222.

Lin, Y. et al., 2014. Comparing gold nano-particle enhanced radiotherapy with protons, megavoltage photons and kilovoltage photons: a Monte Carlo simulation. *Physics in Medicine and Biology*, Volume 59, pp. 7675-7689.

Li, S. et al., 2016. LET-dependent radiosensitization effects of gold nanoparticles for proton irradiation. *Nanotechnology*, Volume 27.

- Liu, Z. et al., 2014. Effect of Internalized Gold Nanoparticles with Respect to Cytotoxicity and Invasion Activity in Lung Cancer Cells. *Plos one*, Volume 9.
- Loeffler, J. S. & Durante, M., 2013. Charged particle therapy- optimization, challenges and future directions. *Nature Reviews Clinical Oncology*, May.
- Luzhna, L., Kathiria, P. & Kovalchuk, O., 2013. Micronuclei in genotoxicity assessment: from genetics to epigenetics and beyond. *Frontiers in genetics*, Volume 4, pp. 1-17.
- Mackie, T. R. et al., 2003. Image Guidance for Precise Conformal Radiotherapy. *International Journal of Radiation Oncology, Biology, Physics*, Volume 56, pp. 89-105.
- Malumbres, M. & Barbacid, M., 2009. Cell cycle, CDKs and cancer: a changing paradigm. *Nature Reviews*, Volume 9, pp. 153-166.
- Ma, N.-N. et al., 2017. Shape-Dependent Radiosensitization Effect of Gold Nanostructures in Cancer Radiotherapy: Comparison of Gold Nanoparticles, Nanospikes and Nanorods. *ACS Applied Materials and Interfaces*, Volume 9, pp. 13037-13048.
- Marshall, T. I. et al., 2016. Investigating the Implications of a Variable RBE on Proton Dose Fractionation Across a Clinical Pencil Beam Scanned Spread Out Bragg Peak. *International Journal of Radiation Oncology*, Volume 9, pp. 70-77.
- Michaelidesová, A. et al., 2017. Relative Biological Effectiveness in a proton spread-out Bragg Peak formed in pencil beam scanning mode. *Australasian Physical and Engineering Science in Medicine*, Volume 40, pp. 359-368.
- Mirkin, C. A. et al., 2010. Gold Nanoparticles for Biology and Medicine. *Nanotechnology*, Volume 49, pp. 3280-3294.
- Misra, R., Acharya, S. & Sahoo, S. K., 2010. Cancer nanotechnology: application of nanotechnology in cancer therapy. *Drug Discovery Today*, Volume 15, pp. 842-849.
- Miu, L. & Sprando, R. L., 2010. Application of Nanotechnology in Cosmetics. *Pharmaceutical Research*, Volume 27, pp. 1746-1749.
- Mohan, R., Mahajan, A. & Minsky, B. D., 2013. New Strategies in Radiation: Exploiting the full potential of Protons. *Clinical Cancer Research*, Volume 19, pp. 6338-43.
- Morgan, D. O., 2007. *The Cell Cycle: Principles of Control*. London: New Science Press Ltd.

Morgan, D. O., Fisher, R. P., Espinoza, F. H. & al, e., 1998. Control of eukaryotic cell cycle progression by phosphorylation of cyclin-dependent kinases. *Journal of Cancer Science and Therapy*, Volume 1, pp. S77-83.

Mounthricas, G., Pispas, S. & Kamitsos, E., 2014. Effect of Temperature on the Direct Synthesis of Gold Nanoparticles Mediated by Poly(dimethylaminethyl methacrylate) Homopolymer. *The Journal of Physical Chemistry*, Volume 118, pp. 22754-22759.

Mueller, M., Hobiger, S. & Jungbauer, A., 2010. Anti-inflammatory activity of extracts from fruits, herbs and spices. *Food Chemistry*, Volume 122, pp. 987-996.

Munshi, A., Hobbs, M. & Meyn, R. E., 2005. Clonogenic Cell Survival Assay. *Methods in Molecular Medicine*, Volume 110, pp. 21-28.

Murata, S. et al., 2013. Anti-tumor effects of 1,8 cineole against colon cancer. *Oncology Reports*, Volume 30, pp. 2647-2652.

Murata, S. et al., 2013. Antitumour effect of 1,8 - cineole against colon cancer. *Oncology Reports*, Volume 30, pp. 2647-2652.

nanoComposix, 2012. *Zeta Potential analysis of nanoparticles*. [Online]

Available at: <http://www.Nanocomposix.com>

[Accessed 20 05 2017].

Newhauser, W. D. & Zhang, R., 2015. The physics of proton therapy. *Physics in Medicine & Biology*, Volume 60, pp. R155-R209.

Newhauser, W. D. & Zhang, R., 2015. The Physics of Proton Therapy. *Phys. Med. Biol.*, 60(8), pp. R155-209.

Nguyen, T. D. T., Pitchaimani, A. & Aryal, S., 2016. Engineered Nanomedicine with Alendronic Acid Corona Improves Targeting to Osteosarcoma. *Scientific Reports*, Volume 6.

Nobbmann, U., 2014. *Materials Talk*. [Online]

Available at: <http://www.materials-talks.com>

[Accessed 5 10 2017].

Nune , S. K. et al., 2009. Green Nanotechnology from Tea: Phytochemicals in Tea as Building Blocks for Production of Biocompatible Gold Nanoparticles. *Journal of Materials Chemistry*, Volume 19, pp. 2912-2020.

Nunez, R., 2001. DNA Measurement and Cell Cycle Analysis by Flow Cytometry. *Current issues in Molecular biology*, Volume 3, pp. 67-70.

O'Connor, C. M. & Adams, J. U., 2010. *Essentials of Cell Biology*. Cambridge, MA: NPG Education.

Ogawa, Y., Takahashi, T., Kobayashi, T. & al, e., 2003. Mechanism of apoptotic resistance of Osteosarcoma cell line, HS-Os-1, against irradiation. *International Journal of Molecular Medicine*, Volume 12, pp. 453-458.

Osaki, F. et al., 2004. A quantum dot conjugated sugar ball and its cellular uptake. On the side effects of endocytosis in the subviral region. *Journal of the American Chemical Society*, Volume 126, pp. 6520-6521.

Otani, K. et al., 2016. Cell-cycle-controlled radiation therapy was effective for treating a murine malignant melanoma cell line in vitro and in vivo. *Scientific Reports*, Volume 6, pp. 1-7.

Paganetti, H., 2012. Range uncertainties in proton therapy and the role of Monte Carlo simulations. *Physics in Medicine and Biology*, Volume 57, pp. R99-R117.

Paganetti, H. et al., 2002. Relative Biological Effectiveness values for proton beam therapy. *International Journal of Radiation Biology and Physics*, Volume 53, pp. 407-421.

Page, K. et al., 2004. Direct observation of the structure of gold nanoparticles by total scattering powder neutron diffraction. *Chemical Physics Letters*, Volume 393, pp. 385-388.

Pan, Y. et al., 2014. Inhibition effects of gold nanoparticles on proliferation and migration in hepatic carcinoma-conditioned HUVECs. *Bioorganic & Medicinal Chemistry Letters* 24, pp. 679-684.

Pandey, R. & Ahmad, Z., 2011. Nanomedicine and experimental tuberculosis: facts, flaws and future. *Nanomedicine*, Volume 7, pp. 259-272.

Pan, Y. et al., 2014. Inhibition effects of gold nanoparticles on proliferation and migration in hepatic-carcinoma conditioned HUVECs. *Bioorganic and Medicinal Chemistry Letters*, Volume 24, pp. 679-684.

Patra, H. K. et al., 2007. Cell selective response to gold nanoparticles. *Nanomedicine: Nanotechnology, Biology and Medicine*, Volume 3, pp. 111-119.

- Pattanayak, M., Muralikrishnan, T. & Nayak, P. L., 2013. Green synthesis of gold nanoparticles using *Elattaria cardamom* (ELAICHI) aqueous extract. *World Journal of Nanoscience and Technology*, Volume 2, pp. 52-58.
- Paul, P., Unnikrishnan, N. K. & Naggapa, N., 2011. Phytochemicals as radioprotective agents- A Review. *Indian Journal of Natural Products and Resources*, Volume 2, pp. 137-150.
- Pavlin, M. & Bregar, V. B., 2012. Stability of nanoparticle suspensions in biologically relevant media. *Digest Journal of Nanomaterials and Biostructures*, Volume 7, pp. 1389-14000.
- Pawlik, T. M. & Keyomarsi, K., 2004. Role of the cell cycle in mediating sensitivity to radiotherapy. *International Journal of Radiation Oncology Biology Physics*, Volume 59, pp. 924-942.
- Pesin, J. A. & Orr-Weaver, T. L., 2008. Regulation of APC/C activators in mitosis and meiosis. *Annual Reviews in Cell and Development Biology*, Volume 45, pp. 475-499.
- Polf, J. C. et al., 2011. Enhance relative biological effectiveness of proton radiotherapy in tumor cells with internalized gold nanoparticles. *Applied Physics Letters*, Volume 98.
- Porcel, E. et al., 2010. Platinum nanoparticles: a promising material for future cancer therapy. *Nanotechnology*, Volume 21.
- Raghunandan, D. et al., 2011. Anti-cancer studies of noble metal nanoparticles synthesized using different plant extracts. *Cancer Nanotechnology*, Volume 2, pp. 57-65.
- Rajan, A., Rajan, A. R. & Philip, D., 2017. *Elettaria cardamomum* seed mediated rapid synthesis of gold nanoparticles and its biological activities. *Open Nano*, pp. 1-8.
- Retif, P. et al., 2015. Nanoparticles for Radiation Therapy Enhancement: The Key Parameters. *Theranostics*, Volume 5, pp. 1030-1044.
- Roa, W. et al., 2009. Gold nanoparticle sensitize radiotherapy of prostate cancer cells by regulation of the cell cycle. *Nanotechnology*, Volume 20, pp. 1-9.
- Rosa, S. et al., 2017. Biological mechanisms of gold nanoparticle radiosensitization. *Cancer Nanotechnology*, Volume 8.

- Saberi, A. et al., 2017. Gold nanoparticles in combination with megavoltage radiation energy increased radiosensitization and apoptosis in colon cancer HT-29 cells. *International Journal of Radiation Biology*, Volume 93, p. 315–323.
- Sahay, G., Alakhova, D. Y. & Kabanov, A. V., 2010. Endocytosis of nanomedicines. *Journal of Controlled Release*, Volume 145, pp. 182-195.
- Salata, O. V., 2004. Applications of nanoparticles in biology and medicine. *Journal of Nanobiotechnology*, Volume 2.
- Sancar, A., Lindsey-Boltz, L. A., Unsal-Kacmaz, K. & Linn, S., 2004. Molecular mechanisms of mammalian DNA repair and DNA damage checkpoints. *Annual Reviews in Biochemistry*, Volume 73, pp. 39-85.
- Sanchez, Y. et al., 1997. Conservation of the the Chk1 checkpoint pathway in mammals: linkage of DNA damage to Cdk regulation through Cdc25. *EMBO Journal*, Volume 16, pp. 545-554.
- Sanna, V., Pala, N. & Sechi, M., 2014. Targeted therapy using nanotechnology: Focus on cancer. *International Journal of Nanomedicine*, Volume 9.
- Santhoskumar, J., Rajeshkumar, S. & Venkat Kumar, S., 2011. Phyto-assisted synthesis, characterization and applications of gold nanoparticles- A review. *Biochemistry and Biophysics Reports*, pp. 46-57.
- Scalliete, P. & Gueulette, J., 2017. *Radiobiological Characterization of Clinical Proton and Carbon ion beams.*, Geneva: CERN.
- Shankar, S. S., Rai, A., Ahmad, A. & Sastry, M., 2004. *Journal of Colloidal Interface Science*, Volume 275.
- Sharma, N., Bhatt, G. & Khothiyal, P., 2015. Gold Nanoparticles synthesis, properties, and forthcoming applications – A review. *Indian Journal of Pharmaceutical and Biological Research*, Volume 3, pp. 13-27.
- Sharma, S., Sharma, J. & Kaur, G., 2011. Therapeutic uses of Cardamom. *International Journal of Drug Formulation and Pharmacy*, Volume 2.

Shukla, B., Bansal, V. & Chaudhary, M. a., 2005. Biocompatibility of gold nanoparticles and their endocytic fate inside cellular compartment: a microscopic view. *Langmuir*, Volume 21, pp. 10644-54.

Singh, A. K. & Srivastava, O. N., 2015. One-Step Green Synthesis of Gold Nanoparticles Using Black Cardamom and Effect of pH on Its Synthesis. *Nanoscale Research Letters*, Volume 10.

Sinha, R., Kim, G. J., Nie, S. & Shin, D. M., 2009. Nanotechnology in cancer therapeutics: bioconjugated nanoparticles for drug delivery. *Molecular Cancer Therapeutics*, Volume 5, pp. 1909-1917.

Sonoda, E. et al., 2006. Differential usage of non-homologous end-joining and homologous recombination in double strand break repair. *DNA Repair*, Volume 5, pp. 1021-1029.

Soshnikova, V. et al., 2017. Cardamom fruits as a green resource for facile synthesis of gold and silver nanoparticles and their biological applications. *Artificial cells, Nanomedicine and Biotechnology*.

Steichen, S. D., Caldorera-Moore, M. & Peppas, N. A., 2013. A review of current nanoparticle and targeting moieties for the delivery of cancer therapeutics. *European Journal of Pharmaceutical Sciences*, Volume 48, pp. 416-427.

Stracker, T. H., Usui, T. & Petrini, J. H. J., 2009. Taking time to make to make important decisions: The checkpoint effector kinases Chk1 and Chk2 and the DNA damage response. *DNA Repair*, Volume 4, pp. 1047-1054.

Sudakin, V., Chan, G. K. & Yen, T. J., 2001. Checkpoint inhibition of the APC/C in HeLa cells mediated by a complex of BUBR1, BUB3, CDC20, and MAD2. *Journal of Cell Biology*, Volume 154, pp. 925-936.

Sui, L. et al., 2013. Clustered DNA damage induced by proton radiation damage in plasmid DNA. *Chinese Science Bulletin*, Volume 58, pp. 3217-3223.

Sujitha, M. V. & Kannan, S., 2013. Green synthesis of gold nanoparticles using Citrus fruits (Citrus limon, Citrus reticulata, Citrus sinensis) aqueous extract and its characterization. *Spectrochimica Acta Part A*, Volume 102, pp. 15-23.

Su, X.-Y., Liu, P.-D., Wu, H. & Gu, N., 2014. Enhancement of radiosensitization by metal-based nanoparticles in cancer radiation therapy. *Cancer Biology & Medicine*, Volume 11, pp. 86-91.

Svaarsand, L. O., Gomer, C. J. & Morinelli, E., 1990. On the physical induced rationale of laser induced hyperthermia. *Lasers and Medical Science*, Volume 5, pp. 121-127.

Taggart, L. E. et al., 2014. The role of mitochondrial function in gold nanoparticle mediated radiosensitisation. *Cancer Nanotechnology*, Volume 5, pp. 1-12.

Takeda, D. Y. & Dutta, A., 2005. DNA replication and progression through S phase. *Oncogene*, Volume 24, pp. 2827-2843.

Tamarkin, L. & Kingston, D. G., 2017. Exposing the tumor microenvironment: how gold nanoparticles enhance and refine drug delivery. *Therapeutic Delivery*, Volume 8, pp. 363-366.

Tanev, S., 2009. Flow Cytometry with Gold Nanoparticles and their Clusters as scattering Contrast Agents: FDTD Simulation of Light-Cell Interaction. *Journal of Biophotonics*, Volume 2, pp. 505-520.

Thakkar, K. N., Mhatre, S. S. & Parikh, P. Y., 2010. Biological synthesis of metallic nanoparticles. *Nanomedicine*, Volume 2, pp. 257-262.

Tokuyama, Y. et al., 2015. Role of isolated and clustered DNA damage and the post-irradiating repair process in the effects of heavy ion beam radiation. *Journal of Radiation Research*, Volume 56, pp. 446-455.

Tommasino, F. & Durante, M., 2015. Proton Radiobiology. *Cancers*, Volume 7, pp. 353-381.

Tran, M., DePenning, R., Turner, M. & Padalkar, S., 2016. Effect of citrate ratio and temperature on gold nanoparticle size and morphology. *Materials Research Express*, Volume 3.

Tran, M., DePenning, R., Turner, M. & Padalkar, S., 2016. Effect of citrate ratio and temperature on gold nanoparticle size and morphology. *Materials Research Express*, Volume 3.

Treuel, L. et al., 2014. Physicochemical characterization of nanoparticles and their behaviour in the biological environment. *Journal of Physical Chemistry*, Volume 16, pp. 15053-15067.

Tully, B. D. et al., 2000. Effects of arsenic, cadmium, chromium, and lead on gene expression regulated by a battery of 13 different promoters in recombinant HepG2 cells.. *Toxicology and Applied Pharmacology*, 168(79-90).

Turkevich, J., Stevenson, P. C. & Hiller, J., 1951. A study of the nucleation and growth processes in the synthesis of colloidal gold. *Discussion of the Faraday Society*, Volume 11.

Valdivieso, M., Kujawa, A. M., Jones, T. & Baker, L. H., 2012. Cancer survivors in the United States: a review of the literature and a call to action. *International journal of medical sciences*, Volume 9, pp. 163-173.

Vega-Avila, E. & Pugsley, M. K., 2011. An Overview of Colorimetric Assay Methods Used to Assess Survival or Proliferation of Mammalian cells. *Proceedings of the Western Pharmacology Society*, Volume 54, pp. 10-14.

Verkhovtsev, A. V., Korol, A. V. & Solov'yov, A. V., 2015a. Electron production by sensitizing gold nanoparticles irradiated by fast ions. *Journal of Physical Chemistry C*, Volume 119, pp. 11000-11013.

Verkhovtsev, A. V., Korol, A. V. & Solov'yov, A. V., 2015b. Revealing the mechanism of the low-energy electron yield enhancement from sensitizing nanoparticles. *Physical Review Letters*, Volume 114.

Vernimmen, F. J. A. I. & Slabbert, J., 2010. Assessment of the  $\alpha/\beta$  ratios for arteriovenous malformations, meningiomas, acoustic neuromas, and the optic chiasma. *International Journal of Radiation Biology*, Volume 86, pp. 486-498.

Vernimmen, F. J. A. I. et al., 2005. Stereotactic proton beam therapy for intercranial arteriovenous malformations. *International Journal of Radiation Biology and Physics*, Volume 62, pp. 44-52.

Villagrasa, C. et al., 2014. RBE-LET relationship for proton and alpha irradiations studied with a nanodosimetric approach. *Radiation Protection Dosimetry*, Volume 161, pp. 449-453.

Vincenzo, A. et al., 2017. Surface plasmon resonance in gold nanoparticles: a review. *Journal of Physics: Condensed Matter*, Volume 29.

Vral, A., Fenech, M. & Thierens, H., 2011. The micronucleus assay as a biological dosimeter of in vivo ionising radiation exposure. *Mutagenesis*, Volume 26, pp. 11-17.

Walzlein, C., Scifoni, E., Kramer, M. & Durante, M., 2014. Simulations of dose enhancement by heavy atin nanoparticles irradiated by protons. *Physics Medicine & Biology*, Volume 59, pp. 1441-1458.

Wilson, G. D. & Marples, B., 2007. Flow Cytometry in Radiation Research: Past, Present and Future. *Radiation Research*, Volume 168, pp. 391-403.

Wurm, F. M., 2004. Production of recombinant protein therapeutics in cultivated mammalian cells. *Nature Biotechnology*, Volume 22, pp. 1393-1398.

Yao, C. et al., 2016. Gold Nanoparticle Mediated Phototherapy for Cancer. *Journal of Nanomaterials*, pp. 1-29.

Yin, H., Liao, L. & Fang, J., 2014. Enhanced Permeability and Retention (EPR) Based on Tumor Targeting : The Concept, Application and Prospect. *JSM Clinical Oncology and Research*, Volume 2, p. 1010.

Zayed, M. F. & Eisa, W. H., 2014. Eisa, Phoenix dactylifera L. leaf extract phytosynthesized gold nanoparticles; Control synthesis and catalytic activity. *Spectrochimca Acta Part A: Mol. Biol. Spectros*, Volume 121, pp. 238-244.

Zhang, S., Gao, H. & Bao, G., 2015. Physical Principles of Nanoparticle Endocytosis. *ACS Nano*, Volume 9, pp. 8655-8671.

Zhang, X. et al., 2008. Enhanced radiation sensitivity in Prostate cancer by gold-nanoparticles. *Clinical and Investigative Medicine*, Volume 31, pp. 160-167.

Zhou, B.-B. S. & Elledge, S. J., 2000. The DNA damage response: putting checkpoints into perspective. *Nature*, Volume 408, pp. 433-439.

Zimbone, M. et al., 2011. Dynamic light scattering and UV-vis spectroscopy of gold nanoparticles solution. *Materials Letters*, Volume 65, pp. 2906-2909.

---

## CHAPTER 5: ADDENDUM

---

### 5.1 AuNP images

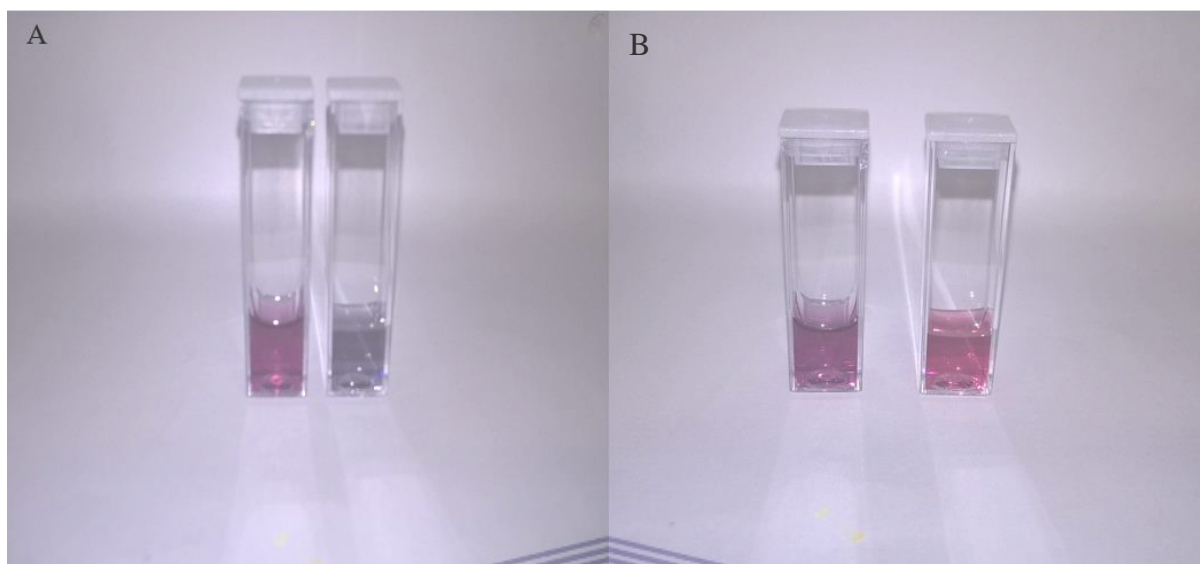


**Figure 5.1: Photographic images depicting the difference in colour of AuNPs synthesized with different temperatures. A) AuNPs synthesized at 55 ° C and RT B) AuNP synthesized at 55 ° C and 85 ° C.**

### 5.2 UV-spectral curves

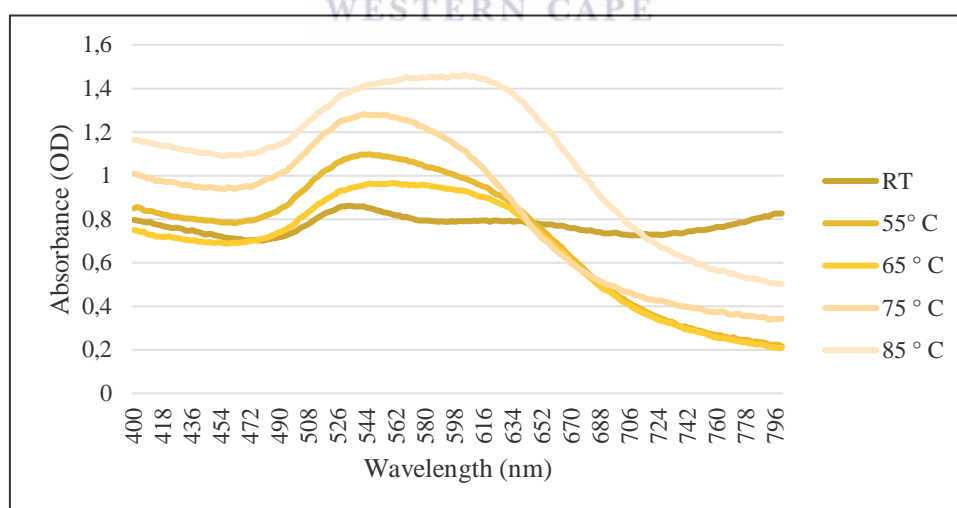


**Figure 5.2: Temperature dependent synthesis of Car-AuNPs with extract prepared from whole cardamom seeds.**

Flat regions in lieu of defined SPR peaks indicate particle agglomeration and instability. The flattened SPR seen opposes the effect exhibited in Car-AuNPs synthesized from crushed seed extract.

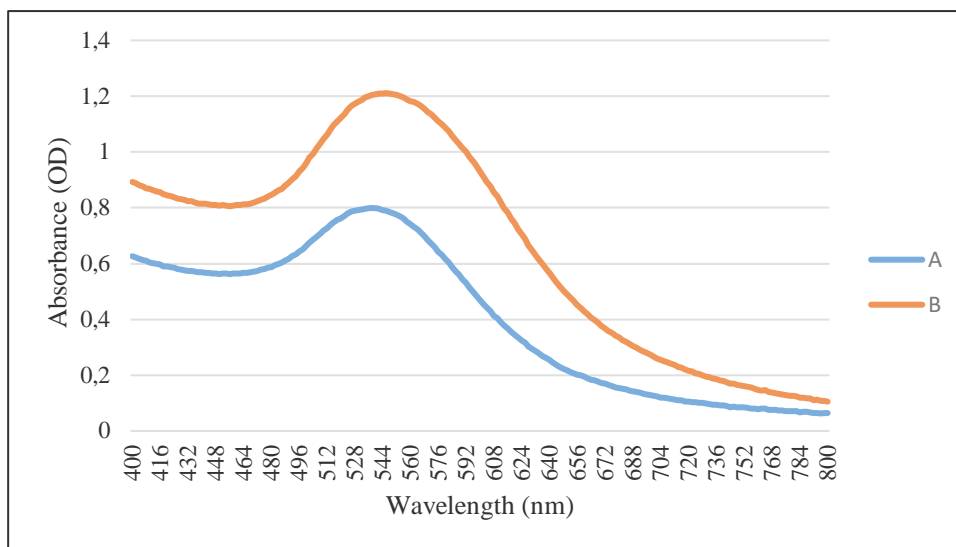


**Figure 5.3: The effect of H<sub>AuCl</sub> quantity on AuNP quality. A)** AuNP synthesized as described in section 2.1.3.1. **B)** AuNP synthesis 200μl H<sub>AuCl</sub> instead of 300 μl.

Reduction of H<sub>AuCl</sub> quantity resulted in longer SPR bands indicated increased AuNP size. The SPR bandwidth increased from a λ<sub>max</sub> of 538 to λ<sub>max</sub> of 548



### 5.3 DLS and Zeta Potential

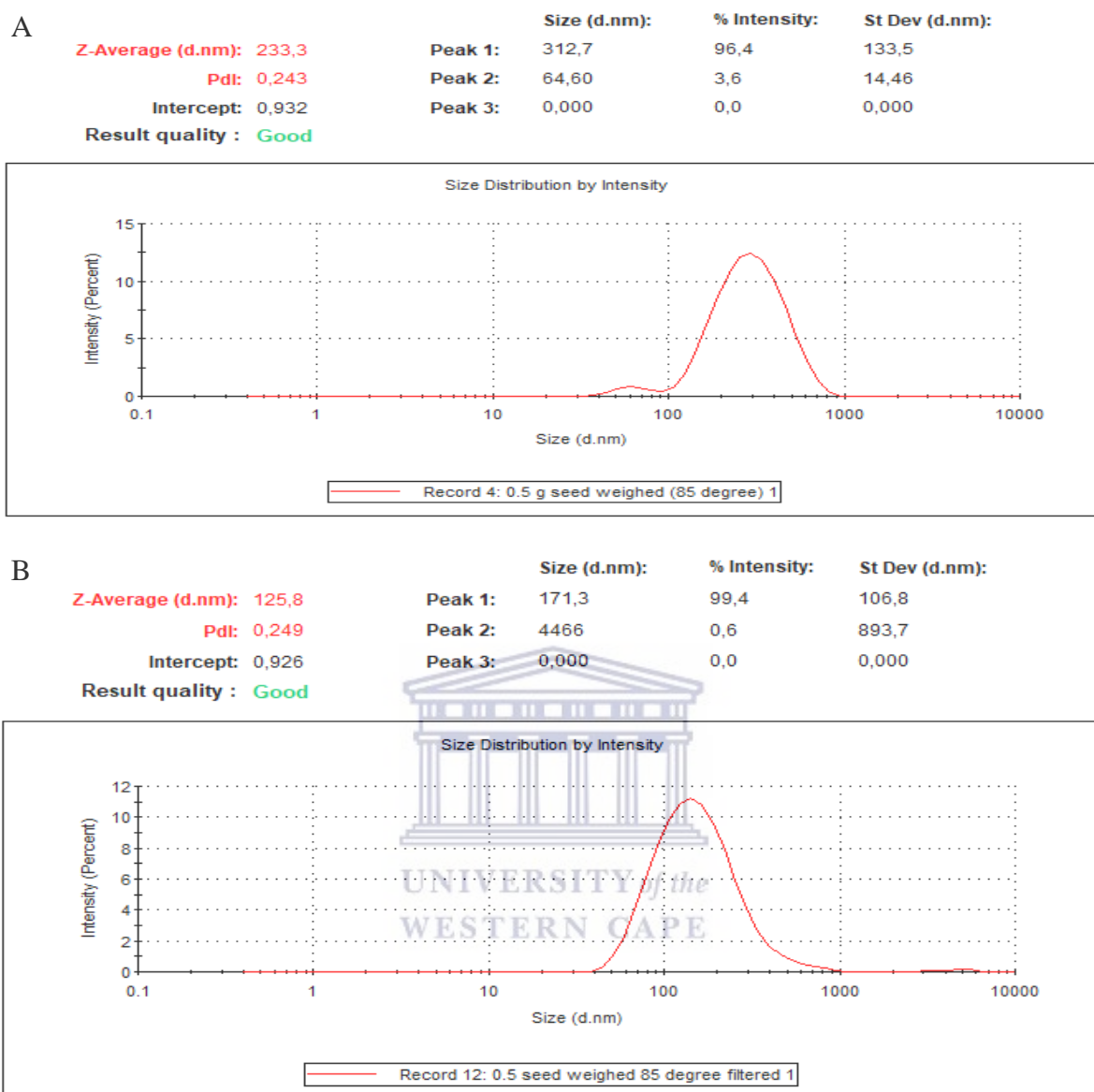


**Figure 5.4:** Size distribution curves prior to and after filtering the AuNPs. The size of the AuNPs were largely reduced and the proportion of AuNPs present within the second peak reduced from 3.6% to 0.6%. Additionally the first peak proved a narrower size distribution of AuNPS with 99.4% of AuNPs falling within the lower size range depicted. The large AuNP read could simply be an artifact or debris.

**Table 5.1:** The stability of Car-AuNPs over time. Car-AuNP stability in storage was measured by Zeta Potential and DLS over time.

Time of characterization	DLS	Zeta Potential	PDI
Same day as synthesis	262.6 d.nm	-17.4 mV	0.247
2 weeks post synthesis	262 d.nm	-19.7 mV	0.258
4 weeks post synthesis	256 d.nm	-17.5 mV	0.211

## 5.4 AuNP uptake

**Table 5.2** AuNP uptake efficiency determined using mean side scatter obtained from flow cytometry

Sample Non-IR	Mean SSC	Uptake efficiency
Control	1 014 808,38	
Car-AuNP	1 272 961,06	1,25
Control	1 349 196,07	
5 nm AuNP	1 110 363,04	0,82
Control	1 409 500,86	
10 nm AuNP	1 803 518,81	1,28
Control	1 416 769,18	
50 nm AuNP	1 417 853,31	1,00



## 5.5 Statistical analysis of Mitotic index

Data	MI
Factor codes	Samples
Sample size	30

**Levene's Test for Equality of Variances**

Levene statistic	1.325
DF 1	9
DF 2	20
Significance level	P = 0.285

**ANOVA**

Source of variation	Sum of squares	DF	Mean square
Between groups (influence factor)	206.5213	9	22.9468
Within groups (other fluctuations)	31.2267	20	1.5613
Total	237.7480	29	

F-ratio	14.697
Significance level	P < 0.001

**Student-Newman-Keuls test for all pairwise comparisons**

Factor	n	Mean	Different (P<0.05) from factor nr
(1) 1	3	5.9667	(2)(3)(4)(9)
(2) 2	3	2.6667	(1)(3)(4)(5)(6)(7)(8)(9)(10)
(3) 3	3	11.3667	(1)(2)(5)(6)(7)(8)(10)
(4) 4	3	12.1333	(1)(2)(5)(6)(7)(8)(10)
(5) 5	3	8.7667	(2)(3)(4)
(6) 6	3	6.0000	(2)(3)(4)(9)
(7) 7	3	7.7333	(2)(3)(4)
(8) 8	3	8.4000	(2)(3)(4)
(9) 9	3	9.6667	(1)(2)(6)
(10) 10	3	7.5000	(2)(3)(4)

**Figure 5.5:** Analysis of Variance and Student Newman Keuls data showing the cumulative p value of the data set (p<0.001) and statistically significant differences between all means.

## 5.6 Reference data of CSA

**Table 5.3.:** The cell survival clonogenic assay performed with two concentrations of 10 AuNPs after a 24 hour pre-incubation period.

Sample	# Cells plated	# Colonies counted	Mean	% PE
Control	200	179,170,168,169	171	85
10 $\mu\text{g/ml}$ AuNP	200	190,203,204,180	194	97
5 $\mu\text{g/ml}$ AuNP	200	256,278,244,247	256	128

Incubation with AuNPs at low concentrations for 24 hours and a subsequent 6 day growth period revealed that colony formation was minimally affected by the presence of AuNPs *in vitro* as indicated by the resultant plating efficiencies (PE).

**Table 5.4:** The cell survival clonogenic assay performed with two concentrations of 10 nm AuNPs and 8 Gy of  $\text{C}^{60}$  radiation.

Sample	# Cells plated	# Colonies counted	Mean	% PE	Surviving fractions
Control IR	10 000	168,175,170,186	174	1.74	0.01
10 $\mu\text{g/ml}$ AuNP	10 000	179,186,174,212	187	1.87	0.01
5 $\mu\text{g/ml}$ AuNP	10 000	191,160,175,181	176	1.76	0.01

Establishing PEs for cells treated with AuNPs allowed for the approximation of dilution routes required to obtain appropriate cell quantities for proton experiments.

## 5.7 Data distribution curves for chromosomal damage analysis

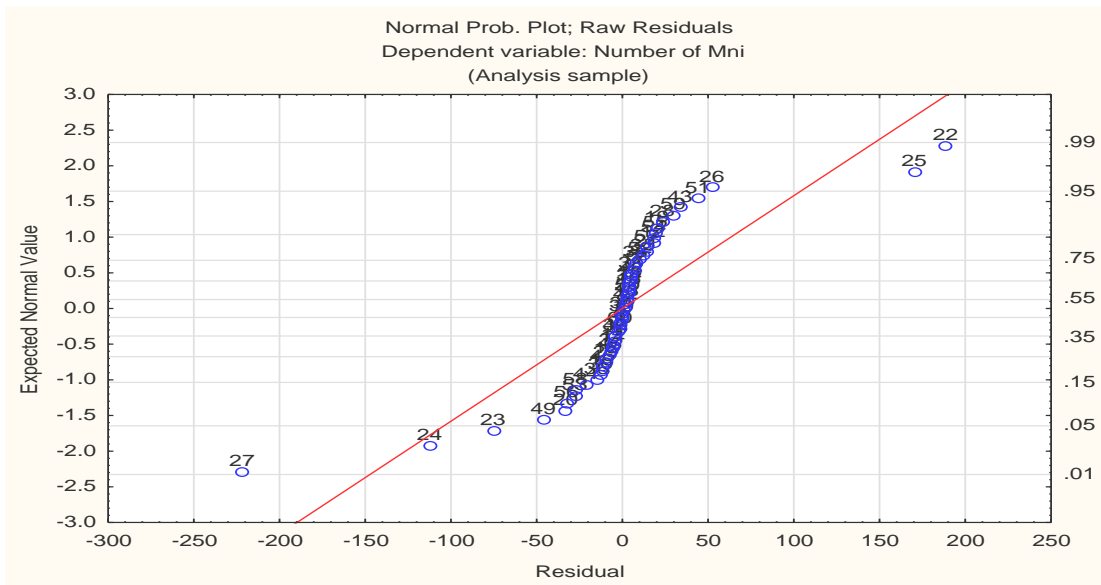


**Figure 5.6:** Distribution curves for MNI data of 5, 10 and Car-AuNPs. Despite a few outliers, the data was relatively normally distributed

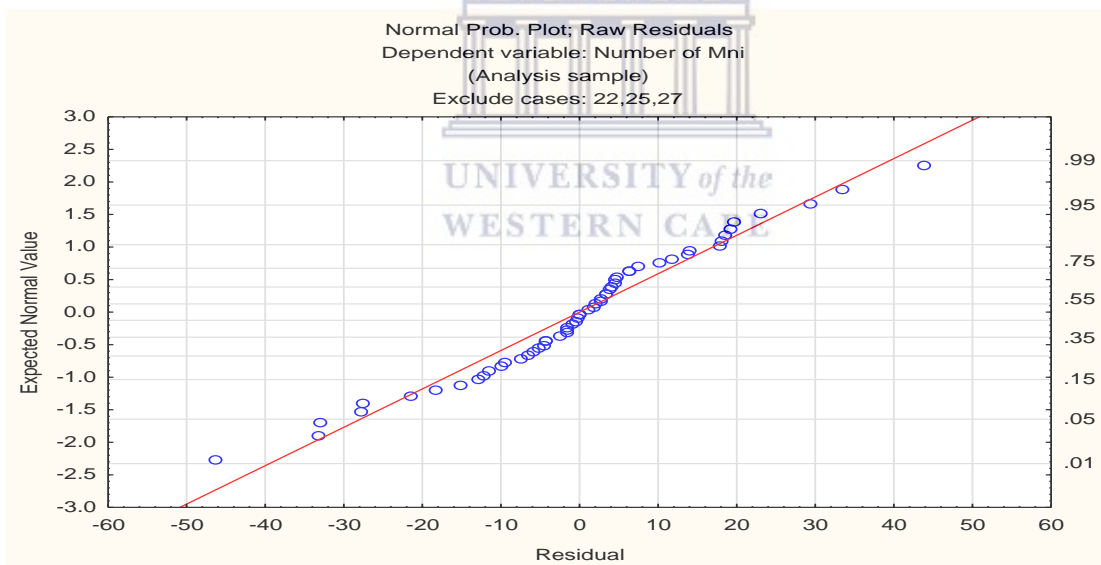


**Figure 5.7:** Distribution curves for MNI data of 50 nm AuNPs.

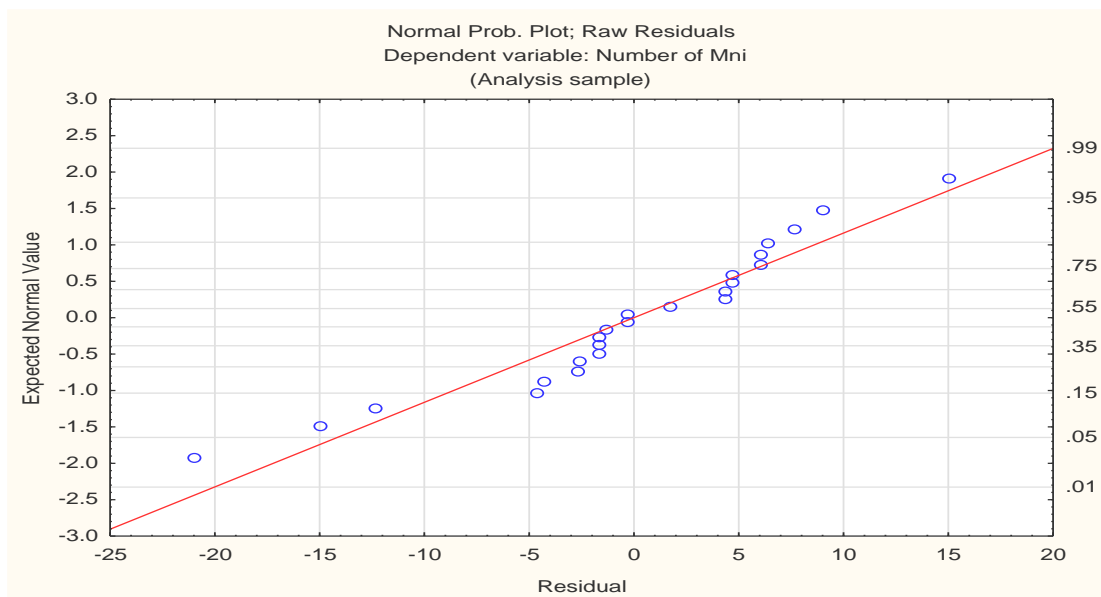


**Figure 5.8:** Distribution data of the MNi assay performed after a 24 hour incubation period with 50 nm AuNPs. The MNi data was normally distributed.

### 5.8 Dose enhancement values (MNI)

**Table 5.5.** Calculated DEFs for CHO cells treated with 5nm, 10nm and Car-AuNPs for 4 hours followed by proton radiation.

SOBP condition	Dose	Unity
5 nm AuNP Entrance SOBP	2	0,725543
5 nm AuNP Middle SOBP	2	1,273187
5 nm AuNP Distal SOBP	2	1,049664
10 nm AuNP Entrance SOBP	2	1,205371
10 nm AuNP middle SOBP	2	1,395122
10 nm AuNP Distal SOBP	2	1,067797
Car-AUNP Entrance SOBP	2	0,945634
Car-AUNP Middle SOBP	2	1,293245
Car-AUNP Distal SOBP	2	0,728745

**Table 5.6** Dose enhancement values expressed after a 4 h incubation period of AuNPs and treatment with protons (2 Gy and 4 Gy)

SOBP position condition	Dose	Unity
AuNP Entrance Reference	2	1,038226
AuNP Proximal SOBP	2	1,223473
AuNP Middle SOBP	2	1,015355
AuNP Distal SOBP	2	1,12069
AuNP 80 % Dmax	2	1,027879
AuNP Entrance Reference	4	1,173193
AuNP Proximal SOBP	4	1,442308
AuNP Middle SOBP	4	0,881412
AuNP 80 % Dmax	4	0,953923

**Table 5.7:** Dose enhancement values expressed after a 24 hour incubation period of 50 nm AuNPs and treatment with protons

SOBP position	Dose	Unity
AuNP Entrance SOBP	2	0,730594
AuNP Proximal SOBP	2	0,98254
AuNP Middle SOBP	2	1,124046



## 5.9 RCGG values (cell cycle kinetics)

**Table 5.8:** RCGG values determined for Car-AuNP exposed cells

Sample	% S-phase	% G2/M phase	RCGG
Control Non-IR	17,94%	31,16%	1,74
Control Entrance Plateau	16,63%	41,86%	2,52
Car-AuNP Non-IR	15,55%	29,43%	1,89
Car-AuNP Plateau	16,96%	32,20%	1,90

**Table 5.9:** RCGG values determined for cells exposed to 5 nm AuNPs, protons, and 5 nm AuNPs in combination with protons

Sample	% S-phase	% G2/M phase	RCGG
Control Non-IR	9,17%	31,92%	3,48
Control Entrance Plateau	26,18%	20,66%	0,79
Control Proximal	23,74%	19,70%	0,83
Control Middle	22,03%	20,54%	0,93
Control Distal	22,20%	21,58%	0,97
5 nm Non-IR	48,96%	37,27%	0,76
5 nm Entrance Plateau	23,04%	20,09%	0,87
5 nm Proximal	22,51%	49,15%	2,18
5 nm Middle	24,59%	47,18%	1,92
5 nm Distal	21,03%	48,78%	2,32

UNIVERSITY OF  
WESTERN CAPE

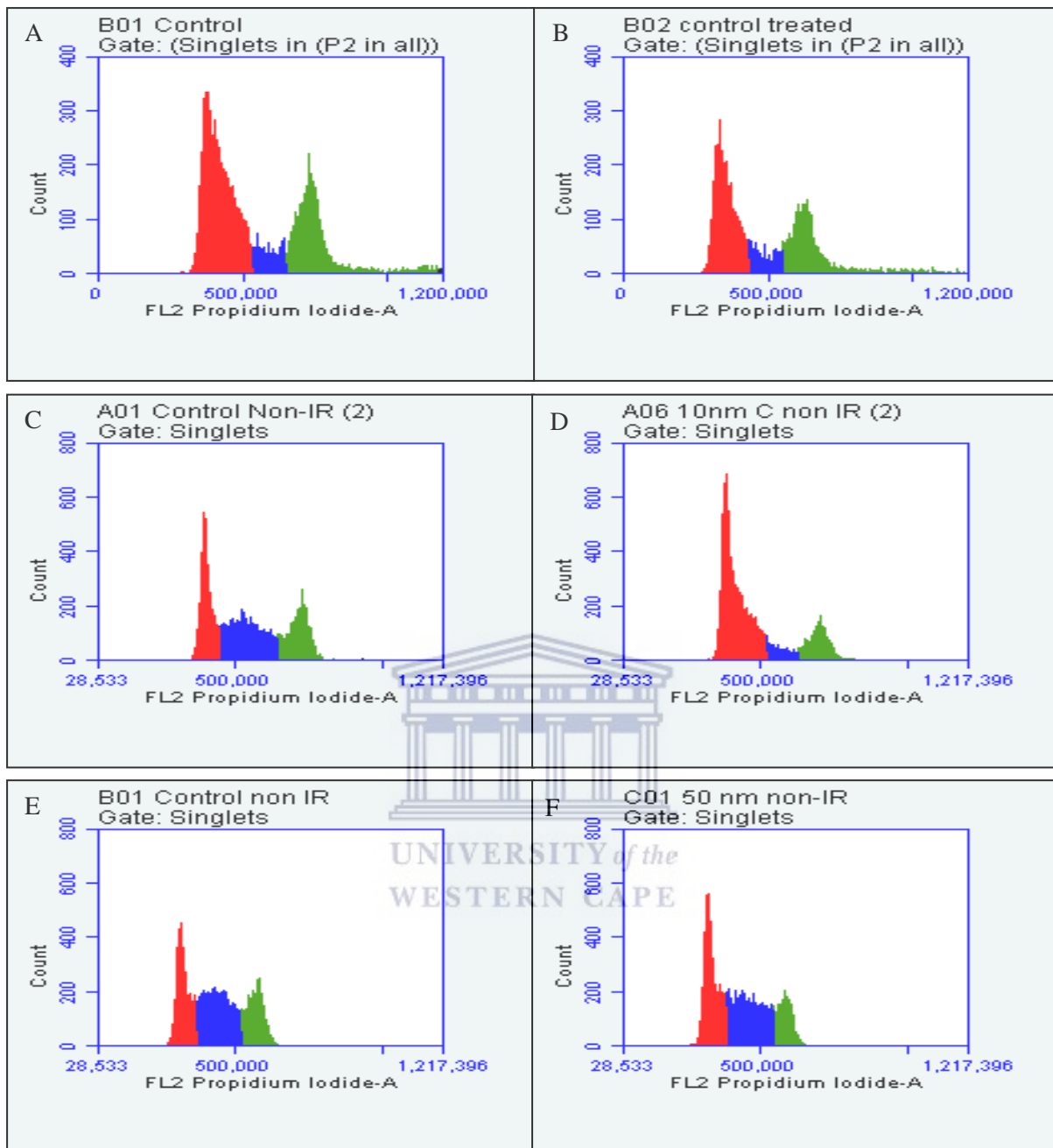
**Table 5.10:** RCGG values determined for cells exposed to 10 nm AuNPs, protons and 10 nm AuNPs in combination with protons

Sample	% S-phase	% G2/M phase	RCGG
Control Non-IR	37,63%	26,81%	0,71
Control Entrance Plateau	11,48%	58,45%	5,09
Control Proximal	9,98%	60,29%	6,04
Control Middle	8,27%	61,25%	7,41
Control Distal	15,01%	68,98%	4,60
10 nm Non-IR	8,12%	19,04%	2,34
10 nm Entrance Reference	6,83%	54,30%	7,95
10 nm Proximal	10,00%	55,16%	5,52
10 nm Middle	9,19%	53,24%	5,79
10 nm Distal	7,33%	52,23%	7,13

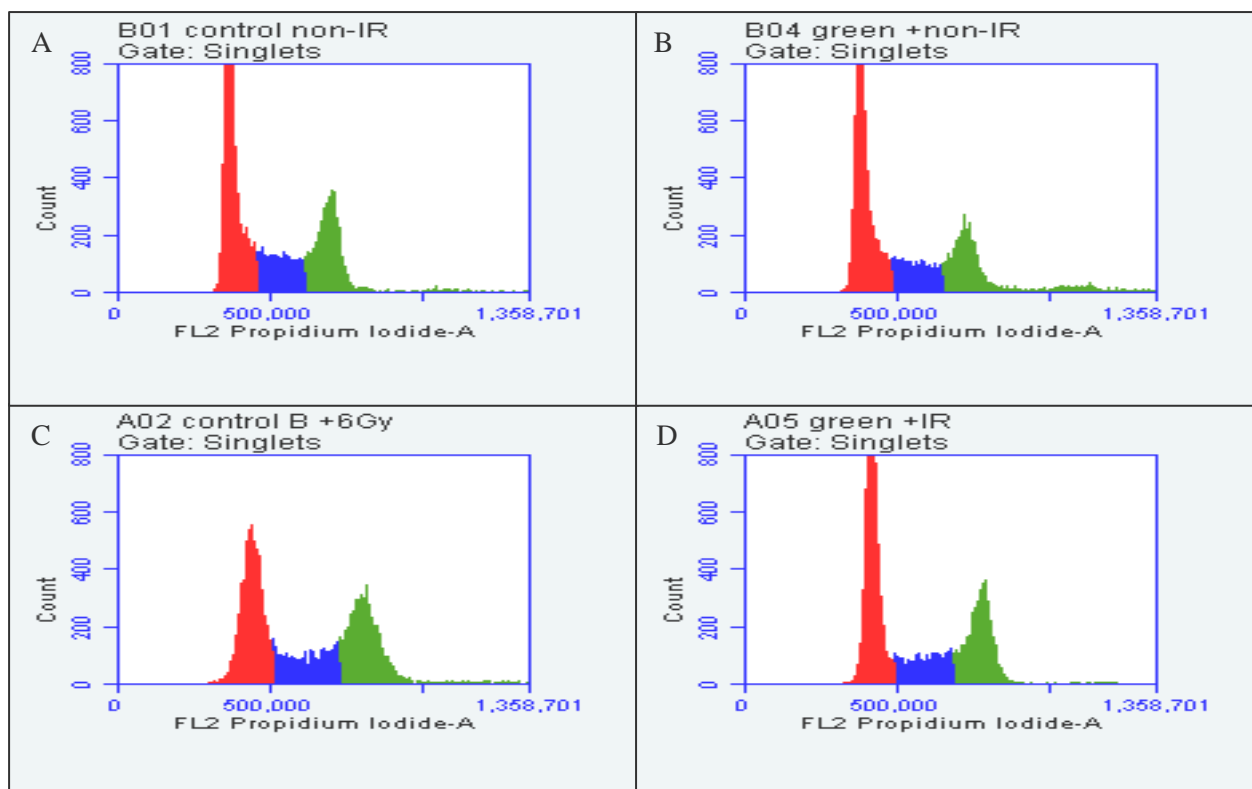
**Table 5.11:** RCGG values calculated for cells exposed to 50 nm AuNPs, protons and 50 nm AuNPs in combination with protons

Sample	% S-phase	% G2/M phase	RCGG
Control Non-IR	40,88%	25,49%	0,62
Control Entrance Plateau	14,87%	39,47%	2,65
Control Proximal	28,86%	43,14%	1,49
Control Middle	15,87%	39,23%	2,47
Control Distal	18,29%	60,25%	3,29
50 nm Non-IR	39,39%	18,03%	0,46
50 nm Entrance Reference	28,91%	36,33%	1,26
50 nm Proximal	28,74%	34,06%	1,19
50 nm Middle	30,09%	38,17%	1,27
50 nm Distal	16,35%	64,88%	3,97

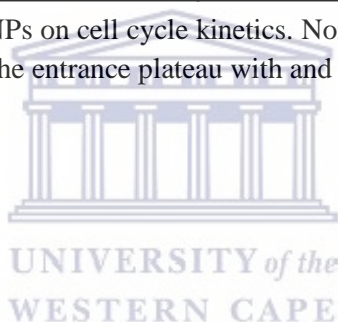
## 5.10 Cell cycle kinetics



**Figure 5.9:** Non-irradiated controls of CHO cells. Negative controls are depicted on the left whilst sample **B)** contains 50 ug/ml of 5 nm AuNPs **D)** contains 50 ug/ml of 10 nm and **F)** contains 10 ug/ml of 50 nm AuNP images on subsequent pages depict these conditions with the addition of 6 Gy of protons at different positions along the proton beam.



**Figure 5.10:** The effect of Car-AUNPs on cell cycle kinetics. Non-Irradiated controls are depicted in A) and B) whilst irradiated samples in the entrance plateau with and without Car-AuNPs are depicted in C) and D).



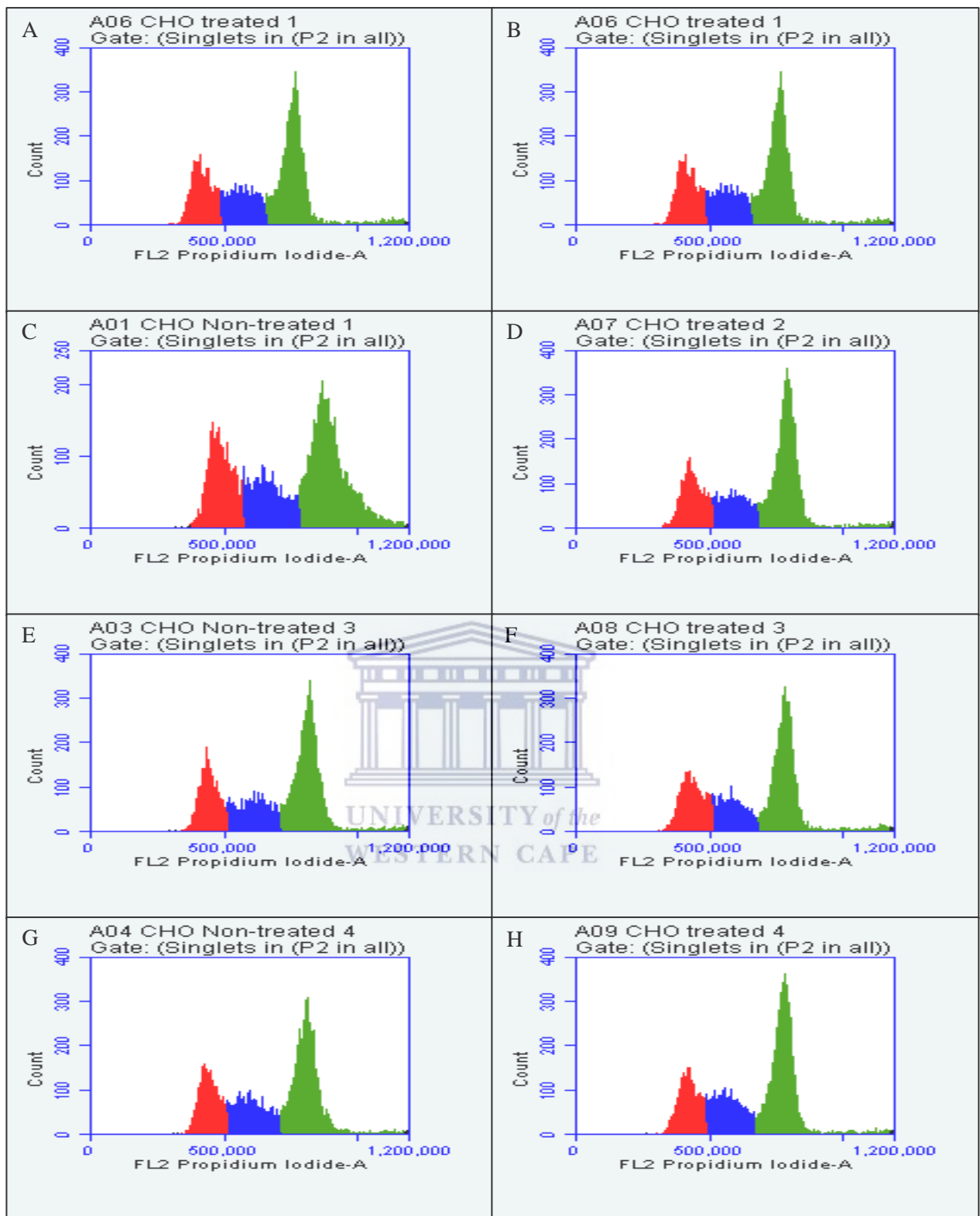


**Figure 5.11:** The effect of 5 nm AuNPs on cell cycle kinetics. Irradiated controls are depicted on the left, whilst irradiated samples containing AuNPs are shown on the right. Samples in row **A)** and **B)** are irradiated in the entrance plateau position, **C)** and **D)** the proximal, **E)** and **F)** the middle **G)** and **H)** the distal positions of the SOBP.

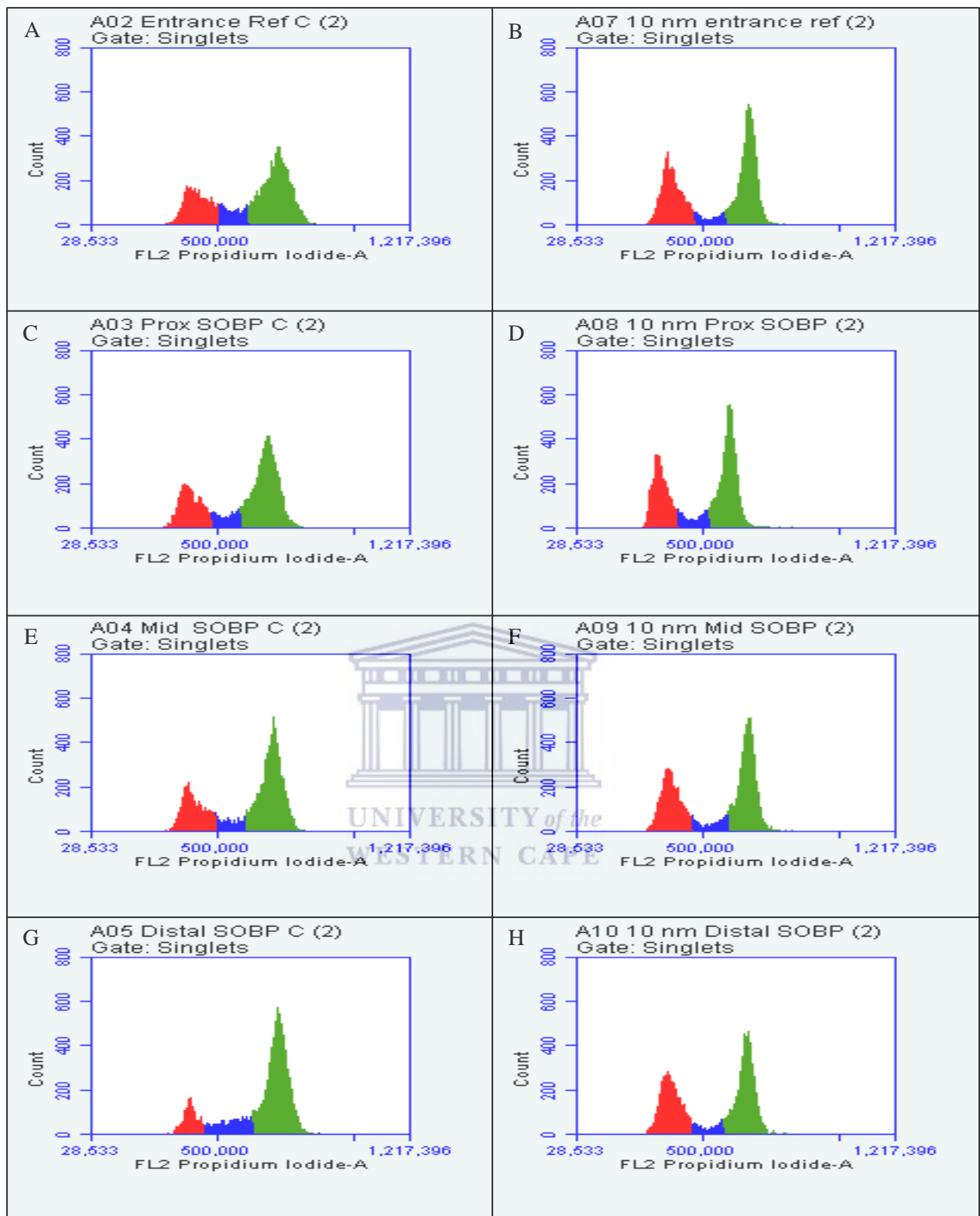


**Figure 5.12:** The effect of 10 nm AuNPs on cell cycle kinetics. Figures on the left, depict irradiated controls without gold, whilst figures on the right depict irradiated samples without gold.

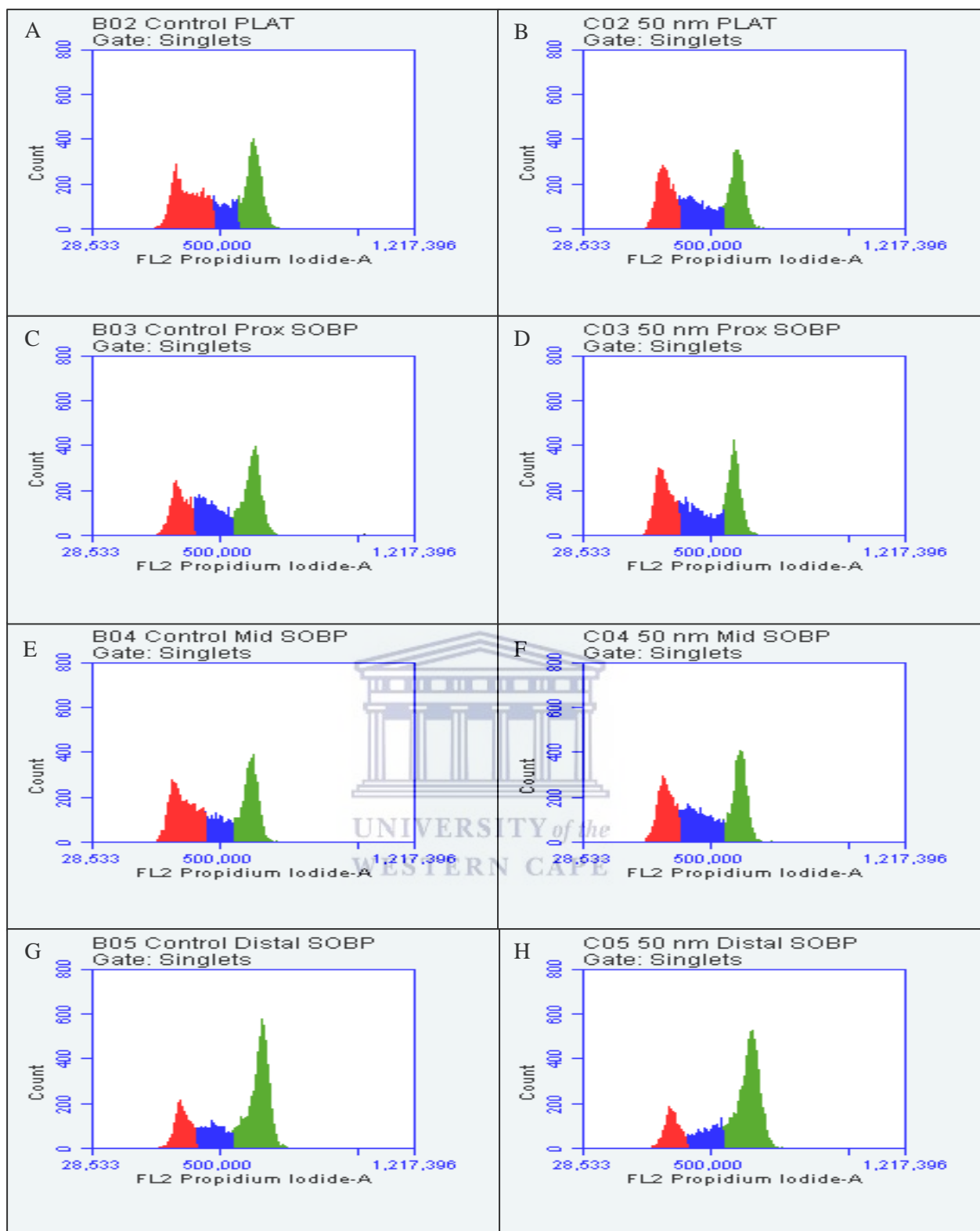


**Figure 5.13:** The effect of 50 nm AuNPs on cell cycle kinetics. Irradiated controls are depicted on the left, whilst irradiated samples containing AuNPs are shown on the right. Samples in **A)** and **B)** are irradiated in the entrance plateau position, **C)** and **D)** the proximal, **E)** and **F)** the middle **G)** and **H)** the distal positions of the SOBPs.